

Radiation Background Studies for Neutrinoless Double Beta Decay in ^{124}Sn

By

Neha Dokania

PHYS01200904009

Bhabha Atomic Research Centre, Mumbai – 400 085

A thesis submitted to the

Board of Studies in Physical Sciences

In partial fulfillment of requirements

For the Degree of

DOCTOR OF PHILOSOPHY

of

HOMI BHABHA NATIONAL INSTITUTE



May, 2015

Homi Bhabha National Institute

Recommendations of the Viva Voce Board

As members of the Viva Voce Board, we certify that we have read the dissertation prepared by Neha Dokania entitled “Radiation background studies for Neutrinoless Double Beta Decay in ^{124}Sn ” and recommend that it may be accepted as fulfilling the dissertation requirement for the Degree of Doctor of philosophy.

Chairman - Prof. B.K. Nayak

Date:

Guide / Convener - Prof. V. Nanal

Date:

Member - Prof. R. Palit

Date:

Member - Prof. S. Saha

Date:

Member - Prof. V. Singh

Date:

Final approval and acceptance of this dissertation is contingent upon the candidate's submission of the final copies of the dissertation to HBNI.

I/We hereby certify that I/we have read this dissertation prepared under my/our direction and recommend that it may be accepted as fulfilling the dissertation requirement.

Date:

Place:

Guide

STATEMENT BY AUTHOR

This dissertation has been submitted in partial fulfillment of requirements for an advanced degree at Homi Bhabha National Institute (HBNI) and is deposited in the Library to be made available to borrowers under rules of the HBNI.

Brief quotations from this dissertation are allowable without special permission, provided that accurate acknowledgement of source is made. Requests for permission for extended quotation from or reproduction of this manuscript in whole or in part may be granted by the Competent Authority of HBNI when in his or her judgement the proposed use of the material is in the interests of scholarship. In all other instances, however, permission must be obtained from the author.

Neha Dokania

DECLARATION

I, hereby declare that the investigation presented in the thesis has been carried out by me. The work is original and has not been submitted earlier as a whole or in part for a degree / diploma at this or any other Institution / University.

Neha Dokania

List of Publications arising from the thesis

Journal

1. “Study of neutron-induced background and its impact on the search of $0\nu\beta\beta$ decay in ^{124}Sn ”, **N. Dokania**, V. Singh, S. Mathimalar, C. Ghosh, V. Nanal, R.G. Pillay, S. Pal, K.G. Bhushan and A. Shrivastava, Journal of Instrumentation **9** (2014) P11002.
2. “Characterization and modeling of a low background HPGe detector”, **N. Dokania**, V. Singh, S. Mathimalar, V. Nanal, S. Pal, R.G. Pillay, Nucl. Inst. Meth. A **745** (2014) 119.

Conferences

1. “Radiation Background studies for $0\nu\beta\beta$ decay in ^{124}Sn ”, **N. Dokania et al.**, arXiv: 1504.05433, To appear in the Proceedings of NuPhys2014: Prospects in Neutrino Physics, 2014.
2. “Simulation studies of Neutron-Induced Background for $0\nu\beta\beta$ decay in ^{124}Sn from underground rock activity at INO”, **N. Dokania et al.**, Proceedings of the DAE Symp. on Nucl. Phys. **59** (2014) 162.
3. “LN₂-free HPGe detector for low background studies”, **N. Dokania et al.**, Proceedings of the DAE Symp. on Nucl. Phys. **59** (2014) 828.

4. “Improvements to background level of the Low Background HPGe setup”, **N. Dokania** *et al.*, Proceedings of the DAE Symp. on Nucl. Phys. **59** (2014) 880.
5. “Study of Neutron-Induced Background in $^{nat,124}\text{Sn}$ and ^{94}Zr for Double Beta Decay”, **N. Dokania** *et al.*, Proceedings of the DAE Symp. on Nucl. Phys. **58** (2013) 118.
6. “Background Radiation Measurements at the INO site”, **N. Dokania** *et al.*, Proceedings of the DAE Symp. on Nucl. Phys. **56** (2011) 1138.
7. “Neutron Transmutation Doping of ^{nat}Ge for thermal sensors”, **N. Dokania** *et al.*, Proceedings of the DAE Symp. on Nucl. Phys. **56** (2011) 1136.

Others

• Journal

1. “Specific Heat of Teflon, Torlon - 4203 and Torlon - 4301 in the range of 30 - 400 mK”, Vivek Singh, Abhijit Garai, S. Mathimalar, **Neha Dokania** *et al.*, Cryogenics **67** (2015) 15.
2. “Characterization of neutron transmutation doped (NTD) Ge for low temperature sensor development”, S. Mathimalar, V. Singh, **N. Dokania** *et al.*, Nucl. Inst. Meth. B **345** (2015) 33.

3. “Study of radioactive impurities in neutron transmutation doped Ge”, S. Mathimalar, **N. Dokania** *et al.*, Nucl. Inst. Meth. A **774** (2015) 68.
4. “Heat capacity setup for superconducting bolometer absorbers below 400 mK”, V. Singh, S. Mathimalar, **N. Dokania** *et al.*, Journal of Low Temperature Physics **175** (2014) 604.
5. “Fusion and quasi-elastic scattering in ${}^6,7\text{Li} + {}^{197}\text{Au}$ systems”, C.S. Palshetkar, Shital Thakur, V. Nanal, A. Shrivastava, **N. Dokania** *et al.*, Phys. Rev. C **89** (2014) 024607 .
6. “Cryogen Free Dilution Refrigerator for Bolometric Search of Neutrinoless Double Beta Decay in ${}^{124}\text{Sn}$ ”, V. Singh, S. Mathimalar, **N. Dokania** *et al.*, Pramana-Journal of Physics **81** (2013) 71.

- **Conferences**

1. “Development of NTD Ge sensors for low temperature thermometry”, S. Mathimalar, V. Singh, **N. Dokania** *et al.*, International Workshop on Low Temperature Electronics 2014, DOI:10.1109/WOLTE.2014.6881014.
2. “Performance of Digitizers with HPGe and Scintillation detectors”, K.V. Anoop, S. Pal, **N. Dokania** *et al.*, Proceedings of the DAE Symp. on Nucl. Phys. **58** (2013) 868.

3. “Defect studies of n-irradiated Ge samples”, S. Mathimalar, V. Singh, **N. Dokania et al.**, Proceedings of the DAE Symp. on Nucl. Phys. **58** (2013) 866.
4. “Testing of the PARIS LaBr₃-NaI Phoswich Detector with High Energy Gamma-rays”, M. Zieblinski, M. Jastrzab, **Neha Dokania et al.**, Acta Phys. Pol. B **44** (2013) 651.
5. “Characterization of a LaBr₃[Ce]-NaI[Tl] Phoswich detector for high energy gamma rays”, **N. Dokania et al.**, Proceedings of the DAE Symp. on Nucl. Phys. **57** (2012) 874.
6. “Study of fusion barrier distribution from quasielastic scattering for ^{6,7}Li + ¹⁹⁷Au systems”, Shital Thakur, **Neha Dokania et al.**, Proceedings of the DAE Symp. on Nucl. Phys. **57** (2012) 406 .
7. “Development of Cryogenic Bolometer for $0\nu\beta\beta$ in ¹²⁴Sn”, V. Singh, G. Yashwant, S. Mathimalar, **Neha Dokania et al.**, AIP Conf. Proc. **1405** (2011) 334.
8. “Half life measurement of ¹⁹⁹Pb in study of reaction in ^{6,7}Li + ¹⁹⁷Au”, Shital Thakur, **Neha Dokania et al.**, Proceedings of the DAE Symp. on Nucl. Phys. **56** (2011) 646 .

9. “Study of direct reactions in ${}^6,7\text{Li} + {}^{197}\text{Au}$ at near barrier energies”, Shital Thakur, **Neha Dokania** *et al.*, Proceedings of the DAE Symp. on Nucl. Phys. **56** (2011) 648.

Neha Dokania

Dedicated to

My Parents

ACKNOWLEDGMENTS

I would like to express my deepest respect to my supervisor, Prof. Vandana Nanal. I convey my regards to her for the continuous support and patience throughout this work as well as for the new dimensions she has brought into my life. Without her inspiring discussions, invaluable guidance and constant encouragement, this accomplishment would never have been fulfilled. She gave me immense freedom to pursue my research work and showed great confidence in me. I am greatly indebted to her assistance and understanding in matters of non-academic concern which helped me to endure some difficult times during my thesis work.

I had the great opportunity to discuss my research work with Prof. R.G. Pillay. His commitment to research, dedication to physics, excellent teaching style, unique personality and even his sense of humour have greatly influenced me.

I consider myself very fortunate to have fruitful interactions with the leading scientists in the field of neutrino physics, Prof. V. Tretyak and Prof. K. Zuber. I strongly feel indebted to Prof. R. Palit, Prof. A. Shrivastava and Prof. V.M. Datar for their useful comments and constructive suggestions throughout my work. I would like to extend my most sincere gratitude to Mr. S.C. Sharma and Dr. K.G. Bhusan for their help with the experiments conducted for this thesis work.

I wish to acknowledge many crucial contributions made by my senior colleagues Dr. Sanjoy Pal, Ms. Shital Thakur, Dr. Vivek Singh and Dr. Y.

Gowda. I would like to sincerely thank my colleagues Mathimalar, Chandan, Sadhana and Abhijit for their fruitful collaborations. I gratefully acknowledge the Pelletron and Linac staff at TIFR for their support during the in-beam experiments. Thanks are due to Kiran Divekar, Mahesh Pose, K.V. Anoop, A. Mahadkar, Deepa mam, Samar, Aman, Prajakta mam, J.N. Karande and Mandar Sawant for their constant help and cooperation.

Many of my friends and INO colleagues selflessly wished for my achievements. I would especially mention Saurabh Sandilya for being the best confidant and accomplice one could ask for. My heartfelt thanks to Ali, Anuradha, Dipankar, Deepak, Jasmine, Kiran, Manisha, Moon Moon, Nitali, Rahul, Subha, Varchaswi and Vinita for making my stay at TIFR an enjoyable one.

Finally and most importantly, I devote my deepest thanks to my parents, Mr. Paban Dokania and Mrs. Renu Dokania, and sister Khusbu for being my pillars of support. This thesis would not have been possible without their encouragement, understanding and boundless love.

TABLE OF CONTENTS

	Page
ACKNOWLEDGMENTS	xi
LIST OF FIGURES	xiv
LIST OF TABLES	xiv
SYNOPSIS	xv
BIBLIOGRAPHY	xxv

Chapters:

1. Introduction	1
1.1 Neutrino Mass Terms	3
1.2 Neutrino Mixing Matrix	5
1.3 NDBD - Experimental Aspects	10
1.4 Sources of Background for $0\nu\beta\beta$ Experiments	18
1.4.1 Techniques of Background Reduction	20
1.5 TIN.TIN Detector	26

2. Characterization of the Low Background HPGe Detector	29
2.1 Introduction	29
2.2 Experimental Details	31
2.3 Monte Carlo Simulations	36
2.3.1 Optimization of Effective Detector Model	38
2.4 Validation of the Effective Detector Model	49
2.5 Summary	55
3. Study of Gamma Background using the TiLES	56
3.1 Introduction	56
3.2 Digital Data Acquisition System	57
3.3 Shielding Arrangement for the HPGe Detector	61
3.3.1 Passive Shield	62
3.3.2 Active Shield	64
3.4 Study of Ambient Background with the TiLES	68
3.5 Radio-purity Measurements	75
3.5.1 Cu Samples	77
3.5.2 Bodi West Hills (BWH) Rock	80
3.5.3 Sn Samples	81
3.5.4 Qualification of TIN.TIN Components	83
3.6 Summary	85
4. Study of Neutron-induced Background and its Effect on $0\nu\beta\beta$	
Decay in ^{124}Sn	87
4.1 Introduction	87

4.2	Experimental Details	89
4.2.1	Estimation of Neutron Flux	94
4.3	Data Analysis and Results	97
4.3.1	Neutron-induced Activity from Torlon and Teflon . . .	100
4.3.2	Neutron-induced Activity from ^{nat} Pb and ^{nat} Cu	105
4.3.3	Neutron-induced Activity in ^{nat} Sn and ¹²⁴ Sn	109
4.3.4	Effect of Neutron-induced Gamma Background for $0\nu\beta\beta$ Decay in ¹²⁴ Sn	111
4.4	Thermal Neutron-induced Background in ^{nat} Sn	113
4.5	Summary	115
5.	Estimation of Neutron Flux at INO Cavern	117
5.1	Introduction	117
5.2	Neutron Production in the INO Cavern	118
5.2.1	Elemental Analysis of BWH Rock	119
5.2.2	Neutron Yield from the BWH Rock	120
5.3	MC Simulation of Neutron Flux at INO Cavern	123
5.4	Neutron Transmission through the BWH Rock	124
5.5	Rock Element Size Optimization	128
5.6	Concept Design for Neutron Shield	134
5.6.1	Laboratory Size Requirements for TIN.TIN	138
5.7	Summary	139
6.	Summary and Future Outlook	141
6.1	Possible Improvements in TiLES	146

6.2 Rare Event Studies with TiLES	146
A. Glossary	152
BIBLIOGRAPHY	155

LIST OF FIGURES

Figure	Page
1.1 A schematic diagram of neutrino masses and mixings of flavour eigenstates.	8
1.2 Value of the effective Majorana mass as a function of the lightest neutrino mass in NH and IH	13
1.3 A schematic of the distribution of the sum of electron energies for $2\nu\beta\beta$ and $0\nu\beta\beta$ modes of the DBD decay.	13
2.1 A picture of the low background HPGe detector	31
2.2 A cross-sectional view of the detector showing different parameters.	32
2.3 Gamma ray spectra showing energy resolution	35
2.4 Effect of collimators on the σ_R	39
2.5 Effect of variation in top Ge dead layer thickness on ϵ^{exp} of $E_\gamma = 59.5$ keV	41

2.6	Effect of variation in side Ge dead layer thickness on ε^{exp} of	
	$E_\gamma = 122.1$ keV	41
2.7	The σ_R for $\varepsilon^{exp}(r = 0)$ data of $E_\gamma = 320.1$ keV	42
2.8	Effect of an inactive Ge dead layer and cylindrical Cu ring at	
	the bottom of the Ge crystal	43
2.9	The ε^{exp} of $E_\gamma = 1115.5$ keV as a function of r (radial scan) . .	44
2.10	The ε^{exp} of $E_\gamma = 1115.5$ keV as a function of z (lateral scan) .	45
2.11	The σ_R for both radial and lateral scans with $E_\gamma = 1115.5$ keV	46
2.12	The σ_R for radial scan data of $E_\gamma = 1115.5$ keV as a function	
	of L for a given R	47
2.13	The radial and lateral scan data of $E_\gamma = 59.5$ keV with opti-	
	mized detector parameters	50
2.14	The radial and lateral scan data of $E_\gamma = 122.1$ keV with opti-	
	mized detector parameters	50
2.15	The top distance and side distance scan data of $E_\gamma = 122.1,$	
	834.8 and 1115.5 keV with optimized detector parameters . .	51
2.16	The radial scans data showing ε^{exp} and ε^{MC} for $E_\gamma = 122.1$ keV	
	and $E_\gamma = 1115.5$ keV with optimized detector parameters at	
	$d = 10.7$ cm	51
2.17	The ε^{exp} as a function of d for volume source geometry ($E_\gamma =$	
	661.7 keV)	52

2.18 The ϵ^{exp} as a function of d for different gamma ray energies	53
2.19 The σ_R for $E_\gamma = 122.1, 279.2, 834.8$ and 1115.5 keV for $d = 5-25$ cm obtained with optimized and nominal detector parameters	53
2.20 The measured energy spectra for ^{54}Mn extended source at $d_s = 25$ cm and ^{137}Cs volume source at $d = 15$ cm together with the simulated spectra	54
3.1 Trapezoidal filter with the relevant parameters	58
3.2 A comparison of ^{152}Eu spectrum with the digitizer and analog electronics	60
3.3 Comparison of the Mn spectra with the digitizer and analog electronics	61
3.4 Decay Schemes of ^{210}Pb , ^{210}Bi and ^{210}Po	62
3.5 A schematic of the TiLES with plastic scintillators	65
3.6 Time profile between HPGe and plastic scintillator signal	66
3.7 Comparison of the observed and the expected random coincidence rate (r) between the pulser and scintillator	67
3.8 A picture of the TiLES with complete shielding arrangement	69
3.9 Gamma ray spectra room background with 10 cm Pb shield	69
3.10 Gamma ray spectra of room background with Cu + Pb shield	71

3.11 Gamma ray spectra of room background in the HPGe detector	
with veto and without veto	72
3.12 The ambient background gamma ray spectra measured in the	
TiLES with full shield	73
3.13 A typical mounting arrangement of a sample in the TiLES for	
counting in a close geometry	76
3.14 A gamma ray spectrum of the ETP Cu sample in the TiLES . .	78
3.15 A gamma ray spectrum of the rock sample from the INO site .	80
3.16 A gamma ray spectrum of the ^{124}Sn sample in the TiLES . . .	82
3.17 A gamma ray spectrum of the $^{\text{nat}}\text{Sn}$ sample in the TiLES . . .	83
3.18 A gamma ray spectrum of the commercial NTD Ge sensor in	
the TiLES	84
4.1 The 6m neutron irradiation set up	91
4.2 A picture of the HPGe detectors D1 and D2	94
4.3 Gamma ray spectra of the neutron irradiated Torlon and Teflon	100
4.4 Decay curves for 511 keV γ -ray in Torlon and Teflon	102
4.5 Gamma ray spectra of the neutron irradiated Teflon	103
4.6 Gamma ray spectra of the neutron irradiated Torlon samples .	104
4.7 Gamma ray spectra of the neutron irradiated $^{\text{nat}}\text{Pb}$ and $^{\text{nat}}\text{Cu}$.	106
4.8 Decay curves for 279 keV and 899 keV γ -ray in $^{\text{nat}}\text{Pb}$	107
4.9 Decay curves for 511 keV γ -ray in $^{\text{nat}}\text{Pb}$ and $^{\text{nat}}\text{Cu}$	108

4.10	Gamma ray spectra of the neutron irradiated ^{124}Sn and $^{\text{nat}}\text{Sn}$.	110
4.11	Gamma ray spectra of the thermal neutron irradiated $^{\text{nat}}\text{Sn}$ sample	114
5.1	Neutron spectra for BWH rock with 60 ppb of ^{238}U and 224 ppb of ^{232}Th	122
5.2	Neutron transmission probability as a function of rock thickness for a mono-energetic point source	125
5.3	Schematic geometry of rock elements RI, RII and RIII considered in the simulations	126
5.4	Neutron spectra after propagation through RI for incident neutron energy $E_n = 10$ MeV	127
5.5	Neutron transmission for three configurations with uniform volume source	128
5.6	Neutron energy spectra for incident neutron energy $E_n = 15$ MeV for the rock element $d = L = 90$ cm	129
5.7	Transmission fraction of neutron for $E_n = 15$ MeV as a function of $d = L = 90$ cm of the rock element for different energy ranges	130
5.8	Neutron spectra of incident neutron energy $E_n = 5, 10, 15$ MeV for rock element $d = L = 140$ cm	131

5.9	A schematic diagram of the underground tunnel assumed as a cylinder	132
5.10	The estimated neutron flux at the center of an underground tunnel at INO site	133
5.11	Neutron shield using (BPE + Pb) between the rock and experimental hall and the corresponding gamma-ray spectra	135
5.12	Transmission probability obtained from the MC and the folding technique through 20 cm BPE for $E_n = 10$ MeV	137
5.13	Neutron spectra at the center of an underground tunnel at INO site after propagation through 20 cm and 40 cm BPE	137
6.1	Decay schemes of ^{94}Zr and ^{96}Zr	147
6.2	Gamma ray spectra of $^{\text{nat}}\text{Zr}$ in the TiLES	150

LIST OF TABLES

Table	Page	
1.1	Experiments contributing to the present determination of the oscillation parameters	9
1.2	Three-flavour oscillation parameters from fit to global data	9

1.3	Ongoing and proposed $0\nu\beta\beta$ experiments	17
1.4	Best reported results for $\beta\beta$ processes	18
1.5	The expected and achieved background levels in the $0\nu\beta\beta$ decay experiments	25
2.1	List of radioactive sources used for measurements	33
2.2	The σ_R for both radial and lateral scans with $E_\gamma = 1115.5$ keV	46
2.3	Optimized parameters of the HPGe detector	48
3.1	Optimum trapezoidal filter settings for two different HPGe detectors	59
3.2	A comparison of energy resolution with analog and DSP . . .	59
3.3	Reduction factor with 10 cm Pb	70
3.4	Reduction factor with 5 cm Cu + 10 cm Pb	71
3.5	Reduction ratio for different energy regions for two configu- rations of plastic scintillators	73
3.6	Background level in TiLES with full shield	74
3.7	Different grades of Cu samples	77
3.8	Observed radio-impurities in different Cu samples	78
3.9	Gamma rays in the ETP Cu sample	79
3.10	Estimated radio-impurity concentrations in the BWH rock sam- ple from the INO site	81
3.11	Gamma rays in the ^{nat}Sn sample	83

4.1	Elemental concentrations of Torlon and Teflon with SIMS . . .	90
4.2	Estimated energy integrated neutron flux	96
4.3	Fast neutron-induced reaction products	98
4.4	Estimation of fast neutron-induced background	112
4.5	Thermal neutron-induced reaction products	114
5.1	Elemental distributions of BWH rock obtained with TOF- SIMS method	119
5.2	The spontaneous fission neutron yield of the U, Th isotopes . .	120
5.3	The Watt spectrum parameters for ^{238}U and ^{232}Th	121
5.4	Details of the alpha yield of the U and Th isotopes	121
5.5	Gamma background produced per incident neutron for differ- ent incident neutron energies	135
6.1	List of potential DBD Isotopes for TiLES	147
6.2	Details of Neutron Irradiation of $^{\text{nat}}\text{Zr}$	148
6.3	Neutron-induced reaction products in $^{\text{nat}}\text{Zr}$	148

SYNOPSIS

Neutrino physics play an important role in the understanding of particle physics beyond the Standard Model, astrophysics and cosmology. The neutrino oscillation experiments have convincingly shown that neutrinos have a finite mass [1]. However, in oscillation experiments only the differences in squares of the neutrino masses (Δm^2) can be measured. Moreover, the oscillation results do not provide information about the properties of neutrinos whether it is a Dirac or a Majorana particle. Double beta decay ($\beta\beta$) is a second-order weak process and is expected to occur in many even-even nuclei where single beta decays are energetically and/or spin forbidden and strongly suppressed. Normal $\beta\beta$ decay is a two-neutrino $\beta\beta$ decay ($2\nu\beta\beta$), which conserves the lepton number and is allowed within the Standard Model and has been experimentally observed in a few isotopes [2, 3]. Neutrinoless $\beta\beta$ decay is an exotic decay, where the two Majorana neutrinos that are virtually produced can annihilate each other leaving only two electrons in the final state. This process violates lepton number conservation and is forbidden in the Standard Model of the electroweak interaction.

The $0\nu\beta\beta$ rate depends on the effective Majorana mass [4] and is given by the following expression:

$$(T_{1/2}^{0\nu})^{-1} = G_{0\nu}(Q_{\beta\beta}, Z) |M_{0\nu}|^2 \langle m_{\beta\beta} \rangle^2 \quad (1)$$

where $G_{0\nu}(Q_{\beta\beta}, Z)$ is the phase-space factor for the emission of the two electrons, $M_{0\nu}$ is the nuclear matrix element and $\langle m_{\beta\beta} \rangle$ is the effective Majorana mass of the electron neutrino. Since the kinetic energy of the two electrons carry the full available decay energy, the experimental signature of $0\nu\beta\beta$ decay is a single peak at the Q value of the decay. Due to the large uncertainty in the model dependent calculation of nuclear matrix element [5, 6], measurements of the $0\nu\beta\beta$ transition rate in different nuclei become extremely important. Several experiments are undergoing and many are planned to search for $0\nu\beta\beta$ decay using different detection techniques [7, 8].

For a rare process such as double beta decay ($T_{1/2} > 10^{20}$ years), the sensitivity of the measurement depends critically on the background level in the region of interest (ROI). The natural radioactivity from the decay chains of U, Th and ^{40}K ($T_{1/2} \sim 10^9 - 10^{10}$ years), setup materials and the detector itself are the source of background. In case of ^{124}Sn , $Q_{\beta\beta} = 2292.64 \pm 0.39$ keV [9] is close to the Compton edge of the 2.614 MeV γ -ray, originating in the decay chain of ^{232}Th . Further, muon-induced interactions in

the materials surrounding the detector give rise to additional background of γ -rays and neutrons. The flux of cosmic ray muons can be significantly reduced in an underground laboratory. Background from internal sources can be minimized by careful selection of radio pure materials [10, 11], while the background from the external sources is reduced by using suitable shielding materials. In recent experiments, ultra low levels of background $\geq 10^{-3}$ cts/(keV kg year) have been achieved [12, 13]. The total background, both from external and internal sources, has to be taken into consideration during the interpretation of results. Generally, a background model employing Monte Carlo (MC) simulations taking into account all the contributions from the actual setup and the environment in the experimental site is used for physics analysis.

A feasibility study to search for $0\nu\beta\beta$ decay in ^{124}Sn using a Sn cryogenic bolometer, The INdia-based TIN detector (TIN.TIN), has been initiated at Tata Institute of Fundamental Research (TIFR) [14]. This thesis work is mainly focused on the characterization of the low background HPGe set up at TIFR for low activity counting and neutron-induced background for the TIN.TIN detector. These aspects are described briefly in the following sections.

Low Background counting setup

In low background gamma spectroscopy, high detection efficiency and complete characterization of the detector for different source geometries are required. A low background counting setup with HPGe detector has been made at TIFR for radiation background studies and qualification of materials. The HPGe detector is a coaxial p-type Ge (ORTEC GEM75-95-LB-C-HJ) with a relative efficiency of $\sim 70\%$. It is constructed with low background materials such as carbon fiber outer body and copper support structures. The detector is cooled by a 60 cm long cold finger attached to a J-shaped cryostat. This assembly allows an all-round shielding of detector capsule with low activity Pb and Cu.

Monte Carlo (MC) techniques are usually adopted to characterize the detector over a wide energy range. It has been reported in the literature [15–17] that simulated efficiencies are generally overestimated (by $\geq 10\%$) as compared to the experimental values. The discrepancy in efficiency is attributed to the inaccuracy of the supplied parameters and/or due to incomplete charge collection [16, 17]. Thus, the parameters of the detector need to be optimized by detailed measurements.

The efficiency measurement in a close geometry with multi gamma line sources is difficult due to the coincident summing effect. Single line gamma sources such as ^{241}Am , ^{57}Co , ^{65}Zn etc., are used to scan the Ge crystal in

directions parallel and perpendicular to its cylindrical axis. Measurements are also done with sources over an energy range of $E_\gamma = 100\text{-}1500$ keV as a function of distance to estimate its active volume. Complete details of the surrounding absorbing materials such as top and side Ge dead layers, Al window, Cu cup support structures, outer carbon fiber body have been included in the MC model. The detector parameters have been optimized corresponding to a minimum relative deviation ($< 5\%$) between the simulated and measured values of absolute photopeak efficiencies of different γ -rays. The optimized detector model works very well for different source geometries and also reproduces the overall experimental spectral shape [18].

The detector is shielded from ambient background γ -rays with a 10 cm thick low activity Pb ($^{210}\text{Pb} < 0.3$ Bq/kg) and low activity 5 cm OFHC Cu shield on all sides. The maximum sample size that can be mounted at $d \sim 1$ cm is $9\text{ cm} \times 9\text{ cm} \times 5\text{ cm}$. The background, at sea level, is dominated by the muon-induced interactions originating in the high Z shield materials. The addition of muon veto system to the setup resulted in a gamma background reduction of $\sim 50\%$ in the region of 0.2-3.0 MeV.

A digital system with a commercial FPGA based 100 MHz digitizer (CAEN-N6724) is used for data acquisition. The setup has been extensively used to test radio-impurities in various samples like the Electrolytic Tough

Pitch (ETP) Copper from the Sn bolometer cryostat, ^{nat}Sn and ^{124}Sn samples of different purity, NTD (Neutron Transmutation Doped) Ge sensors etc. The sensitivity of the setup is ~ 1 mBq/g for ^{232}Th and ~ 2 mBq/g for ^{40}K . Using this setup, radio-impurities in the rock sample from INO site (Bodi West Hills (BWH)) have been estimated. The BWH rock samples was found to have considerable high content of ^{40}K , i.e., 1050(16) mBq/g.

Effect of neutron-induced background in the TIN.TIN detector

Of the different sources of background, namely, α, β, γ and neutrons, background arising from neutrons is most difficult to suppress and hence crucial to understand. In an underground location, neutrons are produced in the spontaneous fission of ^{nat}U (mainly ^{238}U) and Th present in the rocks and surrounding materials. Neutrons are also produced from (α, n) reactions on the light nuclei present in the rocks [19]. Neutrons can lead to gamma background due to radiative neutron capture or through inelastic scattering processes.

Hence, it is crucial to evaluate the neutron-induced gamma background in the region of interest (ROI) for $0\nu\beta\beta$ decay ^{124}Sn . This will also help in the selection/rejection of materials to be used in and around the cryogenic bolometer [20]. As the expected energy resolution of the Sn bolometer is 0.2–0.5% (full width at half maximum) at $Q_{\beta\beta}$, the ROI for background estimation is taken as 2292.6 ± 25 keV (i.e., $Q_{\beta\beta} \pm 5\sigma$). The materials

studied by the neutron activation technique are: ETP ^{nat}Cu used inside the cryostat; Torlon (4203), Torlon (4301) and Teflon – cryogenic materials for detector holders; ^{nat}Pb , ^{nat}Sn and 97.2% enriched ^{124}Sn . The neutron activation was performed using proton beam on Be and Li production targets in the neutron irradiation setup at the Pelletron Linac Facility, Mumbai [21]. Proton beams of energy $E_p = 10, 12$ and 20 MeV on a Be target (5 mm thick) were used to obtain neutrons of a broad energy range with reaction $^9\text{Be}(p, n)^9\text{B}$ ($Q = -1.850$ MeV) [22]. In addition, nearly mono-energetic neutrons were produced using a ^{nat}Li target with the $^7\text{Li}(p, n)^7\text{Be}$ ($Q = -1.644$ MeV) reaction at $E_p = 12$ MeV. The irradiated targets were counted offline for the detection of characteristic γ -rays of reaction products. All the observed gamma rays and the corresponding channels of production were identified.

The Torlon/Teflon samples produced 511 keV γ -ray activity formed via the reaction $^{19}\text{F}(n, 2n)^{18}\text{F}$ at $E_n \geq 11.5$ MeV. Both the Torlon samples showed presence of Al which contribute to high energy gamma background of 2754 keV γ -ray from decay of ^{24}Na . The Torlon 4301 showed Fe which produces short-lived activity ^{56}Mn ($T_{1/2} = 14.997$ h) but the presence of such a magnetic impurity makes it undesirable for use in Sn cryogenic bolometer at low temperatures. The Ti present in Torlon 4203 can produce long-lived impurities like ^{46}Sc ($T_{1/2} = 83.79$ d). Since there is no gamma background

at $E_\gamma > 511$ keV in Teflon, it appears to be a better material for support structures in the Sn cryogenic bolometer. Gamma-rays originating from decay of ^{203}Pb and $^{204\text{m}}\text{Pb}$ and $^{122,124}\text{Sb}$ were seen in the Pb spectrum. Decay of ^{124}Sb produces a γ -ray 2294.02 keV near to the $Q_{\beta\beta}$ of ^{124}Sn but with a small branching fraction (0.032%). The $^{\text{nat}}\text{Cu}$ showed short-lived activities with $T_{1/2}$ ranging from \sim min ($^{62\text{m}}\text{Co}$ and ^{66}Cu) to \sim h (^{64}Cu and ^{65}Ni). Of these, $^{62\text{m}}\text{Co}$ decay produces several high energy γ -rays such as 2882.3 keV. The ^{60}Co ($T_{1/2} = 5.27$ y) was also produced from $^{63}\text{Cu}(n, \alpha)^{60}\text{Co}$ reaction. Hence, it is essential to store Cu in an underground location for extended periods prior to use in the bolometer setup.

Reaction products of other Sn isotopes, namely, ^{112}Sn , ^{115}Sn , ^{116}Sn , ^{117}Sn and ^{122}Sn were found in the Sn samples. Among the various Sn isotopes formed ^{123}Sn has the longest half-life $T_{1/2} = 129.2$ d, while decay of $^{116\text{m}}\text{In}$ produces high energy γ -ray 2112.3 keV. The contribution to the gamma background (a lower limit) within the ROI had been evaluated for an average neutron flux $\sim 10^6$ n cm $^{-2}$ s $^{-1}$ integrated over neutron energy $E_n = \sim 0.1$ to ~ 18 MeV. It is found that $^{\text{nat}}\text{Sn}$ will produce $\sim 5(2)$ times higher gamma background from the 2112.3 keV γ -ray produced in decay of $^{116\text{m}}\text{In}$. Thus, for background reduction enriched Sn is preferable as compared to $^{\text{nat}}\text{Sn}$.

Simulation studies for neutron shield in the INO cavern

The composition of the surrounding rocks namely, the U, Th content and the presence of low Z isotopes determine the level of neutron background in an underground laboratory. A GEANT4-based MC simulations study has been done by incorporating the Bodi West Hills (BWH) rock composition, obtained from Secondary Ion Mass Spectrometry (SIMS). The U and Th content of the rock has been obtained using Inductively Coupled Plasma Mass Spectrometry (ICPMS). The neutron energy spectrum from spontaneous fission of ^{238}U (60 ppb) present in the BWH rock has been generated.

A concept shield design for the neutrons and gammas is suggested as layers of Borated paraffin (BPE) and Pb, of thickness 10 cm and 5 cm respectively. A composite shielding (BPE + Pb + BPE + Pb) is found to be better to reduce the neutron-induced background. The 20 MeV neutron flux in this configuration is attenuated to 0.2%. The overall gamma background, arising from neutron interactions in the paraffin, is 1.5% to that without Pb.

In the first chapter of the thesis, neutrinoless double beta decay is introduced. A brief review of current ($0\nu\beta\beta$) experiments is presented together with the importance and role of background studies for search of $0\nu\beta\beta$ decay. The chapter also presents some of the novel techniques used for background reduction. The second chapter describes the low background

HPGe setup and the Monte Carlo-based optimization of the detector geometry. The third chapter describes the shielding arrangement of the detector. The results of the counting of various materials and their radio-impurity levels are also discussed. Neutron-induced background study of the detector and surrounding materials using activation techniques are described in the fourth chapter. The fifth chapter describes the estimation of the neutron flux in the cavern from the BWH rock activity (spontaneous fission and (α, n) interactions). Summary and conclusions are presented in Chapter 6. Further improvements to the setup and scope of the future work for rare decay studies with the low background setup are also presented.

BIBLIOGRAPHY

- [1] D.P. Roy, *Pramana - Journal of Physics* **54** (2000) 3.
- [2] A.S. Barabash, *Phys. Rev. C* **81** (2010) 035501.
- [3] Ruben Saakyan, *Annu. Rev. Nucl. Part. Sci.* **63** (2013) 503.
- [4] K. Zuber, *Pramana -Journal of Physics* **79** (2012) 781.
- [5] T. Tomoda, *Rep. Prog. Phys.* **54** (1991) 53.
- [6] F. Simkovic, *Physics of Particles and Nuclei Letters* **10** (2013) 623.
- [7] Steven R. Elliott, *Modern Physics Letters A* **27** (2012) 1230009.
- [8] Oliviero Cremonesi and Maura Pavan, *Advances in High Energy Physics* **2014** (2014) 951432.
- [9] D.A. Nesterenko et al., *Phys. Rev. C* **86** (2012) 044313.
- [10] D.S. Leonard et al., *Nucl. Instr. and Meth. A* **591** (2008) 490.
- [11] R. Arnold et al., *Nucl. Instr. and Meth. A* **354** (1995) 338.

- [12] M. Agostini et al., Phys. Rev. Lett. **111** (2013) 122503.
- [13] M. Auger et al., Phys. Rev. Lett. **109** (2012) 032505.
- [14] V. Nanal, International Nuclear Physics Conference – 2013, *EPJ Web of Conferences* **66** (2014) 08005.
- [15] D. Budjas, M. Heisel, W. Maneschg, H. Simgen, Appl. Radiat. and Isot. **67** (2009) 706.
- [16] R.G. Helmer, J.C. Hardy, V.E. Iacob, M. Sanchez-Vega, R.G. Neilson, J. Nelson, Nucl. Instr. and Meth. A **511** (2003) 360.
- [17] F. Hernandez, F.El-Daoushy, Nucl. Instr. and Meth. A **498** (2003) 340.
- [18] N. Dokania et al., Nucl. Inst. Meth. A **745** (2014) 119.
- [19] H. Wulandari, J. Jochum, W. Rau, F. von Feilitzsch, Astroparticle Physics **22** (2004) 313.
- [20] V. Singh, Mathimalar. S, N. Dokania, V. Nanal, R.G. Pillay, S. Ramakrishnan, Pramana - Journal of Physics **81** (2013) 719.
- [21] Sabyasachi Paul et al., Rev. of Sci. Instruments **85** (2014) 063501.
- [22] So Kamada, Toshiro Itoga, Yasuhiro Unno, Wataru Takahashi, Takuji Oishi and Mamoru Baba, Journal of the Korean Physical Society **59** (2011) 1676.

Chapter 1

Introduction

The existence of a neutrino was first proposed by W. Pauli in December 1930, in order to explain the experimentally observed continuous electron spectra in β -decay [1]. For conserving energy, momentum and angular momentum, Pauli postulated that a neutral light particle was emitted in a β -decay together with an electron but was not detected in the experiment and he referred to this particle as “a neutron”. Shortly afterwards in 1932, neutron (with the mass almost equal to the mass of the proton) was discovered by J. Chadwick [2]. Later in 1934, Fermi formulated an effective quantum theory of the β -decay of nuclei based on the Pauli assumptions and named the proposed particle emitted in the β -decay as *neutrino* [3].

In 1935, M. Goepfert-Mayer [4] pointed out the possibility of a double beta decay ($2\nu\beta\beta$) process, i.e. a transformation of a (A, Z) nucleus to a $(A, Z + 2)$ nucleus with the emission of two electrons and two antineutrinos:

$$(A, Z) \rightarrow (A, Z + 2) + 2e^{-} + 2\bar{\nu} \quad (1.1)$$

She also estimated the half-life to be $\sim 10^{17}$ y for such a process. In 1937, Majorana [5] theoretically showed that the conclusions of the theory of β -decay remained unchanged even if only one type of neutrino existed (i.e. $\nu \equiv \bar{\nu}$). In the same year, Racah [6] suggested a possible reaction chain, known as Racah sequence: where initial nucleus (A, Z) emits one beta particle and goes into a virtual intermediate nucleus $(A, Z \pm 1)$ plus a virtual neutrino. The virtual neutrino induces the decay of this intermediate nucleus with emission of the second beta particle and is itself absorbed. In 1939, Furry [7] for the first time considered the $0\nu\beta\beta$ decay following Racah sequence, i.e. the (A, Z) nucleus transforms to the $(A, Z + 2)$ nucleus by emitting only two electrons:

$$(A, Z) \rightarrow (A, Z + 2) + 2e^{-} \quad (1.2)$$

However, he incorrectly estimated the probability of this double beta transition. In 1952, Primakoff [8] calculated the electron-electron angular correlations and electron energy spectra for both $2\nu\beta\beta$ and $0\nu\beta\beta$. This provided a tool for distinguishing between the two processes. The understanding of the β -decay and other weak processes changed drastically after

the discovery of the non-conservation of parity in the weak interaction in 1957-58 [9, 10].

The $2\nu\beta\beta$ decay conserves lepton number (L) while the $0\nu\beta\beta$ decay violates lepton number by two units ($\Delta L = 2$). Both are rare processes and the decay rate of $0\nu\beta\beta$ decay is (at least $\sim 10^6$) smaller than the $2\nu\beta\beta$ decay [11]. The $0\nu\beta\beta$ decay is possible only if neutrinos are Majorana particles with non-zero mass [12]. The observation of neutrino oscillations implies that neutrinos have non-vanishing mass. Presently, $0\nu\beta\beta$, also known as Neutrinoless Double Beta Decay (NDBD), is regarded as a golden probe to study the fundamental character of neutrinos (Dirac or Majorana).

1.1 Neutrino Mass Terms

The two-component massless neutrino theory was proposed by Landau, Lee, Yang and Salam assuming that the neutrino field is $\psi_L(x)$ (or $\psi_R(x)$) [13], in the light of the non-conservation of parity in the weak interaction. Any fermion field can be presented in the form of the sum of left-handed (LH) and right-handed (RH) components:

$$\psi(x) = \psi_L(x) + \psi_R(x) \quad (1.3)$$

where $\psi_{L,R} = [1 \mp \gamma^5]\psi$ are the LH and RH components of the field $\psi(x)$.

A LH component of field must be contracted with the RH component to construct a Lorentz scalar. A mass term is a sum of Lorentz-invariant products of LH and RH components of fields. The scalar term in the Lagrangian obtained in this way is called the Dirac mass term:

$$\mathcal{L}_D(x) = -m_D \overline{\psi(x)} \psi(x) = -m_D (\overline{\psi_R(x)} \psi_L(x) + \overline{\psi_L(x)} \psi_R(x)) \quad (1.4)$$

If the neutrino field is only $\psi_L(x)$ (or $\psi_R(x)$), then the mass term in Eq. 1.4 can not be constructed and hence the Dirac neutrinos have no mass. Alternatively neutrino masses can be obtained by constructing a Lorentz scalar from $\psi(x)$ and its charge conjugate, which is defined as:

$$\psi(x)^c = C \overline{\psi(x)}^T = i\gamma_2 (\psi(x))^* \quad (1.5)$$

where C is the charge conjugation matrix defined by $C = i \gamma_2 \gamma_0$ in the Dirac representation. The chirality of $\psi^c(x)$ is opposite to that of $\psi(x)$. Thus $(\psi_L)^c(x)$ is right handed. Hence, LH and RH Majorana mass terms can be constructed as:

$$\mathcal{L}_M = -\frac{m_L}{2} [\overline{(\psi_L)^c(x)} \psi_L(x) + h.c.] - \frac{m_R}{2} [\overline{(\psi_R)^c(x)} \psi_R(x) + h.c.] \quad (1.6)$$

where h.c. are the hermitian conjugate terms in the Lagrangian. The Majorana mass term can exist in the Lagrangian for only neutral fermions such

as neutrinos but not for particles like electrons or quarks since it violates charge conservation.

1.2 Neutrino Mixing Matrix

The experimental discovery of $\bar{\nu}_e$ was made in 1956 by Reines and Cowan [14] in a nuclear reactor experiment. Later in 1958, Goldhaber et al. measured the helicity of neutrino to be -1 [15]. In 1958, Bruno Pontecorvo suggested the mechanism of neutrino oscillation based on $K^0 \leftrightarrow \bar{K}^0$ effects, a quantum mechanical phenomena depending on the superposition principle [16, 17]. In 1962, $\nu_e \leftrightarrow \nu_\mu$ “virtual transmutations” were mentioned by Maki, Nakagawa and Sakata [18]. This led to the conjecture that the flavour (ν_e, ν_μ, ν_τ) eigenstates and mass eigenstates (ν_1, ν_2, ν_3) of neutrinos are not necessarily identical, a fact well known in the quark sector where both types of states are connected by the CKM matrix [19]. The flavour or weak eigenstates (ν_α ($\alpha = e, \mu, \tau$)) are connected to the mass eigenstates (ν_i ($i = 1, 2, 3$)) via a unitary mixing matrix U (Pontecorvo-Maki-Nakagawa-Sakata matrix):

$$|\nu_\alpha\rangle = \sum_{i=1}^3 U_{\alpha i} |\nu_i\rangle \quad (1.7)$$

In the three neutrino framework, the mixing can be parametrised by three mixing angles ($\theta_{23}, \theta_{13}, \theta_{12}$) and one (three) CP violation phases if neutrinos

are Dirac (Majorana):

$$U = V_{23} W_{13} V_{12} \text{diag}(1, e^{i\alpha_1}, e^{i\alpha_2}) \quad (1.8)$$

where α_1 and α_2 are non-zero if neutrinos are Majorana particles.

$$V_{23} = \begin{pmatrix} 1 & 0 & 0 \\ 0 & c_{23} & s_{23} \\ 0 & -s_{23} & c_{23} \end{pmatrix} W_{13} = \begin{pmatrix} c_{13} & 0 & s_{13}e^{-i\delta} \\ 0 & 1 & 0 \\ -s_{13}e^{i\delta} & 0 & c_{13} \end{pmatrix} V_{12} = \begin{pmatrix} c_{12} & s_{12} & 0 \\ -s_{12} & c_{12} & 0 \\ 0 & 0 & 1 \end{pmatrix} \quad (1.9)$$

where $c_{ij} = \cos(\theta_{ij})$ and $s_{ij} = \sin(\theta_{ij})$, respectively.

The mixing matrix takes the form:

$$U = \begin{pmatrix} c_{12}c_{13} & s_{12}c_{13} & s_{13}e^{-i\delta} \\ -c_{23}s_{12} - s_{23}c_{12}s_{13}e^{i\delta} & c_{23}c_{12} - s_{23}s_{12}s_{13}e^{i\delta} & c_{13}s_{23} \\ s_{23}s_{12} - c_{23}c_{12}s_{13}e^{i\delta} & -s_{23}c_{12} - c_{23}s_{12}s_{13}e^{i\delta} & c_{13}c_{23} \end{pmatrix} \quad (1.10)$$

For CP conservation in the lepton sector, it is necessary to have $U^* = U$. Thus, the phase δ is responsible for effects of the CP violation and δ will be equal to 0 if CP is conserved.

The neutrino oscillation probability, i.e. the transformation probability of a flavour eigenstate neutrino $|\nu_\alpha\rangle$ into $|\nu_\beta\rangle$ is given by:

$$P_{\alpha\beta} = |\langle \nu_\beta | \nu_\alpha(t) \rangle|^2 \quad (1.11)$$

For ultra-relativistic neutrinos with small mass ($p_i \simeq p_j \equiv p \simeq E$):

$$E_i = \sqrt{p_i^2 + m_i^2} \simeq p + \frac{m_i^2}{2E} \quad (1.12)$$

where E_i and m_i are the energy and the mass of the eigenstate ν_i , respectively. Using the orthogonality relation $\langle \nu_j | \nu_i \rangle = \delta_{ij}$ and Eq. 1.12, the transition probability for an initial ν_α of energy E to get converted to a ν_β after traveling a distance $L(=t)$ in vacuum is given by:

$$P_{\alpha\beta} = \delta_{\alpha\beta} - 4 \sum_{i>j} \text{Re} (U_{\alpha i}^* U_{\beta j}^* U_{\beta i} U_{\alpha j}) \sin^2 \left(\frac{(m_i^2 - m_j^2) L}{4E} \right) + 2 \sum_{i>j} \text{Im} (U_{\alpha i}^* U_{\beta j}^* U_{\beta i} U_{\alpha j}) \sin 2 \left(\frac{(m_i^2 - m_j^2) L}{4E} \right) \quad (1.13)$$

It can be seen from Eq. 1.13 that the transition probability has an oscillatory behaviour whose amplitudes are proportional to the elements in the mixing matrix. The neutrino (antineutrino) transition probabilities depend on the mass splitting parameter $\Delta m_{ij}^2 = m_i^2 - m_j^2$ and L/E . There are three possible non-equivalent orderings for the mass eigenvalues, chosen as (Normal Hierarchy, Inverted Hierarchy and Quasi-Degenerate):

$$\text{NO/NH/NS} : \Delta m_{21}^2 \ll +(\Delta m_{32}^2 \simeq \Delta m_{31}^2 > 0)$$

$$\text{IO/IH/IS} : \Delta m_{21}^2 \ll -(\Delta m_{31}^2 \simeq \Delta m_{32}^2 < 0)$$

$$\text{QD} : m_1 \simeq m_2 \simeq m_3 \gg |\Delta m_{ij}^2|^{1/2}$$

The Normal Ordering (NO) / Normal Hierarchy (NH) / Normal Spectrum (NS) and the Inverted Ordering (IO) / Inverted Hierarchy (IH)/ Inverted Spectrum (IS) are pictorially demonstrated in Figure 1.1.

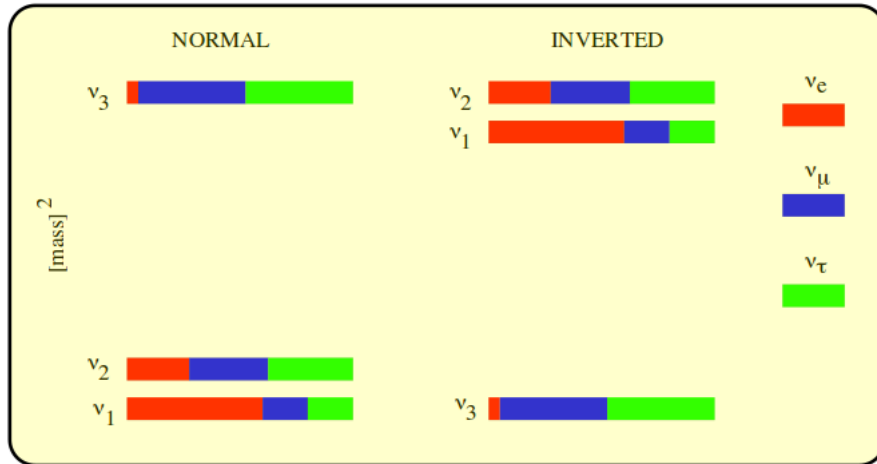


Figure 1.1: A schematic diagram of neutrino masses and mixings of flavour eigenstates in NH and IH. The red, blue and green colours represent ν_e , ν_μ and ν_τ components in the respective mass eigenstates.

The first evidence for neutrino oscillations (solar neutrino anomaly) was found by Davis et al. following the suggestion by Pontecorvo [20]. They detected a smaller rate for solar ν_e as compared to the prediction of Bahcall et al. [21]. The phenomenon of neutrino oscillations (with atmospheric neutrinos) was established in the SuperKamiokande experiment in 1998. Since then neutrino oscillations have been convincingly observed [22] in atmospheric neutrinos [23], solar neutrinos [24], reactor neutrinos [25] and accelerator neutrinos [26, 27] experiments. Table 1.1 shows the ongoing

neutrino experiments together with their sensitivity for different parameters of the PMNS matrix. The latest results on neutrino parameters from the fit to the global experimental data are given in Table 1.2.

Table 1.1: Experiments contributing to the present determination of the oscillation parameters [28]. LBL (MBL) stands for LongBaseLine (MediumBaseLine)

Experiment	Dominant Parameters	Important Parameters
Solar Experiments	θ_{12}	$\Delta m_{21}^2, \theta_{13}$
Reactor LBL (KamLAND)	Δm_{21}^2	θ_{12}, θ_{13}
Reactor MBL (Daya-Bay, Reno, D-Chooz)	θ_{13}	$ \Delta m_{3\ell}^2 $
Atmospheric Experiments	θ_{13}	$ \Delta m_{3\ell}^2 $
Accelerator LBL ν_μ Disapp (Minos, T2K)	$ \Delta m_{3\ell}^2 , \theta_{23}$	
Accelerator LBL ν_e App (Minos, T2K)	δ	$\theta_{13}, \theta_{23}, \text{sign}(\Delta m_{3\ell}^2)$

Table 1.2: Three-flavour oscillation parameters from fit to global data* [29].

	Normal Ordering ($\Delta\chi^2 = 0.97$)		Inverted Ordering (best fit)		Any Ordering 3σ range
	bfp $\pm 1\sigma$	3σ range	bfp $\pm 1\sigma$	3σ range	
$\sin^2 \theta_{12}$	$0.304^{+0.013}_{-0.012}$	$0.270 \rightarrow 0.344$	$0.304^{+0.013}_{-0.012}$	$0.270 \rightarrow 0.344$	$0.270 \rightarrow 0.344$
$\theta_{12}/^\circ$	$33.48^{+0.78}_{-0.75}$	$31.29 \rightarrow 35.91$	$33.48^{+0.78}_{-0.75}$	$31.29 \rightarrow 35.91$	$31.29 \rightarrow 35.91$
$\sin^2 \theta_{23}$	$0.452^{+0.052}_{-0.028}$	$0.382 \rightarrow 0.643$	$0.579^{+0.025}_{-0.037}$	$0.389 \rightarrow 0.644$	$0.385 \rightarrow 0.644$
$\theta_{23}/^\circ$	$42.3^{+3.0}_{-1.6}$	$38.2 \rightarrow 53.3$	$49.5^{+1.5}_{-2.2}$	$38.6 \rightarrow 53.3$	$38.3 \rightarrow 53.3$
$\sin^2 \theta_{13}$	$0.0218^{+0.0010}_{-0.0010}$	$0.0186 \rightarrow 0.0250$	$0.0219^{+0.0011}_{-0.0010}$	$0.0188 \rightarrow 0.0251$	$0.0188 \rightarrow 0.0251$
$\theta_{13}/^\circ$	$8.50^{+0.20}_{-0.21}$	$7.85 \rightarrow 9.10$	$8.51^{+0.20}_{-0.21}$	$7.87 \rightarrow 9.11$	$7.87 \rightarrow 9.11$
$\delta_{\text{CP}}/^\circ$	306^{+39}_{-70}	$0 \rightarrow 360$	254^{+63}_{-62}	$0 \rightarrow 360$	$0 \rightarrow 360$
$\frac{\Delta m_{21}^2}{10^{-5} \text{ eV}^2}$	$7.50^{+0.19}_{-0.17}$	$7.02 \rightarrow 8.09$	$7.50^{+0.19}_{-0.17}$	$7.02 \rightarrow 8.09$	$7.02 \rightarrow 8.09$
$\frac{\Delta m_{3\ell}^2}{10^{-3} \text{ eV}^2}$	$+2.457^{+0.047}_{-0.047}$	$+2.317 \rightarrow +2.607$	$-2.449^{+0.048}_{-0.047}$	$-2.590 \rightarrow -2.307$	$\left[+2.325 \rightarrow +2.599 \right]$ $\left[-2.590 \rightarrow -2.307 \right]$

* Note that $\Delta m_{3\ell}^2 \equiv \Delta m_{31}^2 > 0$ for NO/NS and $\Delta m_{3\ell}^2 \equiv \Delta m_{32}^2 < 0$ for IO/IS.

The questions yet to be answered in neutrino physics are the mass ordering of the neutrinos, absolute mass scale of the neutrinos, CP violation in the leptonic sector and the fundamental nature of neutrinos (Dirac or Majorana). The flavour oscillation experiments are sensitive to the two mass-squared differences (Δm_{ij}^2), three mixing angles ($\theta_{12}, \theta_{23}, \theta_{13}$) and one CP violation phase (δ). The additional Majorana phases do not enter into flavour neutrino and antineutrino transition amplitudes. Further, the study of flavour neutrino oscillations does not reveal the nature of the massive neutrinos. Hence, it is necessary to study processes like NDBD of nuclei.

1.3 NDBD - Experimental Aspects

As mentioned earlier, DBD is a second order weak interaction process, possible in even-even nuclei. The $2\nu\beta\beta$ decay conserves lepton number (L) and is allowed in the Standard Model. It has been experimentally observed in about 12 isotopes [30]. The inverse half-life for $2\nu\beta\beta$ decay is given by:

$$\frac{1}{T_{1/2}^{2\nu}} = G^{2\nu}(Q_{\beta\beta}, Z) |M^{2\nu}|^2 \quad (1.14)$$

where $G^{2\nu}$ is obtained by integration over the phase space of four leptons emitted in the decay and can be calculated exactly, the $Q_{\beta\beta}$ is the Q value of the transition and $M^{2\nu}$ is the Nuclear Transition Matrix Element (NTME)

for this process. For $0\nu\beta\beta$ decay the inverse half-life (or decay rate) is given by:

$$\frac{1}{T_{1/2}^{0\nu}} = G^{0\nu}(Q_{\beta\beta}, Z) |M^{0\nu}|^2 \langle \eta^2 \rangle \quad (1.15)$$

where $G^{0\nu}$ is obtained by integration over the phase space of two leptons emitted in the decay, $\langle \eta^2 \rangle$ is the lepton number violating parameter and $M^{0\nu}$ is the NTME for $0\nu\beta\beta$ decay. There are numerous particles like SUSY, Majoron etc., beyond the standard model and (V+A) interactions, which could mediate the decay [31]. However, the most commonly studied fields mediating the decay are the standard model neutrinos with Majorana masses. In this case, NDBD is sensitive to the effective neutrino mass $\langle m_{ee} \rangle$ and the half-life is given by:

$$\frac{1}{T_{1/2}^{0\nu}} = G^{0\nu}(Q_{\beta\beta}, Z) |M^{0\nu}|^2 \frac{\langle m_{ee} \rangle^2}{m_e^2} \quad (1.16)$$

where m_e is the mass of the electron. To extract the effective neutrino mass $\langle m_{ee} \rangle$, accurate knowledge of $M^{0\nu}$ is essential. Two basic approaches are used to evaluate NTME : the nuclear shell model (NSM) and the quasi-particle random phase approximation (QRPA) [32]. The NTMEs have rather large “theoretical” uncertainties and experiments are required to constrain the different parameters in nuclear models [33]. The $M^{2\nu}$ calculations can be verified with the measured decay rates of $2\nu\beta\beta$ (see Eq.1.14) and these

calculations can be extended to $M^{0\nu}$ calculations for the same isotope. However, it should be mentioned that the intermediate states involved in $2\nu\beta\beta$ and $0\nu\beta\beta$ decays are quite different. Therefore for accurate measurement of effective neutrino mass m_{ee} , it is essential to observe $0\nu\beta\beta$ decay in different nuclei.

The effective neutrino mass m_{ee} in Eq. 1.16 is given by:

$$|m_{ee}| = \left| \sum_i U_{ei}^2 m_i \right| = \left| m_1 c_{12}^2 c_{13}^2 + m_2 s_{12}^2 c_{13}^2 e^{2i\alpha_1} + m_3 s_{13}^2 e^{2i\alpha_2} \right| \quad (1.17)$$

where U_{ei} are elements of PMNS matrix in Eq.1.10 and α_1, α_2 are the Majorana phases.

The $0\nu\beta\beta$ decay can also address the neutrino mass ordering as shown in Figure 1.2. The experimental signature for $0\nu\beta\beta$ decay is a sharp monoenergetic peak at the $Q_{\beta\beta}$ value of the transition as shown schematically in Figure 1.3.

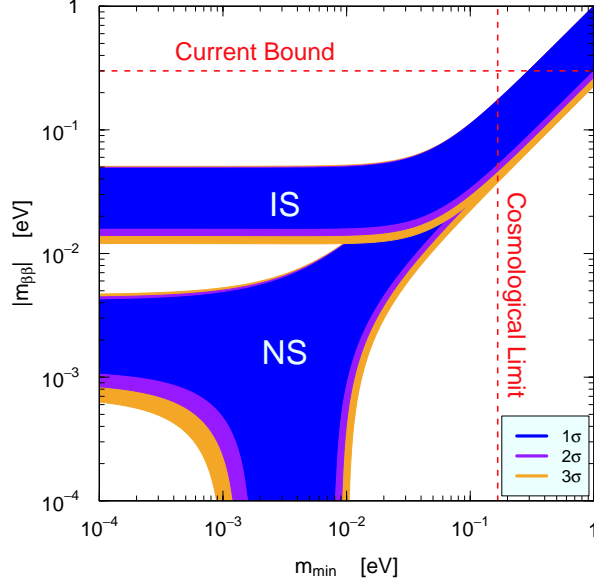


Figure 1.2: Value of the effective Majorana mass as a function of the lightest neutrino mass in the normal (NO/NS, with $m_{min} = m_1$) and inverted (IO/IS, with $m_{min} = m_3$) neutrino mass spectra before and after the Daya Bay measurement of θ_{13} [34].

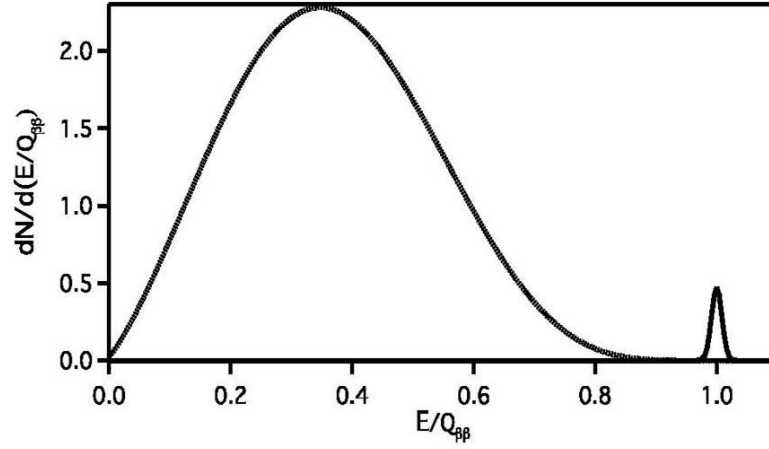


Figure 1.3: A schematic of the distribution of the sum of electron energies for $2\nu\beta\beta$ and $0\nu\beta\beta$ modes of the DBD decay. The figure has been taken from the Ref. [35]. The curves were drawn assuming that the decay rates $\Gamma_{0\nu}$ is 1% of $\Gamma_{2\nu}$ and for a 1σ energy resolution of 2%.

If $0\nu\beta\beta$ decay is positively identified, then the half-life $T_{1/2}^{0\nu}$ can be calculated using the relation given by:

$$T_{1/2}^{0\nu} = \frac{N_A \ln 2 \varepsilon M a t}{W N_{obs}} \quad (1.18)$$

where N_A is Avogadro's number, ε is the detection efficiency, a is the isotopic abundance in the source of the mass M , W is the molar mass of the source, N_{obs} is the number of events attributed to $0\nu\beta\beta$ (above all possible backgrounds) and t is the time of measurement. In the absence of a clear $0\nu\beta\beta$ signal, a lower limit can be placed on the half-life of the process assuming a Gaussian approximation for the background fluctuation:

$$T_{1/2}^{0\nu} > \frac{N_A \ln 2 \varepsilon a}{W k_{CL}} \sqrt{\frac{M t}{N_{bkg} \Delta E}} \quad (1.19)$$

where N_{bkg} is a background index (in $\text{kg}^{-1}\text{keV}^{-1}\text{y}^{-1}$) defined as the number of background events normalized to energy unit, source mass and measurement time, ΔE is the energy window of $0\nu\beta\beta$ decay and k_{CL} is the number of standard deviations corresponding to a given confidence level (e.g. 1.64 σ for 90% CL). Eq. 1.19 highlights key parameters that need to be optimized in a DBD experiment. An ideal experiment should have:

1. Large source size (M), preferably with a high isotopic abundance a .

2. Large Q value of the transition leads to faster decay rate. The $Q_{\beta\beta} > 2.6$ MeV is also desirable as the energy region of interest (ROI) will be above potential backgrounds.
3. A low-background index (N_{bkg}). This is arguably the most important and certainly the most challenging aspect of a $0\nu\beta\beta$ experiment, which limits the sensitivity.
4. High detection efficiency of two electrons.
5. Good energy resolution. This requirement is very critical due to the fact that the continuous spectrum of the electron's energy sum in the $2\nu\beta\beta$ decay is an inherent source of background for the $0\nu\beta\beta$ signal.

The DBD experiments can be broadly subdivided into two main categories:

1. **Active detectors:** The detector material itself is made of DBD isotope. This approach yields a high detection efficiency and compactness. Examples include semiconductor detectors such as High Purity germanium (HPGe), Cadmium Zinc Telluride (CdZnTe), low temperature bolometers (TeO_2), scintillators and liquid noble gas (Xe) detectors. Calorimetric detectors like HPGe detectors and bolometers offer excellent energy resolution. Since these detectors measure only the

energy deposited by the electrons, the background reduction capabilities are relatively poor. However, in some cases like high pressure gaseous time projection chambers (TPCs) filled with xenon and pixellated CdZnTe detectors, electron tracks can be reconstructed with discrimination against α and γ particles.

2. **Passive detectors:** In this case source and detector are separate. The DBD isotope, in form of thin foils or loaded scintillator, is surrounded by detectors to reconstruct the full topology of DBD events. Often these detectors allow electronic discrimination of background and correlation measurements of emitted electrons. The main disadvantages of these detectors are relatively larger sizes, lower detection efficiency and modest energy resolution.

The search for double beta decay started 60 years back with the first reported claim in ^{124}Sn in 1949 [36]. The first geochemical evidence was observed in ^{130}Te in 1950 [37]. The first direct experimental evidence in laboratory came in 1987 when Elliott et al. detected DBD in ^{82}Se [38]. The discovery of neutrino oscillations confirming finite mass of neutrinos has renewed interest in NDBD and many experiments are pursued worldwide. The $0\nu\beta\beta$ decay has not yet been observed and the best current lower limits are $\sim T_{1/2} > 10^{25}$ y. It should be mentioned that the $\beta\beta$ process can also occur in modes like double positron emission ($\beta^+\beta^+$), positron emission and

electron capture (β^+EC) and double electron capture ($ECEC$). These processes are in general strongly disfavoured because of reduced decay energy and available phase space. As a result, $\beta^+\beta^+/ECEC$ modes are experimentally more challenging to detect even though they provide additional experimental signal (β^+ annihilation or X-rays). The list of ongoing and proposed $0\nu\beta\beta$ experiments is shown in Table 1.3 while Table 1.4 lists the best reported results for $\beta\beta$ processes taken from Ref. [39].

Table 1.3: Ongoing and proposed $0\nu\beta\beta$ experiments with detection techniques.

Experiment	Isotope	Technique
CANDLES [40]	^{48}Ca	Solid Scintillator
GERDA [41]	^{76}Ge	Semiconductor
MAJORANA [42]	^{76}Ge	Semiconductor
SuperNEMO [43]	^{82}Se	Tracking + Calorimeter
LUCIFER [44]	^{82}Se	Cryogenic Bolometer + Scintillator
AMoRE [45]	^{100}Mo	Cryogenic Bolometer + Scintillator
MOON [46]	^{100}Mo	Tracking + Scintillator
COBRA [47]	^{116}Cd	Semiconductor
CdWO ₄ [48]	^{116}Cd	Solid Scintillator
CUORE [49]	^{130}Te	Cryogenic Bolometer
EXO-200 [50]	^{136}Xe	Tracking
KamLAND-Zen [51]	^{136}Xe	Liquid Scintillator
SNO+ [52]	^{150}Nd	Liquid Scintillator

Table 1.4: Best reported results for $\beta\beta$ processes taken from Ref. [39]

Isotope	$T_{1/2}^{2\nu}$ (10^{19} y)	$T_{1/2}^{0\nu}$ (10^{24} y)	$ m_{ee} $ (eV)
^{48}Ca	$(4.4^{+0.6}_{-0.5})$	> 0.058	$< 19 - 36$
^{76}Ge	(150 ± 10)	$22.3^{+4.4}_{-3.1}$	$0.32^{+0.03}_{-0.03}$
		> 21	$< 0.17 - 0.29$
^{82}Se	(9.2 ± 0.7)	> 0.36	$< 1.23 - 1.88$
^{96}Zr	(2.3 ± 0.2)	> 0.0092	$< 5.24 - 10.83$
^{100}Mo	(0.71 ± 0.04)	> 1.1	$< 0.71 - 1.05$
^{116}Cd	(2.8 ± 0.2)	> 0.17	$< 1.64 - 2.69$
^{130}Te	(70^{+9}_{-11})	> 2.8	$< 0.45 - 0.70$
^{136}Xe	(217 ± 6)	> 1.6	$< 2.10 - 3.37$
^{150}Nd	(0.82 ± 0.09)	> 0.018	$< 9.01 - 16.07$

1.4 Sources of Background for $0\nu\beta\beta$ Experiments

Given the rarity of $\beta\beta$ processes ($T_{1/2} > 10^{18}$ y) [39, 53, 54], background reduction is very crucial to increase the sensitivity of the measurement of $T_{1/2}$. The background index is of paramount importance in the ROI defined around the $Q_{\beta\beta}$ region depending on the energy resolution of the detector. The potential sources of background are listed below.

1. Natural radioactivity (α, β, γ) which arises from the primordial activities of U, Th and ^{40}K chains with $T_{1/2} \sim 10^9 - 10^{10}$ y. The dominant background comes from the high energy gamma rays from various decay products in the ^{238}U and ^{232}Th natural chains, eg. 2448 keV γ -ray from ^{214}Bi (^{222}Rn progeny) and 2615 keV γ -ray from ^{208}Tl .

2. Primary cosmic rays give rise to spallation neutrons and cosmogenically activated isotopes such as ^{14}C ($T_{1/2} = 5700$ y), ^7Be ($T_{1/2} = 53.24$ d), ^{68}Ge ($T_{1/2} = 271$ d) (seen in GERDA), ^{60}Co ($T_{1/2} = 1925$ d), ^{56}Co ($T_{1/2} = 78$ d) (mostly in cryostat materials like Copper).
3. The low energy background ($< 2\text{MeV}$) arising from Radon which is always present inside tunnels or mines [55]. The ^{222}Rn ($T_{1/2} = 3.8$ d), ^{220}Rn ($T_{1/2} = 55.6$ s) and ^{219}Rn ($T_{1/2} = 3.96$ s) are short-lived gases, produced in the natural radioactive chains of ^{238}U , ^{232}Th and ^{235}U , respectively. Due to the porosity of rock, Radon diffuses out of the exposed rock surface into the atmosphere. For a given type of rock, the Radon background (mostly ^{222}Rn) is proportional to U, Th content of the rock.
4. Neutron background arising from the spontaneous fission (SF) of $^{\text{nat}}\text{U}$ (mainly ^{238}U), Th present in the rocks and the surrounding materials. In addition, alpha particles produced from decay of intermediate nuclei in the natural decay chains can react with light nuclei in the rocks to produce neutrons via (α, n) reactions [56]. Very high energy neutrons ($E_n \sim \text{GeV}$) are produced by muon-induced interactions in the rocks and materials surrounding the detector.

5. Anthropogenic radioisotopes (i.e. artificially produced radioisotopes) like ^{207}Bi with $T_{1/2} = 31.55$ y.
6. The detector and its surrounding materials can be internally contaminated with β -decaying isotopes accompanied by internal conversion (IC), Moller or Compton scattering.
7. Surface contamination of the detectors, especially in bolometers, can be produced due to the degraded α 's coming from U and Th radioactive chains. The contaminated surface can further produce $\beta + \gamma$ events. In fact, above 2.6 MeV the natural β, γ contributions from environmental and material radioactivity tend to vanish and α 's are the only really disturbing background source.

1.4.1 Techniques of Background Reduction

In order to achieve the desired experimental sensitivity, a careful and detailed study of background identification and background rejection is necessary. The latter is of primary importance for background modeling. The standard techniques of background reduction are given below:

- The double beta decay experiments are mostly housed in deep underground site for suppression of cosmic ray muons. Typically at 1 km

underground depth the muon flux is reduced by six orders of magnitude as compared to the sea level.

- The detector system is shielded for the gamma rays using Pb (10-15 cm) and/or Cu (5-10 cm) shields. Usually the graded shielding is employed such that the outermost shield consist of high Z materials. This is further surrounded by the muon and neutron shield. Generally, water tanks/Liq. Ar serve as Cherenkov medium for muon veto and can also act as neutron shield.
- All materials including the shield should be of high radio-purity. The steel cryostat with internal Cu shield used in GERDA is produced from selected low background austenitic steel, ancient Lead ($^{210}\text{Pb} < \text{mBq/kg}$) obtained from a sunk Roman ship is used in CUORE. Similarly, a low contamination Copper cryostat is designed for CUORE.
- The implementation of radon suppression techniques by flushing the system with pure N_2 gas is a mandatory requirement for these experiments. Mitigation of radon-induced background can be obtained by improving the energy resolution of the calorimeter, the accuracy of energy calibration and the ability to identify and subtract ^{214}Bi contributions from the measured spectrum.

- The setup is isolated for extended time (months - y) in an underground laboratory so as to wait for short-lived cosmogenic isotopes to decay. Proper exposure management during production, storage and transport is implemented.

In addition to the above methods, many novel techniques and improved detector technologies over the last decade have lowered the background levels down to $< 10^{-2}$ counts/ (keV kg y) [57–60]. The background rejection capability needs to be optimized with a proper design of the detector. Particle tracking, if possible, is a powerful technique to distinguish a $0\nu\beta\beta$ signal from a background signal. A $0\nu\beta\beta$ event is characterized by a pair of very short tracks (in dense matter) originated at the source position if compared with background events with the same energy (for most of the isotopes $Q_{\beta\beta} \sim 2\text{-}3$ MeV) that are usually characterized by much longer tracks (as in the case of cosmic ray muons) and/or by multi-site energy depositions (e.g. β/γ emissions). It should be noted that active background rejection methods can be counter productive if additional background is introduced (e.g. additional electronic channels for detector segmentation/dual read out vs. single read out of unsegmented detectors).

The background reduction techniques in some of the major NDBD experiments are briefly described in the following.

- **GERDA:** The GERmanium Detector Array uses bare Ge diodes (enriched in ^{76}Ge) in liquid argon supplemented by a water shield. With an exposure of 21.6 kg y, GERDA phase I [61] has strongly disfavoured the previous claim for a $0\nu\beta\beta$ signal in ^{76}Ge [62]. The experiment employs the p-type Broad Energy Germanium detectors (BEGe) produced by Canberra Company (similar in Majorana) [63]. The signal electrode is very small if compared to standard coaxial HPGe detector, this results in a completely different field distribution capable of enhancing the differences between Single Site Events and Multi Site Events pulses [64, 65]. The n-type highly segmented HPGe detectors will be used in Phase II of GERDA to reduce the gamma background component [66].
- **EXO-200 :** Enriched Xenon Observatory-200 is a single liquid Xe detector designed to search for NDBD in ^{136}Xe . With an exposure of 100 kg y, EXO-200 has placed a half-life limit of 1.9×10^{25} y for NDBD in ^{136}Xe [57]. Both the scintillation and ionization signals produced by particle interactions are studied to achieve good energy resolution. EXO-200 aims at the identification (through laser excitation) of the ^{136}Xe $\beta\beta$ decay daughter ($^{136}\text{Ba}^{++}$) as a further and unambiguous signature of a DBD event. The Ba tagging technique has been demonstrated.

- **CUORE** : This is a cryogenic detector to search for $0\nu\beta\beta$ decay in ^{130}Te using TeO_2 crystal bolometers and is in advanced stages of construction after the successful running of its prototype CUORE-0 [58]. Effective techniques for the cleaning of all the surfaces of bolometer crystals have been developed.
- **NEMO3, SuperNEMO** : SuperNEMO aims to extend and improve the successful NEMO3 technology which took data for ~ 9 y and studied DBD in seven different isotopes [60]. The SuperNEMO demonstrator module after 17 kg y of exposure will reach a sensitivity of 6.5×10^{24} y in ^{82}Se [67]. The tracking plus calorimetry technique employed in NEMO3 provides an accurate and efficient identification of background events. A magnetic field is used to improve particle identification capability. SuperNEMO will use planar geometry (instead of cylindrical as in NEMO3) and modular systems.
- **NEXT** : This experiment comprises a Xenon TPC to search for $0\nu\beta\beta$ decay in ^{136}Xe and construction is in progress [68]. It uses Xenon gas where energy and tracking resolutions are better as compared to EXO where liquid Xe is used. In a high pressure Xe chamber the two electrons emitted in a DBD event produce a characteristic track

which is ~ 30 cm long and easily distinguishable from most radioactive induced events.

The expected/achieved background levels in some of the NDBD experiments are given in the Table 1.5. Investigations are underway to make low

Table 1.5: The expected and achieved background levels in the $0\nu\beta\beta$ decay experiments.

Experiment	Achieved N_{bkg} (counts / (keV kg y))	Expected N_{bkg} (counts / (keV kg y))
GERDA [61]	1×10^{-2}	1×10^{-3}
CUORE [58]	1.9×10^{-2}	1×10^{-2}
EXO [57]	1.7×10^{-3}	$\sim 10^{-4}$
NEXT [68]	–	5×10^{-4}
KamLAND-Zen [39]	1.5×10^{-4}	–

temperature calorimeters which can simultaneously detect light and heat, i.e. construction of hybrid scintillating bolometers such as LUCIFER and AMORE [69]. The simultaneous detection of the heat and scintillation components of an event allows to identify and reject α particles with very high efficiency ($\sim 100\%$). It has been shown that α/γ discrimination by pulse shape analysis is also possible in some crystals, both in the heat and light channel [70]. The background modeling using Monte Carlo simulations helps to design experiments - but cannot foresee unexpected backgrounds, e.g. ^{42}Ar in GERDA, alpha surface contamination in CUORE, $^{110\text{m}}\text{Ag}$ in

KamLAND-Zen that can be either Fukushima fallout products or the result of cosmogenic activation of Xe. It should be mentioned that the background reduction techniques are relevant to other rare event studies like dark matter searches.

1.5 TIN.TIN Detector

In India, a feasibility study to search for $0\nu\beta\beta$ decay in ^{124}Sn has been initiated using a Tin cryogenic bolometer [71]. The ^{124}Sn has moderate isotopic abundance $\sim 5.8\%$ and a reasonably high $Q_{\beta\beta}$ value of 2292.64 ± 0.39 keV [72]. Since Tin becomes superconducting at 3.7 K, at temperatures below 1 K its specific heat has only lattice contributions ($\propto T^3$). Thus, it can be made into a bolometric detector at $T < 100$ mK. Very small size (\sim mg) Sn bolometers have been employed for X-ray detection [73]. Cryogenic bolometers have excellent energy resolution (0.2% at $Q_{\beta\beta}$) and therefore are well suited for search of $0\nu\beta\beta$ decay. TIN.TIN detector (The INdia-based TIN detector) is planned to be housed at India based Neutrino Observatory (INO), an upcoming underground facility near Bodi West Hills (BWH) in Madurai [74].

This thesis mainly discusses the background issues pertaining to NDBD search in ^{124}Sn . The $Q_{\beta\beta}(^{124}\text{Sn})$ is close to the Compton edge of 2.614 MeV

γ -ray, originating in the decay chain of ^{232}Th . The TiLES (Tifr Low Background Experimental Setup) with a special low background HPGe detector has been set up at sea level at TIFR for radiation background studies. This low background HPGe detector is completely characterized with Monte Carlo studies using GEANT4 simulations. The detector model has been optimized for measurements over a wide energy range and for different source geometries with GEMS (Germanium Efficiency based on Monte carlo Simulations). The TiLES consists of a 5 cm low activity Cu shield surrounded by a 10 cm low activity Pb shield and active veto system. The TiLES has been used for the screening and qualifications of the materials to be used in and around the bolometer.

As mentioned earlier, there are different sources of radiation background (α, β, γ , neutrons) for a NDBD experiment. Of the different sources of background, neutron is the most crucial to understand, can travel large distances and difficult to suppress. Neutron-induced background in the ROI near $Q_{\beta\beta}(^{124}\text{Sn})$ arising from the fast and thermal neutrons has been studied using neutron activation techniques in the detector and surrounding materials of TIN.TIN detector. The neutron flux from natural radioactivity of the cavern rock at the underground site has been estimated and concept shield design for the neutron-induced background is proposed. Based on

these considerations, requirements for the cavern to house TIN.TIN detector are presented. These aspects of radiation background studies for NDBD in ^{124}Sn are described in the following chapters.

Chapter 2

Characterization of the Low Background HPGe Detector

2.1 Introduction

For screening of materials to be used in the prototype bolometer R&D as well as for understanding the background pertaining to NDBD search in ^{124}Sn , the low background γ -ray spectrometry technique with HPGe detector is used. The low background γ -ray spectrometry is a very powerful method with sensitivity down to several tenths of a $\mu\text{Bq/kg}$ and enables simultaneous identification of multiple γ -emitters present in a sample. To assess the level of radio purity in the materials, samples are often counted in a close geometry to obtain high counting efficiency. For accurate determination of radio impurities, precise knowledge of detection efficiency over a wide energy range is necessary. The efficiency measurement in a close

geometry is complicated using standard multi-gamma sources due to coincidence summing effects. Hence, measurements are restricted to available mono-energetic sources in a limited energy range. Consequently, MC simulation technique is adopted to obtain efficiency of the detector over a wide energy range for different source-detector configurations. It has been observed in the literature [75–82] that the efficiency computed from the MC simulations using the detector geometry supplied by the manufacturer is overestimated (by $\geq 10\%$) as compared to the experimental values. The discrepancy in efficiency is attributed to the inaccuracy of the supplied parameters, like detector size and the dead layer. It should be mentioned that this effect is more pronounced for large size detectors [79, 80], which may be due to incomplete charge collection.

This chapter describes the optimization of the HPGe detector parameters to generate an effective detector model using MC simulations. Monoenergetic sources are used to scan the Ge crystal in directions parallel and perpendicular to its cylindrical axis. Measurements are also done with sources over an energy range of $E_\gamma = 100\text{-}1500$ keV as a function of distance to estimate its active volume. The effective detector model is validated with gamma energies 500-1500 keV using point and volume sources.

2.2 Experimental Details

The HPGe detector is a coaxial p-type Ge (ORTEC GEM75-95-LB-C-HJ), specially designed for low background measurements with a relative efficiency of $\sim 70\%$. It has a low background carbon fiber outer body and copper support structures with a 60 cm long cold finger attached to a J-shaped cryostat (see Figure 2.1).



Figure 2.1: The low background HPGe detector (ORTEC GEM75-95-LB-C-HJ).

Figure 2.2 shows the cross-sectional view of the detector indicating different parameters. The detector bias used is +4 kV, as recommended by the manufacturer. The nominal size of the Ge crystal given by the manufacturer is 78.3 mm diameter and 63 mm length with a 0.7 mm dead layer on the cylindrical side. In addition to electrical contacts, the detector is surrounded

by aluminized mylar and thin copper on sides as well as on bottom for thermal shielding. Generally, the physical dimensions of the detector can be determined by radiography [75, 83] but the active volume of the detector may differ depending on the electric field configuration inside the crystal [80].

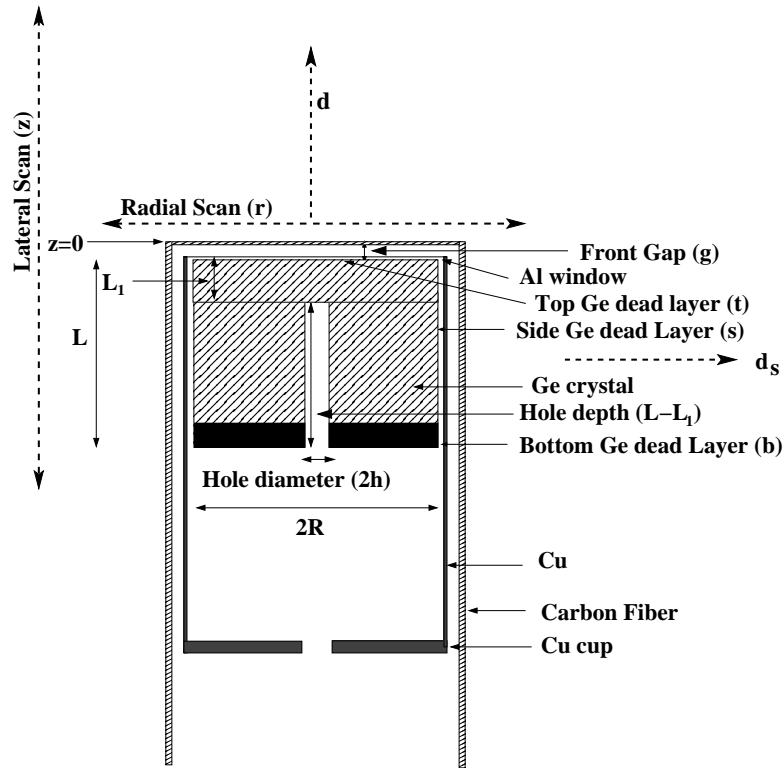


Figure 2.2: A cross-sectional view of the detector showing different parameters. Scan directions for lateral (z), radial (r), top (d) and side (d_s) are also indicated. The center of the detector corresponds to $r = 0$ and the top edge of the detector, i.e. carbon fiber housing, corresponds to $z = 0$.

Precise measurements of photopeak efficiencies using radioactive sources give better estimates on the actual active volume and the surrounding materials of the detector. In the present case, radiography of the setup was not possible and hence mono-energetic sources covering an energy range of 59.5–1115.5 keV were used to scan the crystal. Table 2.1 gives the details of various sources and source geometries used in the present work together with respective gamma ray energies.

Table 2.1: List of radioactive sources used for measurements.

Isotopes	Energy (keV)	Geometry
^{241}Am	59.5	point
^{57}Co	122.1	extended
^{203}Hg	279.2	extended
^{51}Cr	320.1	extended
^{137}Cs	661.7	volume
^{54}Mn	834.8	extended
^{65}Zn	1115.5	extended
^{152}Eu	121.8, 778.9, 1408	point
^{60}Co	1173.2, 1332.5	point

Measured absolute strengths of sources are in the range of $\sim 1\text{-}90$ kBq with $\sim 0.8\text{-}1.5\%$ uncertainty¹. The extended geometry source has a 6 mm active diameter and is mounted on a 25 mm diameter plastic disc with a 1 mm thick plastic front cover. In case of ^{137}Cs volume source, the liquid

¹The strengths of the sources were measured using another calibrated HPGe detector.

was sealed inside a perspex cylindrical vial of radius 3 mm and height 5 mm. The distribution of ^{137}Cs volume source was assumed to be homogeneous in the perspex vial. Measurements for optimizing detector geometry can be broadly classified into three categories (see Figure 2.2), namely, radial scan, lateral scan and distance scan for volume effect. Radial and lateral scans are carried out with ^{241}Am , ^{57}Co and ^{65}Zn sources. The low energy gamma rays are sensitive to the dead layers and high energy gamma rays probe the detector size. Radial scan was done by moving the source parallel to the top detector face (r) at a distance of 5 mm in 3 mm steps and covered a range of ± 6 cm w.r.t. the center of the detector. For the lateral scan the source was moved parallel to its cylindrical axis (z) at a distance of 8 mm from the side face of the detector in 3 mm steps and covered a range of ± 8 cm w.r.t. the top face of the detector. The distance scan (d) was done in steps of 5 cm over a distance of 0–25 cm from the top face as well as from the cylindrical side of the detector to study the volume effect for $E_\gamma = 834.8$ and 1115.5 keV. Typical uncertainty in positioning of the source, both in horizontal and vertical direction, was less than 1 mm. Detector signal was given to a 13-bit analog-to-digital converter through a spectroscopic amplifier (shaping time : 10 μs). Data was recorded with a CAMAC-based acquisition system, LAMPS [84]. Dead time correction was done using a standard 10 Hz pulser. Figure 2.3 shows gamma-ray energy

spectra with ^{57}Co and ^{65}Zn . Typical measured energy resolution (FWHM) obtained was 0.75(2) keV at 122.1 keV and 1.84(2) keV at 1115.5 keV, respectively. Photopeak efficiency (ϵ^{exp}) was extracted using LAMPS soft-

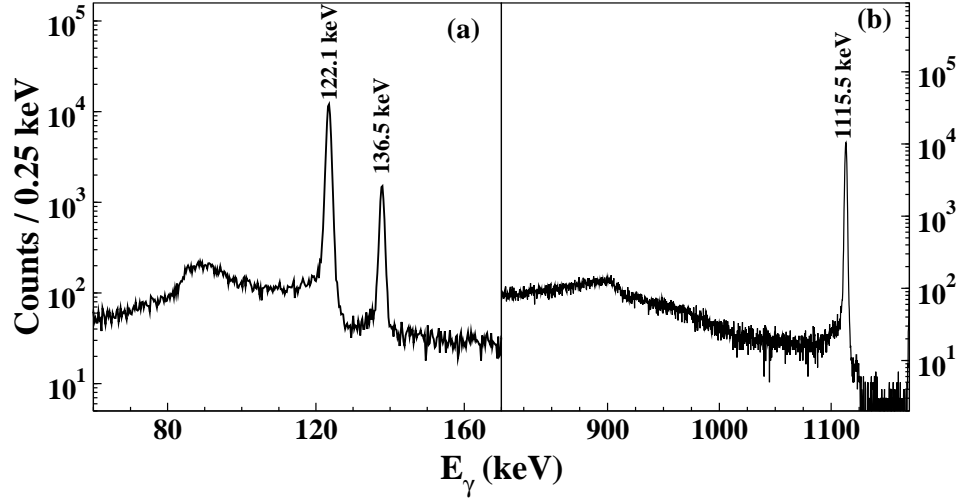


Figure 2.3: Gamma ray spectra obtained with (a) ^{57}Co at $d = 10$ cm, and (b) ^{65}Zn source at $d = 1$ cm.

ware by fitting the observed photopeak to a Gaussian function with either a linear or a quadratic background. In some cases, the observed peak had a slight low energy tail, which could be incorporated in the fitting software. However, the contribution from tail region was found to be negligible. In the present case, given relatively low source strengths no pile up effects have been observed in the spectra. Errors were computed including statistical errors and least-squares fitting errors in extracting the peak areas. Typical errors obtained in ϵ^{exp} were : in radial/lateral scans $\sim 3.7\%$ for $E_\gamma = 59.5$ keV,

0.2% for $E_\gamma = 122.1$ keV and 1.8% for $E_\gamma = 1115.5$ keV. It should be mentioned that differences in statistical errors are mainly due to the difference in strengths of various sources and energy dependent variation in detection efficiency. Similarly, for both the top and side distance scan errors in ϵ^{exp} were $\sim 2\%$ and $\sim 5\%$, respectively.

To verify the effective detector model, additional radial scans with ^{57}Co and ^{65}Zn sources at $d = 10.7$ cm were carried out and distance scan ($\sim 1\text{--}30$ cm) was done with various sources covering an energy range of 122.1–1408 keV. In this case, multi-gamma sources such as ^{152}Eu and ^{60}Co were used at a distance $d > 10$ cm to ensure that the coincidence summing is negligible. Measurements were also done with the volume source ($E_\gamma = 661.7$ keV).

2.3 Monte Carlo Simulations

In the present work, GEANT4 (version 4.9.5.p01) [85] is used to simulate the HPGe detector response. The coaxial geometry of Ge crystal with a central hole is realized in the simulations by placing a circular disk of radius R and thickness L_1 on a hollow cylinder of length $L - L_1$, as shown in Figure 2.2. The inner radius of the hollow cylinder is taken to be that of the hole (h) and the outer radius is R . The curvature of the edges of the cylinder/disk is neglected. Complete details of the surrounding absorbing materials such

as top and side Ge dead layers, Al window, Cu cup support structures, outer carbon fiber body have been included in the Monte Carlo model. Source geometry is also taken into account in the MC simulations. It should be mentioned that the MC code is verified with other HPGe detector geometries [76, 81]. A photon of given energy is generated in the MC simulations. Simulations have been carried out for a set of detector parameters over a range of r and z in 6 mm steps corresponding to the measurements. Event by event data obtained from MC is binned in 0.25 keV bin size and absolute photopeak efficiency (ϵ^{MC}) is determined using the ROOT analysis framework [86]. In some cases where the source co-ordinates in the experiment (r_i, z_i) were different from those in the simulation (diff. ~ 1 mm), the ϵ^{MC} corresponding to r_i, z_i was obtained by interpolation. Statistical uncertainties are kept below 2%. For modeling the detector geometry, only absolute photopeak efficiencies of different γ -rays are taken into consideration. The best fit values of detector parameters are obtained by two methods. In the first method, χ^2 is determined for a data set like radial/lateral/distance scan (n points) corresponding to each source [87] using Eq. 2.1,

$$\chi^2 = \frac{1}{n-1} \sum_{i=1}^n \frac{(\epsilon_E^{\text{exp}}[r_i] - \epsilon_E^{\text{MC}}[r_i])^2}{\epsilon_E^{\text{MC}}[r_i]} \quad (2.1)$$

where, $\varepsilon_E^{exp}(r_i)$ represents the measured absolute photopeak efficiency at r_i for a γ -ray of energy E_γ and $\varepsilon_E^{MC}(r_i)$ is the corresponding simulated efficiency. In the second method, following the procedure as in [78, 79] to give similar weightage to ε_E for different energies, the total relative deviation between measured and simulated efficiencies is calculated as defined in Eq. 2.2,

$$\sigma_R = \frac{1}{n_2} \sum_{j=1}^{n_2} \left\{ \frac{1}{n_1} \sum_{i=1}^{n_1} \frac{|\varepsilon_{E_j}^{exp}[r_i] - \varepsilon_{E_j}^{MC}[r_i]|}{\varepsilon_{E_j}^{MC}[r_i]} \right\} \quad (2.2)$$

where n_1 is number of points in each data set and n_2 is number of data sets corresponding to different energies or scans.

2.3.1 Optimization of Effective Detector Model

It is observed from the simulation data that the measured value of 66% relative efficiency corresponds to an active volume of $\sim 230 \text{ cm}^3$, which is significantly smaller ($\sim 20\%$) than the number quoted by the manufacturer (292 cm^3). Further, a comparison of ε_E^{MC} using default detector parameters with ε_E^{exp} for $E_\gamma = 122.1$ to 1115.5 keV and $d = 5$ to 25 cm , resulted in a large relative deviation, $\sigma_R \sim 29.2(3)\%$. The response of the central core region of the detector was probed by measurements with two collimators made from a 5 cm thick lead block with a 13 mm (35 mm) diameter conical (cylindrical) hole at the center. In both cases, a better agreement has been observed between the simulations and the measured values for the restricted

central volume of the detector. Figure 2.4 shows that the σ_R obtained is less than 10% when measurements done with a collimator and without varying any parameters in MC simulations.

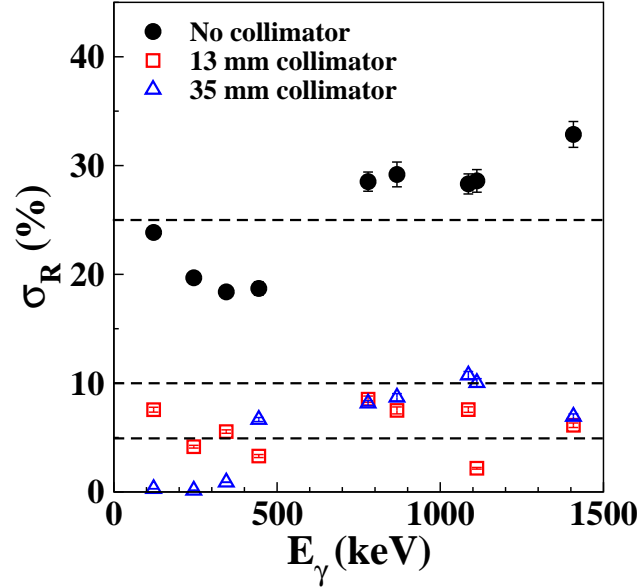


Figure 2.4: The σ_R as a function of gamma ray energies at $d = 25$ cm, distance from the top face of the detector using the 13 mm Pb collimator (unfilled square) and 35 mm Pb collimator (unfilled triangle). The σ_R with the nominal parameters have also been shown for comparison. Errors are within the point size.

It is therefore necessary to optimize the size of the detector to reproduce the experimental data. For generating the detector model, the crystal parameters varied are (see Figure 2.2) : top Ge dead layer (t), side Ge dead layer (s), front gap (g) i.e., the distance between the top carbon fiber and the Al window, crystal radius (R), crystal length (L_1 and L) and hole radius (h). External detector parameters like thicknesses of carbon fiber housing,

Al window and Cu cup are taken as given by the manufacturer. Initial crystal parameters, namely, radius ($R_i = 37.5$ mm), length ($L_i = 55$ mm), hole radius ($h_i = 6.5$ mm) and front gap ($g_i = 5$ mm) were obtained by the best fit to the scan data of $E_\gamma = 1115.5$ keV at close distance ($d \sim 1$ cm), where measurements are not strongly affected by the dead layers and surrounding materials. For the front gap estimation, the fit has been restricted to the central region i.e. $r = \pm 3$ cm, to minimize the effect of radial extension of crystal.

The Ge dead layer on the crystal attenuates the gamma rays and is best estimated with low energy gamma rays. It reduces the active volume of the detector [88] and may also increase with time depending on years of operation [89]. As mentioned earlier, no top dead layer (t) has been specified by the manufacturer while the side dead layer (s) is quoted as 0.7 mm. The uniform dead layer is employed in the simulations and values of t and s are varied in the range of 0–1.2 mm and 0.7–1.5 mm, respectively. The σ_R is calculated for the central region of radial (lateral) scan, namely, $r = \pm 3$ cm ($z = \pm 2.5$ cm), with 59.5 keV and 122.1 keV γ -ray sources mounted close to the face of the detector ($d \sim 1$ cm). Figure 2.5 and Figure 2.6 show the variation of MC parameters of t, s together with the fit to the combined σ_R of 59.5 keV and 122.1 keV γ -ray energies, respectively. The best fit values of t and s extracted corresponding to a minimum σ_R are $t_{opt} = 1.04 \pm 0.02$ mm

and $s_{opt} = 1.27 \pm 0.02$ mm. It should be mentioned that a 2% variation in dead layer thickness results in $\sim 2\%$ change in the photopeak efficiency for $E_\gamma = 59.5$ keV.

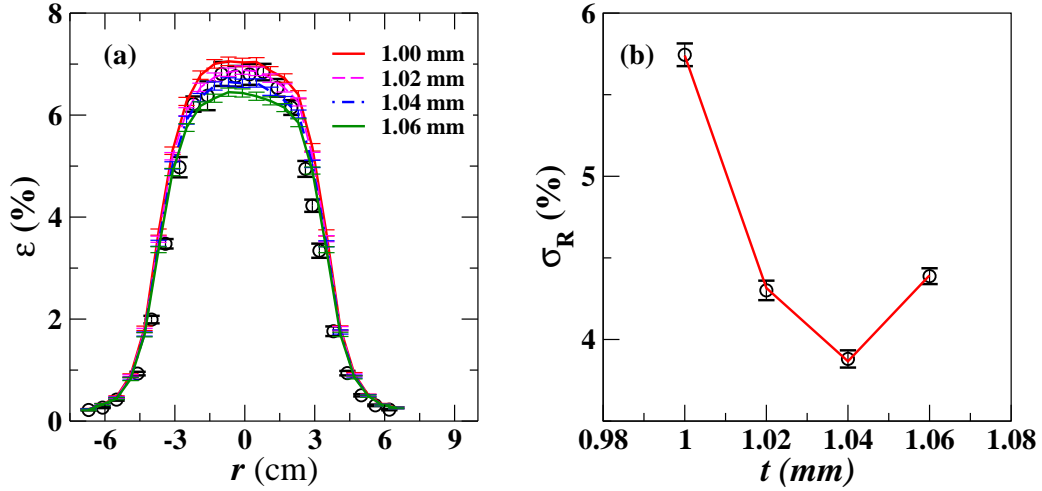


Figure 2.5: (a) The radial scan data of $E_\gamma = 59.5$ keV with different values of parameters. Symbols represent the ε^{exp} and the line corresponds to ε^{MC} , (b) The total σ_R (59.5 keV + 122.1 keV) for radial scan. Symbols represent the experimental data and the line corresponds to the parabolic fit.

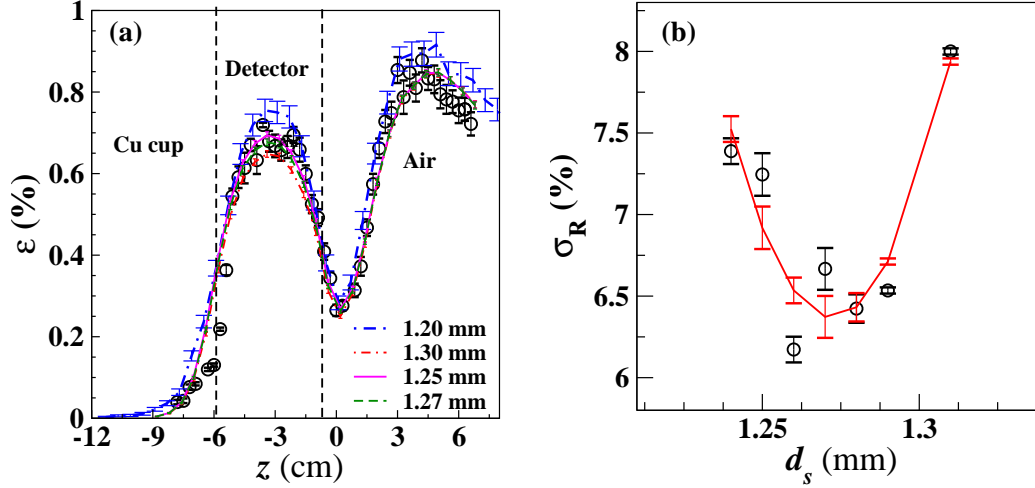


Figure 2.6: Same as Figure 2.5 for lateral scan. The z range occupied by the crystal is marked in the figure.

The germanium disc thickness L_1 was obtained by fitting the $\varepsilon^{exp}(r=0)$ data of $E_\gamma = 320.1$ keV close to the detector top face. Since for this energy half-value layer for germanium is ~ 5 mm, the ε^{MC} is expected to have better sensitivity for L_1 and has a very little dependence on dead layers. The L_1 was varied from 7.5 mm to 12.3 mm in steps of 0.2 mm and minimum σ_R was found at $L_{1-opt} = 9.7 \pm 0.5$ mm. Figure 2.7 shows the fit (for $L_1 = 8.3 - 11.5$ mm) together with the σ_R as a function of L_1 .

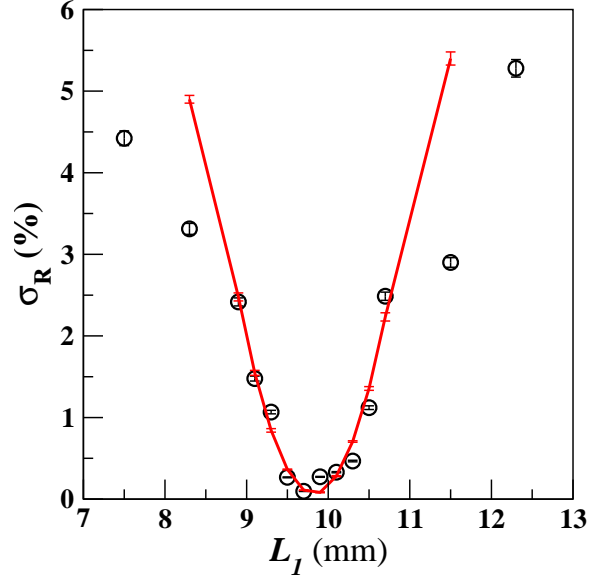


Figure 2.7: The σ_R for $\varepsilon^{exp}(r=0)$ data of $E_\gamma = 320.1$ keV. Symbols represent the experimental data and the line corresponds to the parabolic fit.

Considering the physical length specified by the manufacturer (L_m), an inactive Ge dead layer of thickness $b=L_m - L$ surrounded by a 3.5 ± 0.5 mm thick cylindrical Cu ring at the bottom of the crystal is included in the model. This resulted in a better reproduction of the overall shape of the measured lateral scan for low energy gamma-rays (see Figure 2.8).

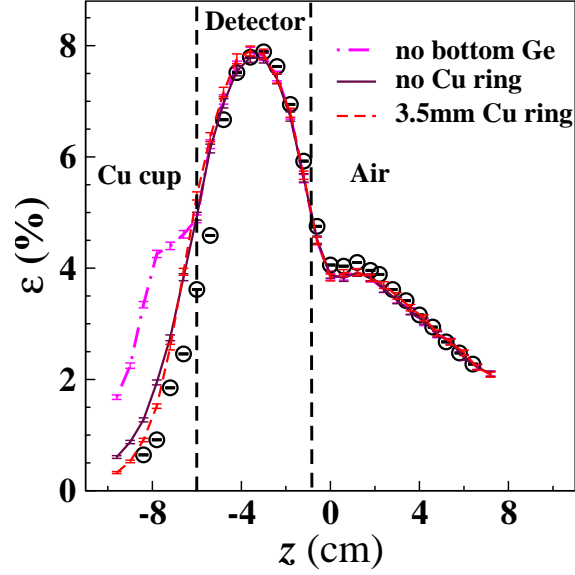


Figure 2.8: The lateral scan of $E_\gamma = 122.1$ keV at $d_s = 1.5$ mm showing the effect of an inactive Ge dead layer of thickness b and cylindrical Cu ring at the bottom of the crystal. Symbols represent the ε^{exp} and the line corresponds to ε^{MC} . The z range occupied by the crystal is marked by the dotted lines in the figure.

For extracting R_{opt} and L_{opt} , simulations have been carried out by varying R and L in fine steps of 0.25 mm and 1 mm, respectively. Figures 2.9 and 2.10 show ε^{exp} together with ε^{MC} for the radial and lateral scan of $E_\gamma = 1115.5$ keV, respectively. It is evident that R and L are not independent of each other. Therefore, the best fit values of R and L are obtained by a simultaneous fit to the radial and the lateral scan data for $E_\gamma = 1115.5$ keV. Table 2.2 lists the σ_R for $R = 37.25\text{--}38.0$ mm and $L = 52\text{--}56$ mm for $E_\gamma = 1115.5$ keV.

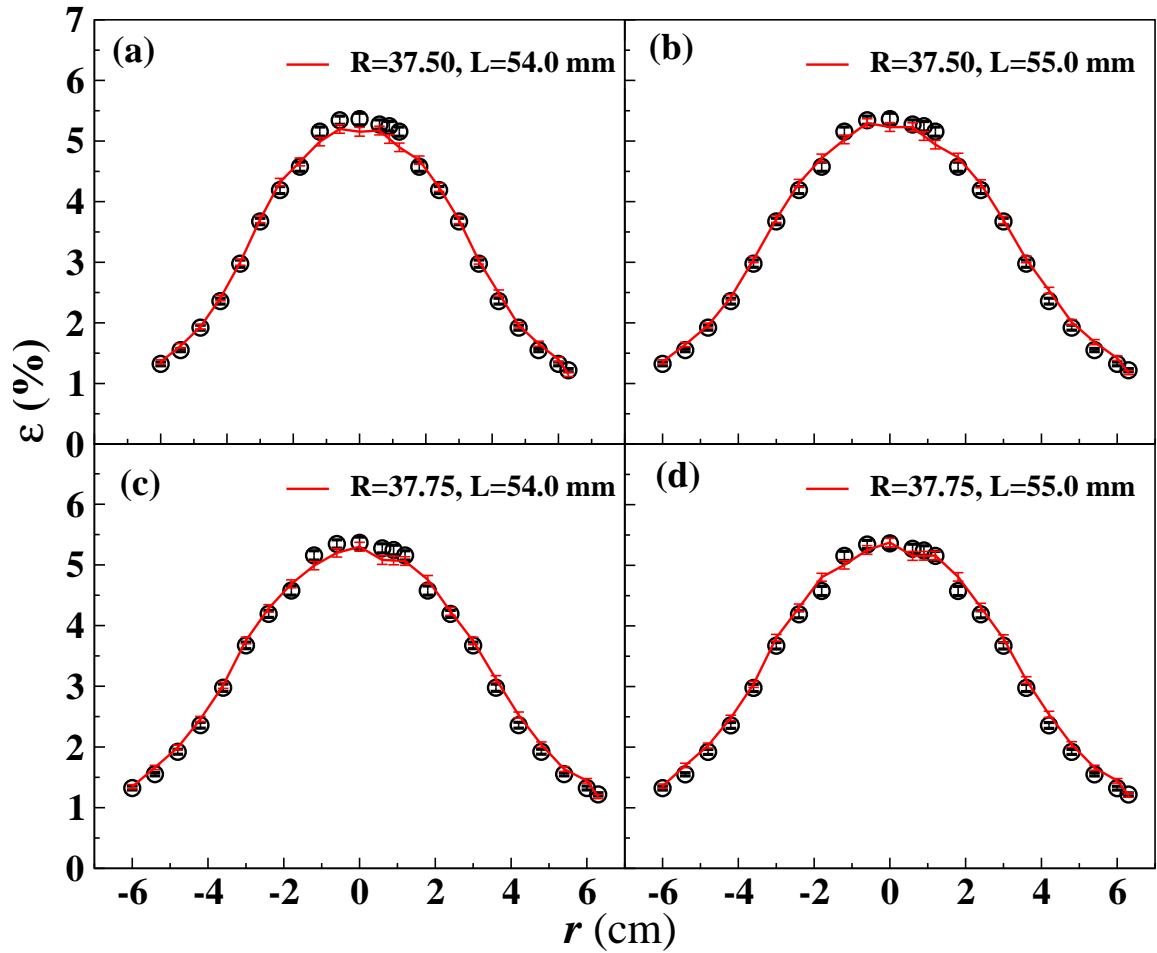


Figure 2.9: The absolute photopeak efficiency ε^{exp} (unfilled circles) of $E_\gamma = 1115.5$ keV as a function of r (radial scan). The simulated values ε^{MC} (lines) for different combinations of radii (R) and lengths (L) are shown in panels (a) to (d).

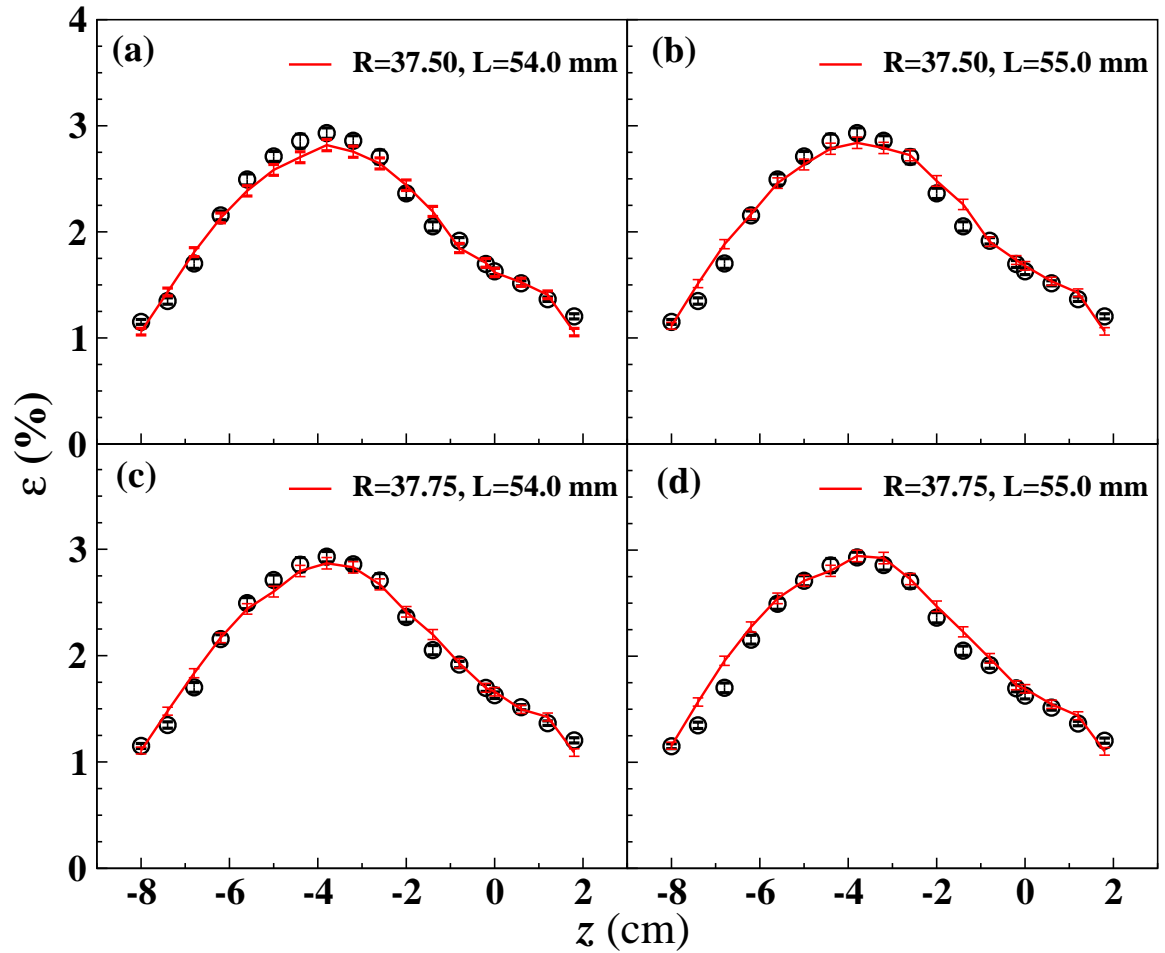


Figure 2.10: The absolute photopeak efficiency ε^{exp} (unfilled circles) of $E_\gamma = 1115.5$ keV as a function of z (lateral scan). The simulated values ε^{MC} (lines) for different combinations of radii (R) and lengths (L) are shown in panels (a) to (d).

Table 2.2: Total relative deviation σ_R as a function of R and L for both radial and lateral scans with $E_\gamma = 1115.5$ keV.

Radius mm	Length mm	σ_R (%)	Radius mm	Length mm	σ_R (%)
37.25	52.0	6.09(4)	37.50	51.0	6.33(5)
37.25	53.0	4.27(3)	37.50	52.5	4.87(3)
37.25	54.0	3.93(3)	37.50	53.0	3.88(3)
37.25	55.0	3.73(3)	37.50	54.0	3.67(2)
37.25	56.0	3.62(3)	37.50	55.0	3.71(2)
37.25	58.0	5.15(4)	37.50	56.0	4.58(3)
37.75	50.0	7.19(4)	38.00	50.0	5.89(2)
37.75	52.0	4.22(2)	38.00	52.0	3.71(2)
37.75	53.0	3.67(2)	38.00	53.0	3.67(2)
37.75	54.0	3.44(3)	38.00	54.0	3.85(3)
37.75	55.0	4.04(3)	38.00	55.0	4.89(3)
37.75	56.0	4.94(5)	38.00	56.0	5.99(2)

Figure 2.11 shows a pictorial representation of the σ_R for radial and lateral scan. It can be seen that the minimum is rather shallow. The projec-

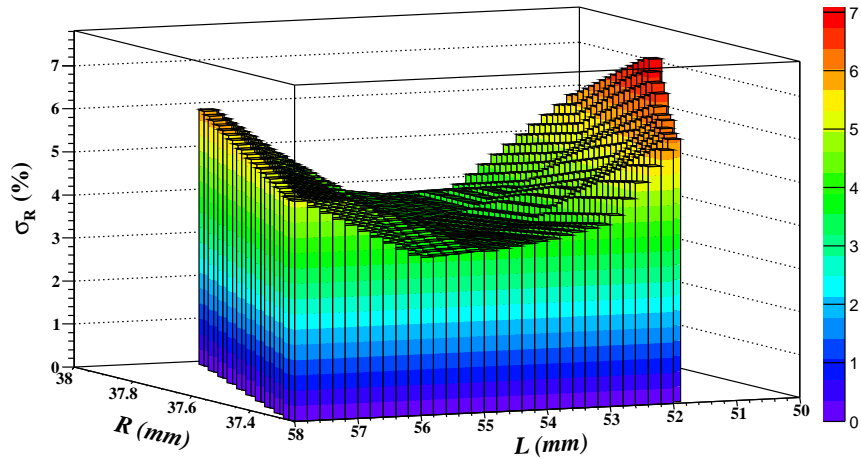


Figure 2.11: Total relative deviation σ_R as a function of R and L for both radial and lateral scans with $E_\gamma = 1115.5$ keV.

tions in L space corresponding to different values of R (37.25 mm to 38.00 mm) are shown in Figure 2.12. The R_{opt} and L_{opt} are then obtained from

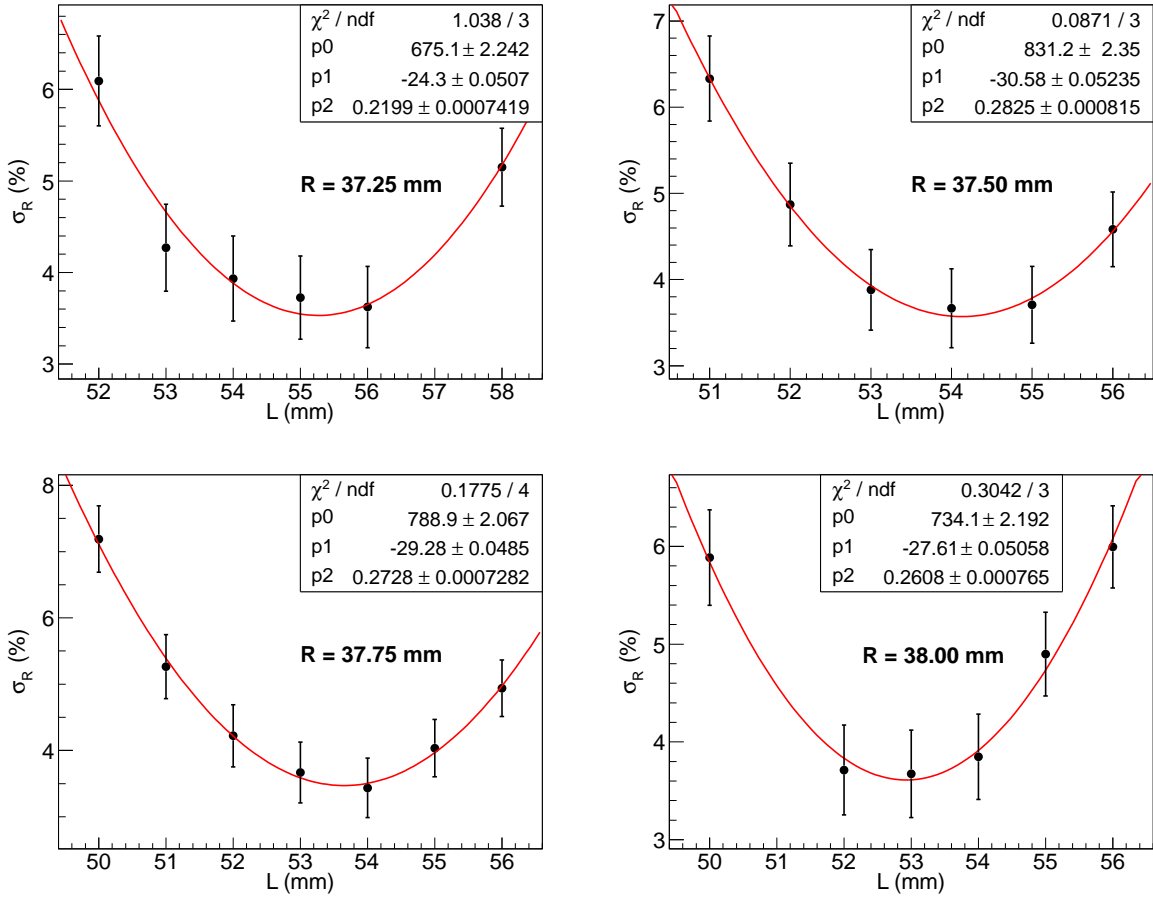


Figure 2.12: The σ_R for radial scan data of $E_\gamma = 1115.5$ keV as a function of L for a given R . Symbols represent experimental data and the line corresponds to the parabolic fit.

this weighted mean as $R_{opt} = 37.6 \pm 0.3$ mm and $L_{opt} = 54.0 \pm 0.9$ mm after rounding off to the first decimal place. The errors quoted are the standard deviations on the calculated quantities. With above values of R_{opt} and L_{opt} , the hole depth $L_h = 44.3 \pm 1.0$ mm was obtained corresponding to $L_{opt} - L_1$.

The remaining unknown parameter, hole radius h , was extracted from the distance scan with high energy γ -rays. From the best fit to the distance scan data (1–25 cm) of $E_\gamma = 834.8$ and 1115.5 keV, the h_{opt} was found to be 7.5 ± 0.6 mm. As mentioned earlier, the bottom dead layer b_{opt} was set to the difference between L_m and L_{opt} . Table 2.3 gives a complete list of optimized parameters of the detector.

Table 2.3: Optimized parameters of the detector.

Detector Parameter	Nominal (mm)	Optimized (mm)
Ge crystal radius (R)	38.45	37.6 ± 0.3
Ge crystal total length (L)	63.0	54.0 ± 0.9
Ge disc thickness (L_1)	12.3	9.7 ± 0.5
Hole depth ($L - L_1$)	50.7	44.3 ± 1.0
Hole radius (h)	5.5	7.5 ± 0.6
Top Ge Dead Layer (t)	-	1.04 ± 0.02
Side Ge Dead Layer (s)	0.7	1.26 ± 0.02
Bottom Ge Dead Layer (b)	-	9.0 ± 1.0
Front gap (g)	4	5.0 ± 0.7
Top carbon fiber*	0.9	0.9
Side carbon fiber*	1.8	1.8
Cu Cup thickness*	0.8	0.8
Ge Crystal Volume (V)	292 cm^3	$232 \pm 6 \text{ cm}^3$

* Not altered in MC simulations

Errors on the parameters have been estimated from the standard deviations on the calculated quantities. The quantities marked with an asterisk in Table 2.3 have not been altered in the MC simulations. The nominal parameters supplied by the manufacturer are also shown for the comparison.

2.4 Validation of the Effective Detector Model

The GEMS (GERmanium efficiency based on Monte carlo Simulations) is the program developed for MC simulation based efficiency computation for any source configuration in a close geometry, using the optimized detector parameters in Table 2.3. Figures 2.13, 2.14 and 2.15 show a comparison of experimental data for various energies together with simulation results employing the optimized detector parameters. For the lateral scan with low energy gamma-rays, addition of the bottom dead layer ($L_m - L_{opt} = b$) is crucial to reproduce the shape in $z = -9$ to -6 cm region (see Figures 2.13b and 2.14b). It should be mentioned that at low energy ($E_\gamma = 122.1$ keV), the effective linear dimension of the crystal (radius/length) seems to be lower than that for the high energy ($E_\gamma = 1115.5$ keV). This could be an effect of a non-uniform electric field at corners of the crystal [80] or the non-uniform dead layer [90] or the curvature of the crystal edges (which is neglected in the simulations) [76]. A comparison of data and simulation results for radial scans at $d \sim 10$ cm ($E_\gamma = 122.1$ and 1115.5 keV) is shown in Figure 2.16. Though the overall fit is good ($\sigma_R = 2.8(3)\%$), the simulated spectra seems to slightly overestimate the data at higher energies (see Figure 2.16). For both the close geometry and distance scans, an excellent agreement is observed between simulations and data. It should be mentioned that the cylindrical symmetry of the crystal was verified with $E_\gamma = 59.5$ keV by placing

the source in all four perpendicular directions close to the detector face. It should be noted that the energy threshold of the HPGe detector is ~ 40 keV.

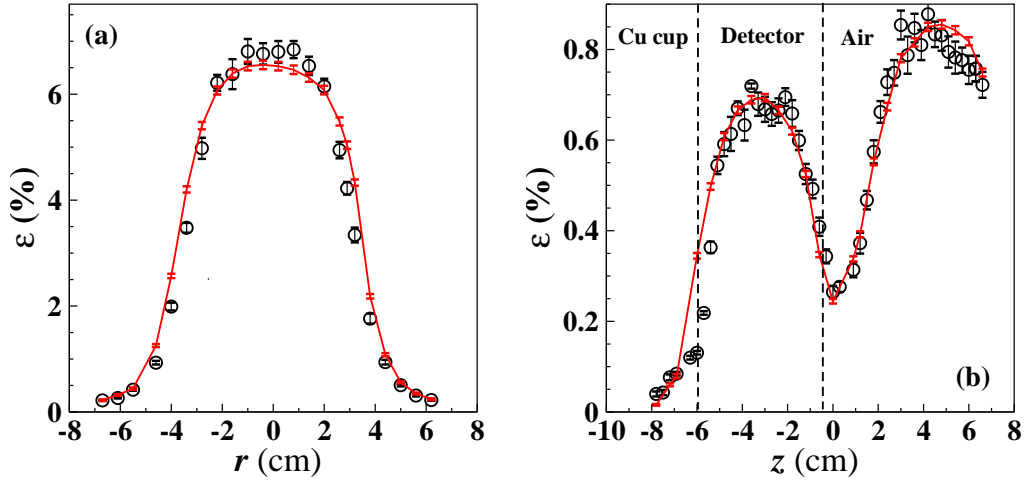


Figure 2.13: The radial (left panel) and lateral (right panel) scan data of $E_\gamma = 59.5$ keV with optimized detector parameters. Symbols represent the ϵ^{exp} and the line corresponds to ϵ^{MC} . The z range occupied by the crystal is marked in the figure.

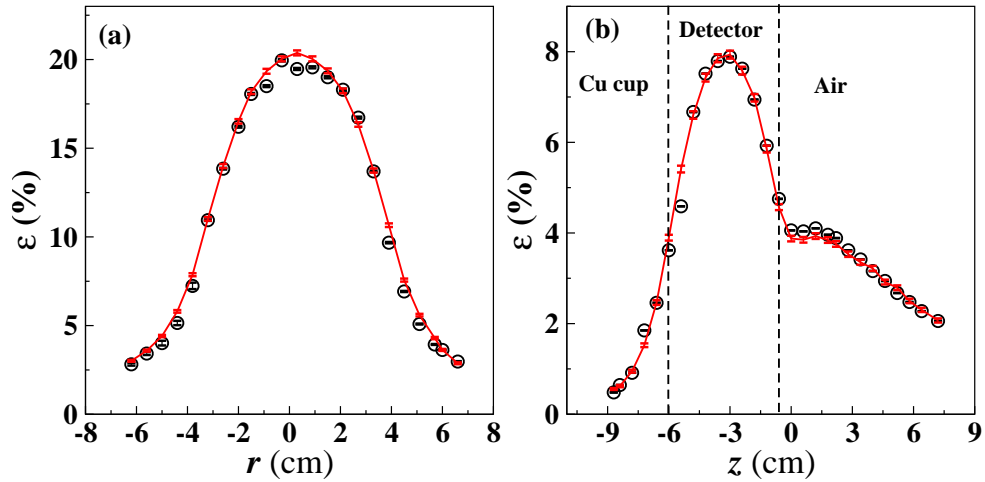


Figure 2.14: Same as Figure 2.13 for $E_\gamma=122.1$ keV

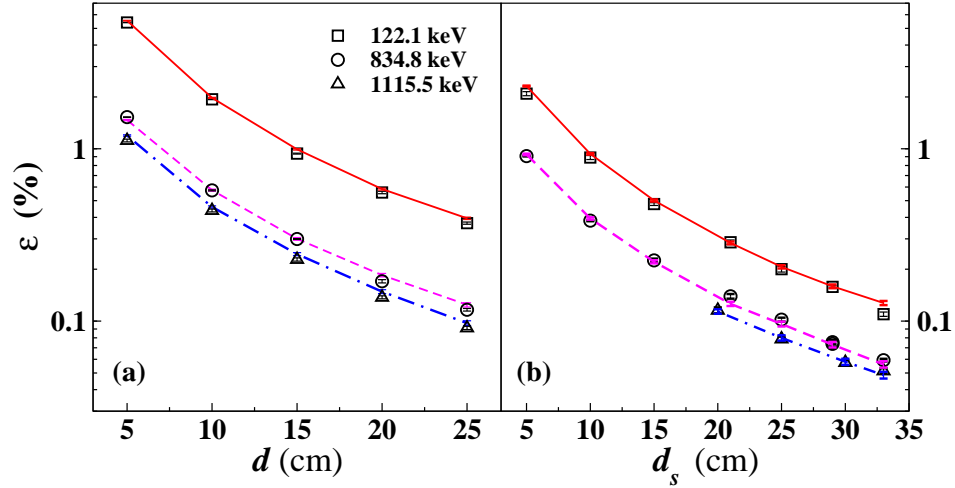


Figure 2.15: The top distance (left panel) and side distance (right panel) scan data of $E_\gamma = 122.1, 834.8$ and 1115.5 keV with optimized detector parameters. Symbols represent the ε^{exp} and the line corresponds to ε^{MC} .

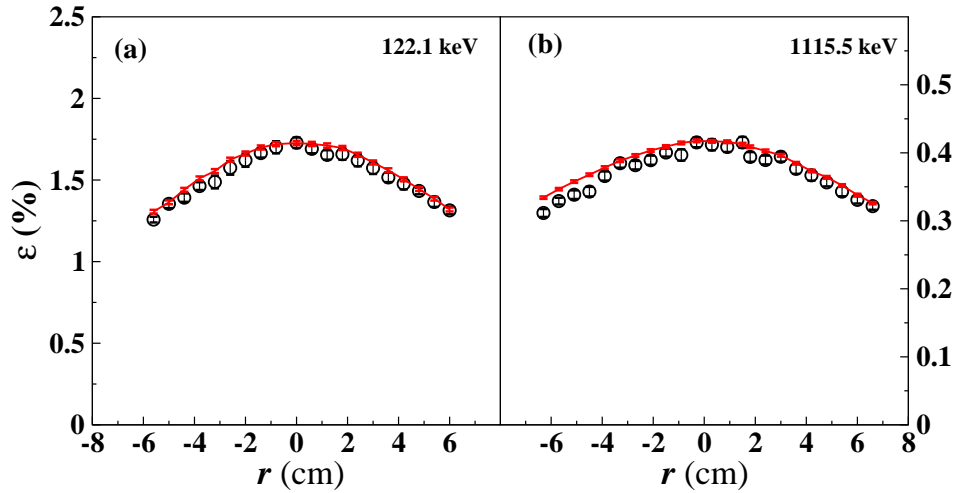


Figure 2.16: The radial scans data showing ε^{exp} (unfilled circles) and ε^{MC} (lines) for (a) $E_\gamma = 122.1$ keV and (b) $E_\gamma = 1115.5$ keV with optimized detector parameters at $d = 10.7$ cm.

The effective detector model was also used to simulate the volume source geometry ($E_\gamma = 661.7$ keV) and results are plotted in Figure 2.17. The excellent agreement between measured and simulated values indicate that the

optimized model works very well for different source geometries. The effective detector model is further tested with distance scan measurements with many sources, $E_\gamma = 59.5, 279.2, 1173.2$ and 1408 keV, and results are shown in Figure 2.18.

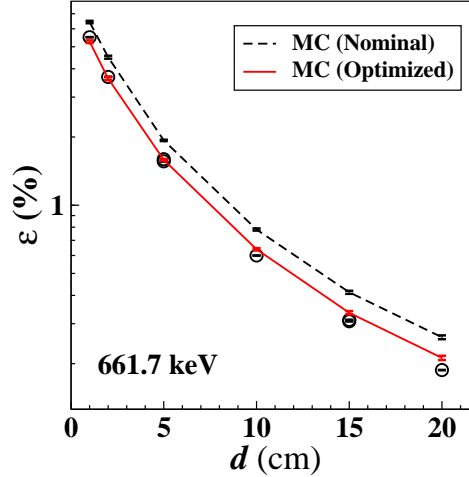


Figure 2.17: The ϵ^{exp} (unfilled circles) as a function of d for volume source geometry ($E_\gamma = 661.7$ keV). The ϵ^{MC} for both optimized parameters (bold line) and for nominal parameters (dashed line) is also shown for comparison.

It is evident from both these figures that the simulations are well able to reproduce the experimental data. Figure 2.19 displays the relative deviation σ_R for $E_\gamma = 122.1, 279.2, 834.8$ and 1115.5 keV as a function of $d = 5$ – 25 cm. It can be seen that the optimized model yields $\sigma_R = 5.46(3)\%$ as opposed to $29.2(3)\%$ obtained with nominal parameters. With inclusion of low energy data of $E_\gamma = 59.5$ keV, the σ_R worsens to $\sim 8.37(4)\%$. The measured energy spectra for ^{54}Mn source ($E_\gamma = 834.8$ keV) at $d_s = 25$ cm

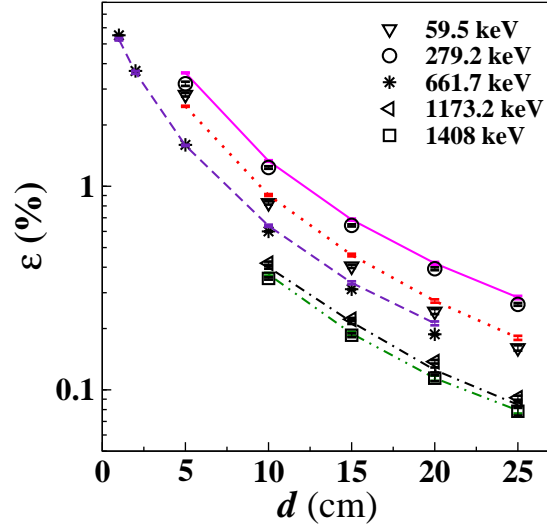


Figure 2.18: The ε^{exp} as a function of d for different gamma ray energies. Symbols represent the measured data and corresponding ε^{MC} with optimized parameters is shown by lines.

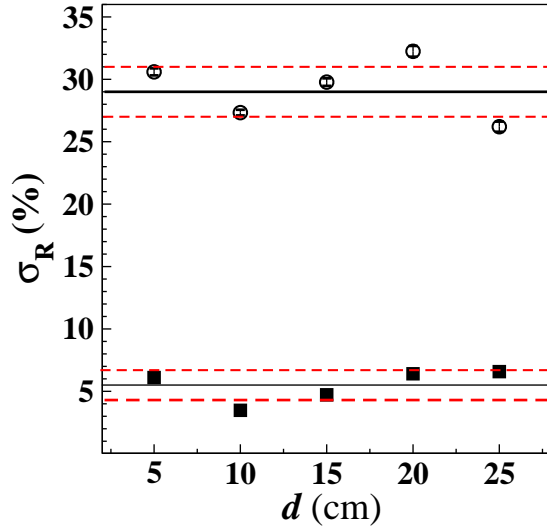


Figure 2.19: The relative deviation σ_R for $E_\gamma = 122.1, 279.2, 834.8$ and 1115.5 keV for $d = 5\text{--}25$ cm obtained with optimized detector parameters (filled symbols) and with nominal parameters (open symbols). The bold line is the average and the RMS deviation is indicated by dashed lines. Errors are within the point size.

and ^{137}Cs source ($E_\gamma = 661.7$ keV) at $d = 15$ cm is shown in Figure 2.20 together with the simulated spectrum after folding in energy resolution of the detector. The room background with suitable time normalization has been added to the simulated spectrum for comparison with experimental spectrum. Even though the detector model was optimized with photopeak efficiency, overall spectral shape including the Compton edge, is very well reproduced. However, a slight low energy tail in the experimental spectrum ($\sim 1.5\%$) as compared to MC simulations is visible.

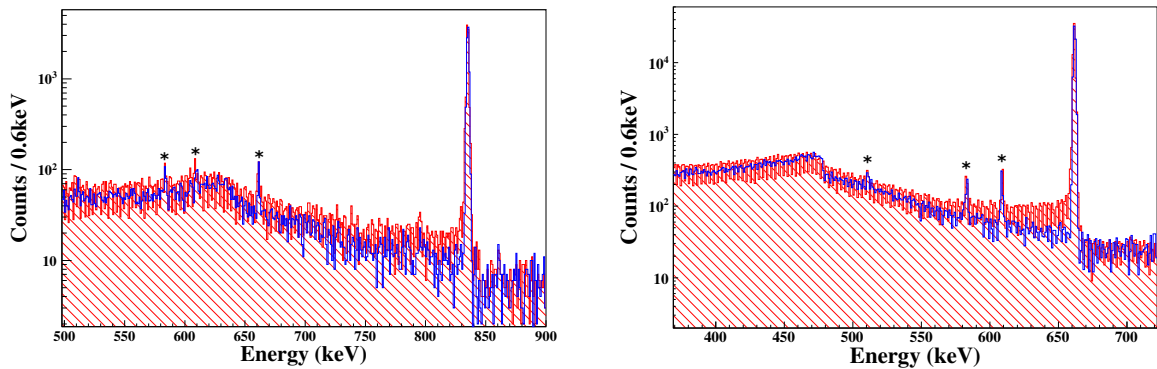


Figure 2.20: The measured energy spectra (filled red) for ^{54}Mn extended source ($E_\gamma = 834.8$ keV) at $d_s = 25$ cm (left panel) and ^{137}Cs volume source ($E_\gamma = 661.7$ keV) at $d = 15$ cm (right panel) together with the simulated spectra (blue) after folding in energy resolution of the detector. The room background with suitable time normalization has been added to the simulated spectrum for comparison. The gamma rays originating from room background are indicated with star symbols.

It should be mentioned that the detector has undergone two thermal cycles and an evacuation during three years of operation without any change in the performance (efficiency and resolution).

2.5 Summary

Detailed measurements are performed with point and extended geometry sources to generate an effective model of the detector with GEANT4 based Monte Carlo simulations. The active volume obtained is about 20% smaller than the nominal value supplied by the manufacturer. The effective detector model agrees within 5.46(3)% with experimental data over a wide energy range of 100–1500 keV. The GEMS program is developed for MC simulation based efficiency computation for any source configuration in a close geometry.

Chapter 3

Study of Gamma Background using the TiLES

3.1 Introduction

As explained in Chapter 1, the sensitivity of a $0\nu\beta\beta$ experiment critically depends on the background level in the region of interest. In order to reduce the internal background it is essential to have radio-pure materials in and around TIN.TIN detector. The detector material itself can be a potential source of background. Moreover, understanding the sources of the background in the surrounding materials is very crucial. Most of the double beta decay experiments have dedicated low background counting facility, often underground, for radio-purity checks in detector materials.

For investigating the background issues related to the development of TIN.TIN detector, a low background set up with HPGe detector, TiLES

(Tifr Low background Experimental Setup), has been installed at sea level at TIFR. This chapter describes the digital Data Acquisition System (DAQ) and the shielding configuration (both passive and active) around the HPGe detector. The results of the gamma ray measurements of low activity samples using the TiLES : Cu, Bodi West Hills (BWH) rock, Sn, Neutron Transmutation Doped (NTD) Ge sensors, Torlon and Teflon are presented.

3.2 Digital Data Acquisition System

Digital signal processing (DSP) is ideally suited for rare decay studies like $0\nu\beta\beta$ decay involving long counting periods. In a digitizer, a flash ADC directly samples and stores the preamplifier output, which is then processed by pulse height analyzing algorithms to extract energy information. Since fast sampling speeds for high precision ADCs and high speed FPGAs are available today, the digital DAQ can handle much higher throughput and consequently work as a “zero dead time” system. The DSP not only reduces requirement of electronics units and cabling but also eliminates temperature related drifts to a large extent and has a better noise immunity.

The DAQ of the TiLES is based on a commercial CAEN N6724 digitizer. This is a 14 bit, 100 MS/s digitizer with input dynamic range 2.25 V_{pp}. The algorithm implemented for pulse height analysis is based on trapezoidal filter (moving window de-convolution). The detector pulse is characterized

by an amplitude A , rise time t_{rise} and decay time t_{decay} . Figure 3.1 shows the parameters involved in the trapezoidal filter algorithm. The digitizer

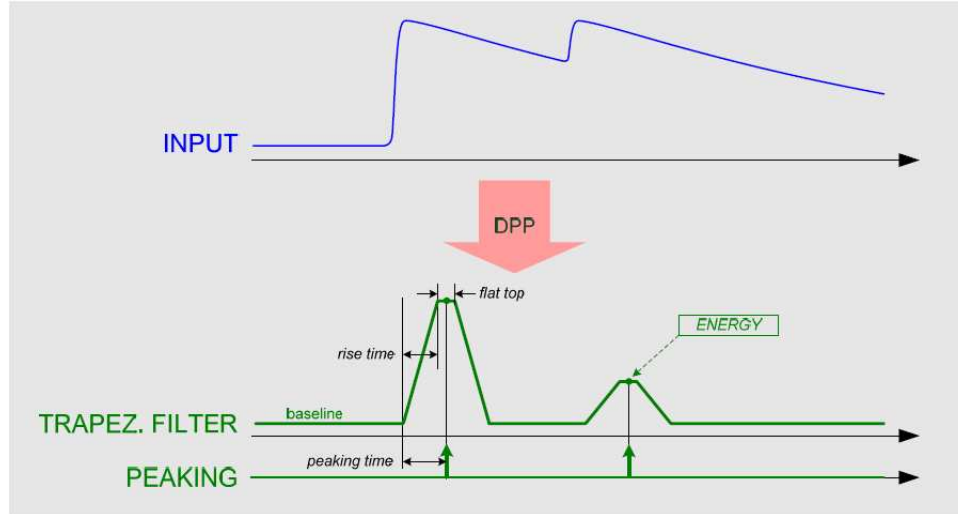


Figure 3.1: Trapezoidal filter with the relevant parameters [91].

parameters, namely, input signal decay time (T_{decay}), trapezoidal rise time (T_{rise}), trapezoidal flat top time ($T_{flattop}$) and Baseline Restorer (number of points for moving average) are optimized for best resolution. The T_{rise} is functionally equal to integration time of spectroscopic amplifier. Optimum pole-zero cancellation of trapezoidal signal is obtained by varying T_{decay} . It has been found that ballistic deficit error could be well compensated by setting $T_{flattop} \geq 3t_{rise}$. The moving average takes care of the jitter due to least count in signal digitization and baseline fluctuations. The $T_{flattop}$ is optimized to get best energy resolution and minimum pulse pile up. The

CAEN N6724 digitizer was tested with two different HPGe detectors, one is the TiLES (70% relative efficiency) and the other is Bruker Baltic make (30% relative efficiency). Table 3.1 gives optimum trapezoidal filter settings together with HPGe detector sizes and preamplifier output signal parameters.

Table 3.1: Optimum trapezoidal filter settings for two different detectors.

Detector	Dia.	L	Pulse shape parameters		Digital filter parameters		
	(mm)	(mm)	t_{rise} (ns)	t_{decay} (μs)	T_{rise} (μs)	T_{decay} (μs)	$T_{flattop}$ (μs)
Bruker Baltic (30%)	53	63	140	120	3.5	70	0.5
TiLES (70%)	78.3	63	400	150	5.5	50	1.5

It may be noted that T_{rise} and $T_{flattop}$ is higher for the larger HPGe detector as expected. A gamma ray spectrum of ^{152}Eu source recorded using the digitizer (bottom panel) and conventional analog electronics (top panel) is shown in Figure 3.2. A comparison of energy resolution (FWHM) obtained from two methods is given in Table 3.2. It can be seen that the energy reso-

Table 3.2: A comparison of energy resolution with analog and DSP.

Energy (keV)	Analog FWHM (keV)	Digitizer FWHM (keV)
121.7	1.44(2)	1.67(3)
778.9	1.87(5)	2.03(5)
1408.0	2.36(6)	2.31(5)

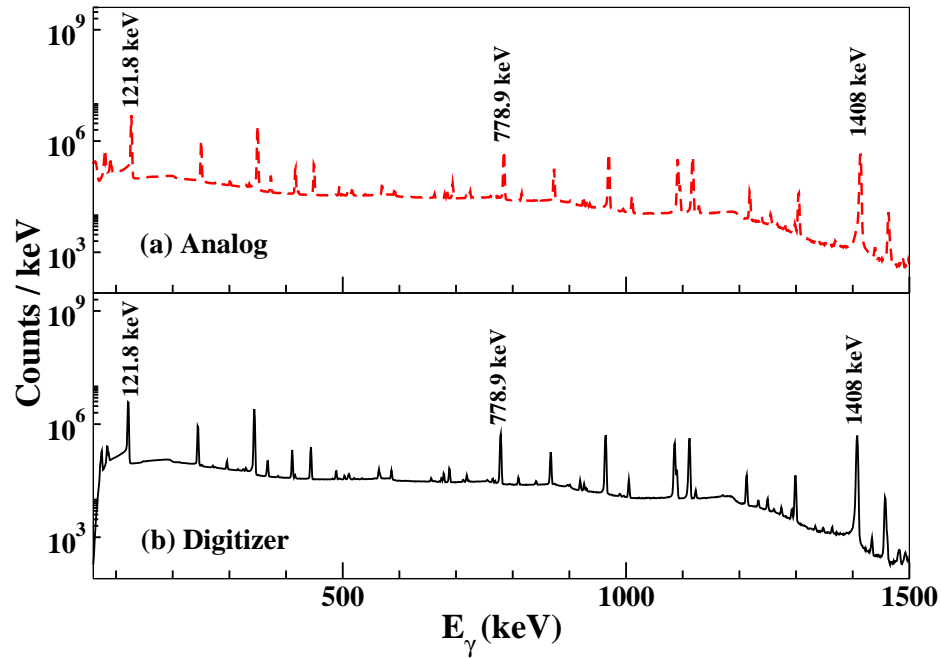


Figure 3.2: A comparison of gamma ray spectra with ^{152}Eu using (a) the analog electronics and (b) the CAEN digitizer.

lution obtained with digitizer is comparable to that with analog electronics. The energy resolution is better with digitizer at higher energy and slightly worse at lower energies. Moreover, peak positions show excellent stability against thermal drift in the data recorded in the digitizer over long duration (~ 15 d). The digitizer has also been tested with a standard pulse generator and dead time is found to be nearly zero up to counting rate of ~ 50 kHz. Figure 3.3 shows a spectrum for high activity ^{54}Mn source (~ 30000 dps) in a close geometry in the TiLES. The peak shape of 834.8 keV gamma ray with digitizer shows a considerable improvement. This clearly illustrates

the advantage of the DSP particularly for such large diameter HPGe detectors and high count rates. It is also evident that pile up corrections are more readily implementable in the digital domain.

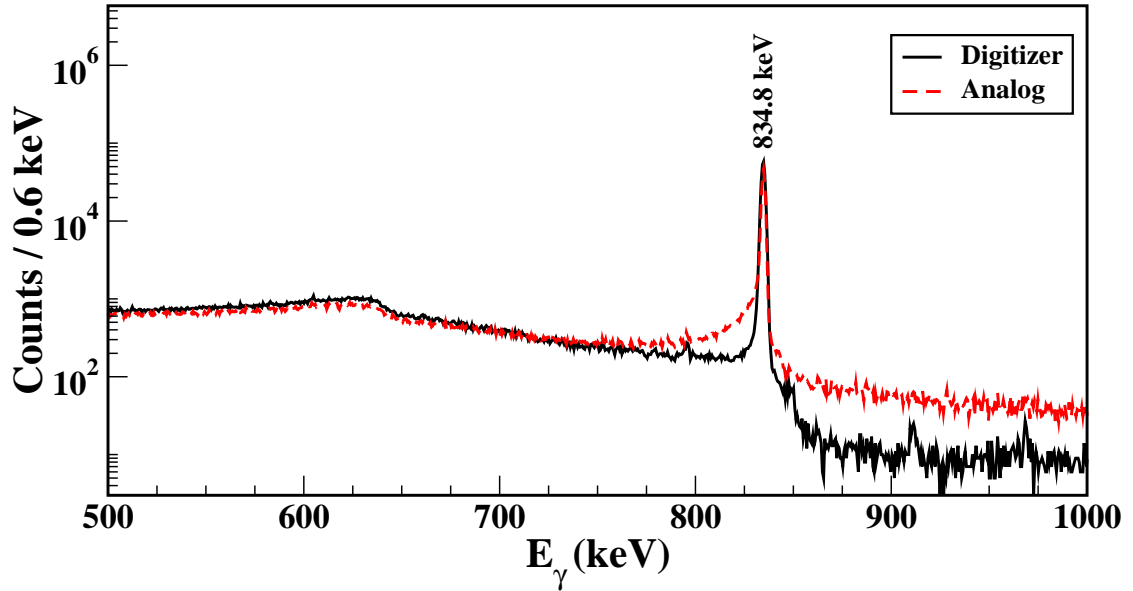


Figure 3.3: A comparison of the gamma ray spectra with ⁵⁴Mn using the CAEN digitizer (bold black line) and analog electronics (dashed red line). Both the spectra are normalized to constant time.

3.3 Shielding Arrangement for the HPGe Detector

As mentioned earlier, the low background HPGe detector has a 60 cm long cold finger attached to a J-shaped cryostat. This was chosen to facilitate the shielding arrangement around the HPGe detector. Also the activity from the preamplifier and HV filter does not come in the line of sight of the HPGe

crystal. The HPGe detector is placed ~ 1 m from the ground and at equal distance (~ 2 m) from the walls on all sides to reduce the activity from the walls of the laboratory (on the third floor).

3.3.1 Passive Shield

For attenuating gamma rays from surroundings, graded shielding arrangement is desirable. Lead is generally chosen as a shielding material for gamma rays due to its high density (11.34 g/cm^3) and high atomic number ($Z = 82$). The intensity of 3000 keV gamma ray falls to 0.06% and 0.001% after transmission through 10 cm and 15 cm thick Lead, respectively. The ^{210}Pb ($T_{1/2} = 22.2(2) \text{ y}$) contamination is present in Pb and its concentration depends on the origin of ore and manufacturing process. The decay of ^{210}Pb produces ^{210}Bi and ^{210}Po (see Figure 3.4). Subsequently, the beta

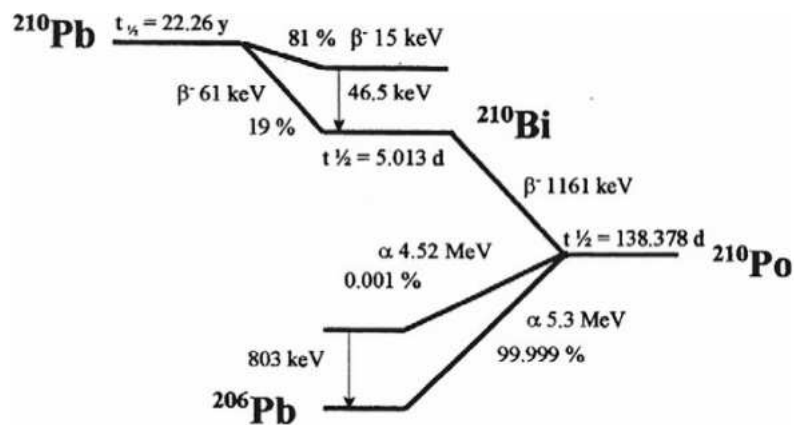


Figure 3.4: Decay Schemes of ^{210}Pb , ^{210}Bi and ^{210}Po [92].

emission of ^{210}Bi in Lead shielding produce a low energy bremsstrahlung continuum up to 1162 keV and also induce characteristic X-rays [93]. Archaeological Pb with lower intrinsic activity of ^{210}Pb is highly desirable for ultra-low background experiments like $0\nu\beta\beta$ decay. In the TiLES low activity Pb bricks ($^{210}\text{Pb} < 0.3 \text{ Bq/kg}$) of sizes $20 \text{ cm} \times 10 \text{ cm} \times 5 \text{ cm}$ and $10 \text{ cm} \times 10 \text{ cm} \times 5 \text{ cm}$ procured from Lemer Pax (France) are used for providing a 10 cm thick cover on all sides. To reduce the background originating from the bremsstrahlung radiation of ^{210}Bi and X-rays from the outer Pb shield, an inner layer with lower Z is used. The thickness of the inner shield (low Z) is constrained because :

- The background of the HPGe detector installed at sea level is dominated by the muon-induced interactions in the surrounding materials. Additional materials may increase cosmic-ray induced activity.
- Increase of Compton scattering in the inner layer and probability of gamma rays scattering towards the HPGe detector is high for $E_\gamma < 500 \text{ keV}$.
- The outer Pb shield requirement increase in proportion to the inner low Z shield thickness. The overall shield size is also constrained by overall weight limitations of the setup and load capacity of the lab floor.

Copper ($Z = 29$) was chosen for inner shield because of its ease of availability and lower neutron capture cross-section. A 5 cm thick inner shield of low activity OFHC (Oxygen Free High Conductivity) Cu rings procured from Leico Industries, USA (selected on the basis of radio-purity) has been added to the setup. The intensity of 1000 keV gamma ray falls to $\sim 5\%$ after transmission through 5 cm thick Cu and hence is expected to be adequate for attenuating bremsstrahlung from ^{210}Bi .

3.3.2 Active Shield

The background of the HPGe detector installed at sea level is dominated by the muon-induced interactions in the surrounding high Z shield materials (Cu + Pb). Muons are minimum ionizing particles (mip) with a typical energy loss of $\sim 2 \text{ MeV}/(\text{g cm}^{-2})$ in any material. The muon-induced background can be reduced by rejecting these events using a plastic scintillator around the detector. The plastic scintillators ($50 \text{ cm} \times 50 \text{ cm} \times 1 \text{ cm}$) were cast at the Cosmic Ray Laboratory (TIFR), Ooty, India. Each scintillator was coupled through a light guide to a single PMT (Photonis XP2262/B) operated at a voltage -1800 V . Figure 3.5 shows a schematic of the TiLES with two plastic scintillators P1 and P2. The incoming muon may interact in the Cu/Pb shield and the gamma produced can deposit energy in the HPGe crystal. However due to higher attenuation of gamma rays in Pb ($Z = 82$)

than Cu ($Z = 29$) and Cu being nearer to the HPGe detector, the interactions originating in Cu will contribute more to the muon-induced background in the HPGe detector.

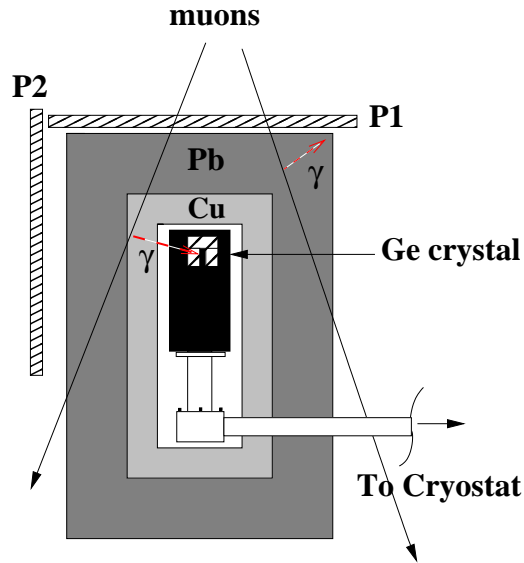


Figure 3.5: A schematic of the TiLES with the plastic scintillators P1 and P2 arranged in configuration I (see text for details).

The fast signal of the plastic scintillator was fed through a custom designed amplifier to the input of the digitizer. The data from the HPGe detector and plastic scintillators was recorded in the list mode on event-by-event basis with a time stamp. A program has been developed for the implementation of anti-coincidence between the HPGe detector and plastic scintillators, CADFLAP (CAen Digitiser oFFLine Anti-coincidence Program). The anti-coincidence window can be adjusted in the program and is defined to be $\pm 2.5 \mu\text{s}$. The window was selected to ensure complete overlap between

the Ge and scintillator input signals. If the HPGe and plastic scintillator events fall within this window, the corresponding HPGe events were rejected. The program generates the coincidence, anti-coincidence and time spectra which can be analyzed with LAMPS [84]. Figure 3.6 shows a time profile between the HPGe and plastic scintillator signals within the anti-coincidence window. It is clear that the preset time window is adequate to cover all coincidence events.

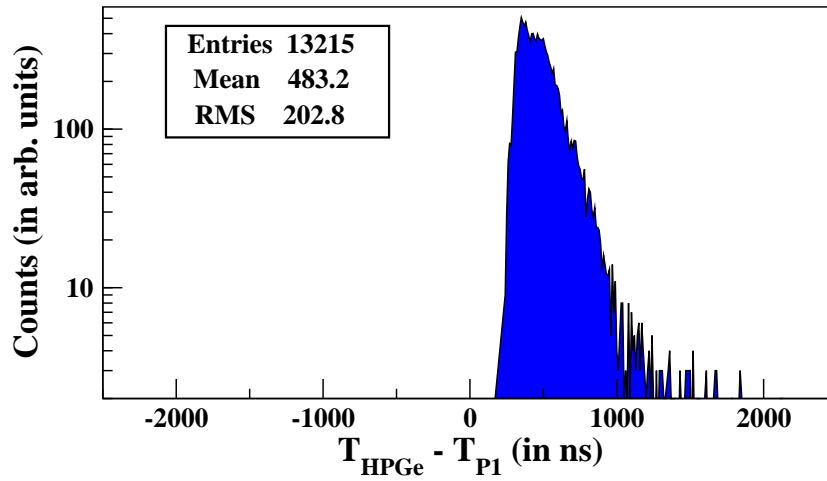


Figure 3.6: Time profile between HPGe and plastic scintillator signal.

It was ensured that the threshold of the scintillator was set above the noise level and the genuine HPGe events were not lost. Also, a 10 Hz pulser was added to monitor the random coincidence rate (r) defined as:

$$r = r_1 \times r_2 \times \Delta T \quad (3.1)$$

where r_1, r_2 are the rates of the pulser and plastic scintillator, respectively. The ΔT is the width of the coincidence window. Figure 3.7 shows that the observed and the expected random coincidence rate (r) between the pulser and scintillator are in good agreement as a function of the set threshold of the plastic scintillator.

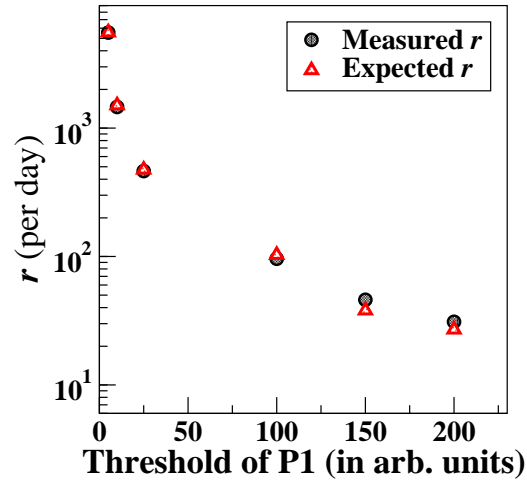


Figure 3.7: Comparison of the observed and the expected random coincidence rate (r) between the pulser and scintillator as a function of the energy threshold of P1.

The cosmic suppression factor (R) for the gamma background is defined as,

$$R = \left(1 - \frac{N_{HPGe} \cdot \bar{N}_{Plastic}}{N_{HPGe}}\right) \times 100\% \quad (3.2)$$

where N_{HPGe} and $N_{Plastic}$ are the events in the HPGe detector and plastic scintillator, respectively. The reduction ratio R depends on the solid angle coverage of the muon flux and hence on the mounting geometry of the HPGe

detector and plastic scintillators. It is desirable to cover all sides of the detectors with active veto shield. In the TiLES, two plastic scintillators have been used which give coverage of ~ 0.72 sr.

3.4 Study of Ambient Background with the TiLES

The gamma background in the TiLES was studied and monitored over a period of three years. It should be mentioned that the shielding arrangement around the detector described in the previous section was installed in phases. In stage I, 10 cm low activity Pb shield was setup around the HPGe detector. In stage II, inner Cu shield was added and finally the active veto system comprising plastic scintillators was installed (Stage III). Figure 3.8 shows a picture of the TiLES with complete shielding arrangement. The total weight of the TiLES is ~ 1650 kg (including Cu + Pb + Mild Steel support table). Figure 3.9 shows the gamma ray spectra of room background with and without 10 cm thick low activity Pb shield (TiLES-Stage I). The reduction in the intensity of the background gamma rays with addition of Pb shield is listed in Table 3.3.



Figure 3.8: A picture of the TILES with complete shielding arrangement.

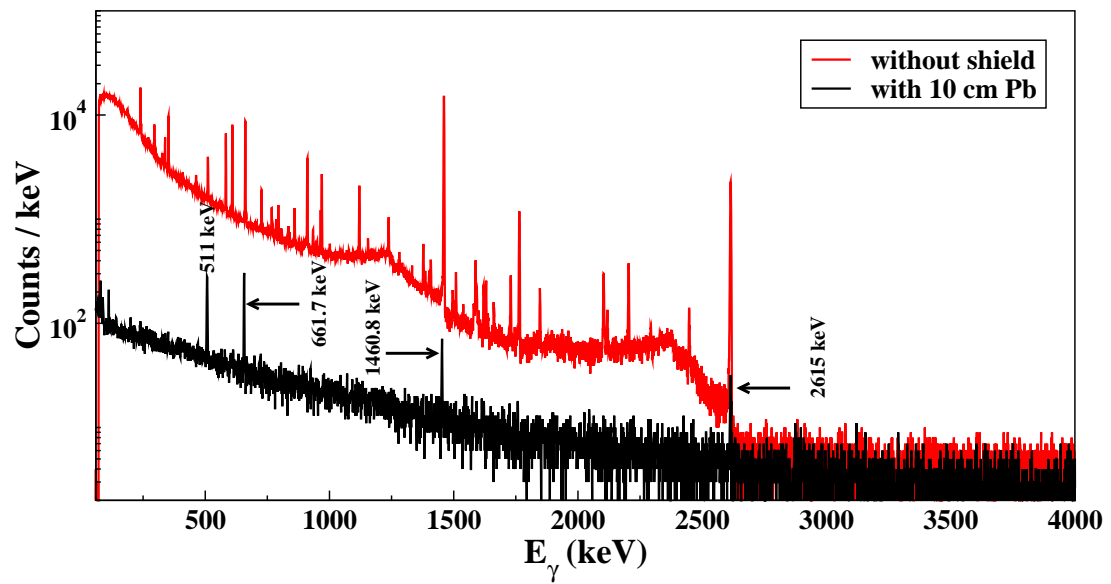


Figure 3.9: Gamma ray spectra of room background with (black lines) and without (red lines) Pb shield ($T_{data} = 1$ d).

Table 3.3: Reduction in intensity of the major gamma rays with 10 cm Pb shield.

Energy (keV)	Radio-isotopes	Without shield (A) (counts/day)	With Pb shield (B) (counts/day)	Reduction factor B/A(%)
238.6	^{212}Pb	44839(680)	64(15)	0.14(3)
351.9	^{214}Pb	30709(394)	17(7)	0.06(2)
511.0	$^{208}\text{Tl}, ^{40}\text{K}, \text{ann.}^*$	14995(407)	959(28)	6.4(3)
609.3	^{214}Bi	33721(264)	33(11)	0.10(3)
661.7	^{137}Cs	35325(427)	243(12)	0.69(3)
806.4	^{214}Bi	931(121)	13(6)	1.4(7)
835.6	^{228}Ac	1232(215)	10(5)	0.8(4)
1173.2	^{60}Co	3208(202)	22(6)	0.7(2)
1332.5	^{60}Co	3202(210)	16(6)	0.5(2)
1460.8	^{40}K	114330(1356)	134(8)	0.12(1)
1764.5	^{214}Bi	9617(156)	19(5)	0.20(5)
2614.5	^{208}Tl	24326(74)	96(7)	0.39(3)

* 511 keV gamma rays can also originate from annihilation process due to different β^+ emitters.

Figure 3.10 shows a further reduction seen in prominent background gamma rays with the addition of 5 cm thick low activity Cu shield (TiLES Stage II). It is observed that the background in the low energy region is enhanced with addition of Copper. This is due to the increased Compton scattering in the Cu shield which is also verified with GEANT4 simulations. It is also seen that the background above 2 MeV is slightly worsened due to cosmic ray interactions (as expected at sea level). The intensity reduction factors for prominent gamma rays and energy windows of interest are listed in Table 3.4.

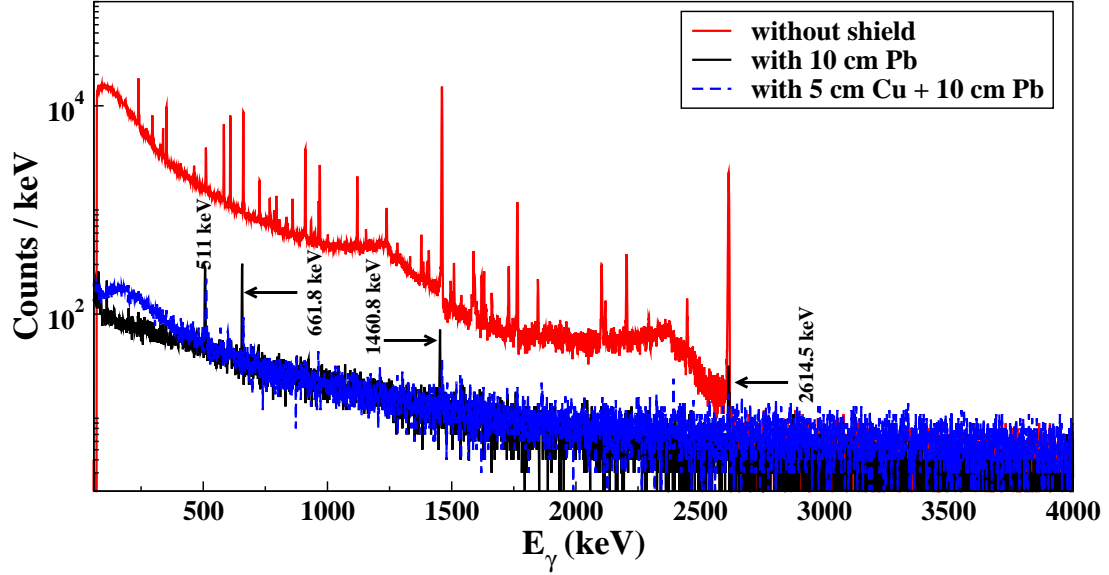


Figure 3.10: Gamma ray spectra of room background with 5 cm Cu + 10 cm Pb (blue lines), with only Pb (black lines) and without shield (red lines) ($T_{data} = 1$ d).

Table 3.4: Reduction in intensity of major gamma rays with 5 cm Cu + 10 cm Pb

Energy (keV)	Radio-isotopes	With Pb shield X (counts/day)	With Cu + Pb shield Y (counts/day)	Reduction factor Y/X (%)
70-500		32835(181)	46951(72)	143(1)
511.0	$^{208}\text{Tl}, ^{40}\text{K}, \text{ann.}$	959(28)	596(21)	62(3)
661.7	^{137}Cs	243(12)	125(9)	51(5)
1460.8	^{40}K	134(8)	49(7)	37(6)
2614.5	^{208}Tl	96(7)	14(6)	15(6)
2000-2500		3813(62)	4207(72)	110(3)

The room/ambient background spectra obtained in anti-coincidence with plastic scintillators is shown in Figure 3.11. A total gamma background reduction of $\sim 50\%$ in the region of 200–3000 keV is obtained by the addition of cosmic veto shield to the setup.

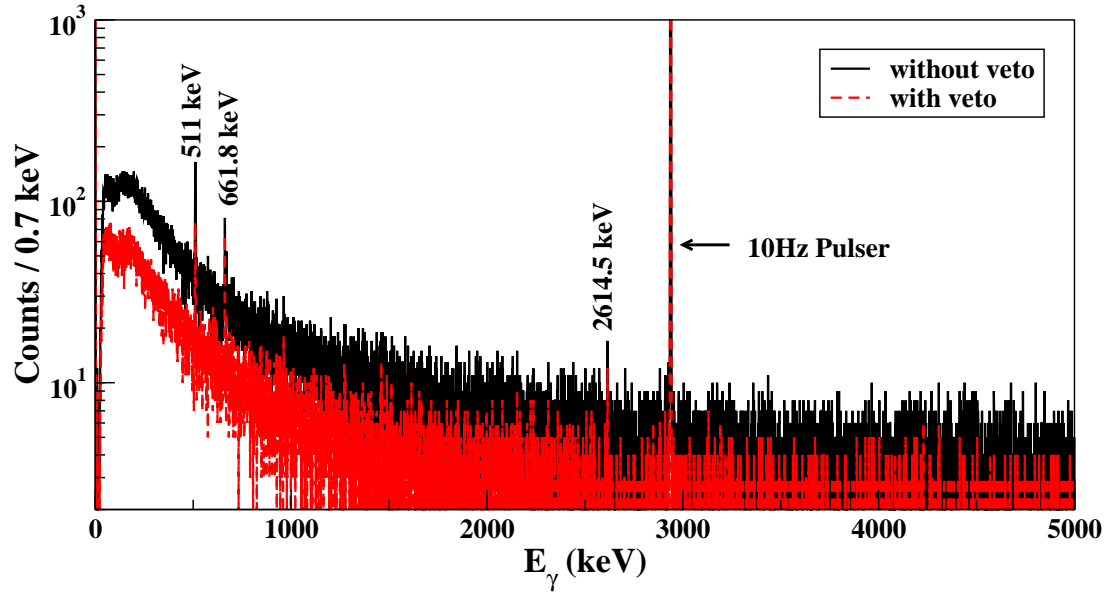


Figure 3.11: Gamma ray spectra of room background in the HPGe detector with veto (red dotted lines) and without veto (black solid lines) in the energy range of 200 – 5000 keV ($T_{data} = 1$ d).

Due to the saturation of the HPGe preamplifier around ~ 55 MeV, the events corresponding to the muons traversing the entire length of the HPGe crystal (~ 6 cm) could not be observed. It should be mentioned that two configurations of plastic scintillator were studied. Configuration I is shown in Figure 3.5 while the configuration II had the plastic scintillator (P2) at the bottom of the shield, at a distance of 71 cm from the center of the HPGe detector. The latter gave 10% lower reduction ratio in the range of 200–3000 keV. Table 3.5 gives reduction ratio (R) for different energy ranges in the background gamma ray spectra.

Table 3.5: Reduction ratio (R) for different energy regions for the two configurations of the setup geometry.

Energy Range (keV)	R (I) (%)	R (II) (%)
200–3000	52.1(0.4)	40.5(0.3)
3000–5000	54.7(1.5)	40.8(1.0)
5000–25000	61.2(0.5)	41.4(0.5)

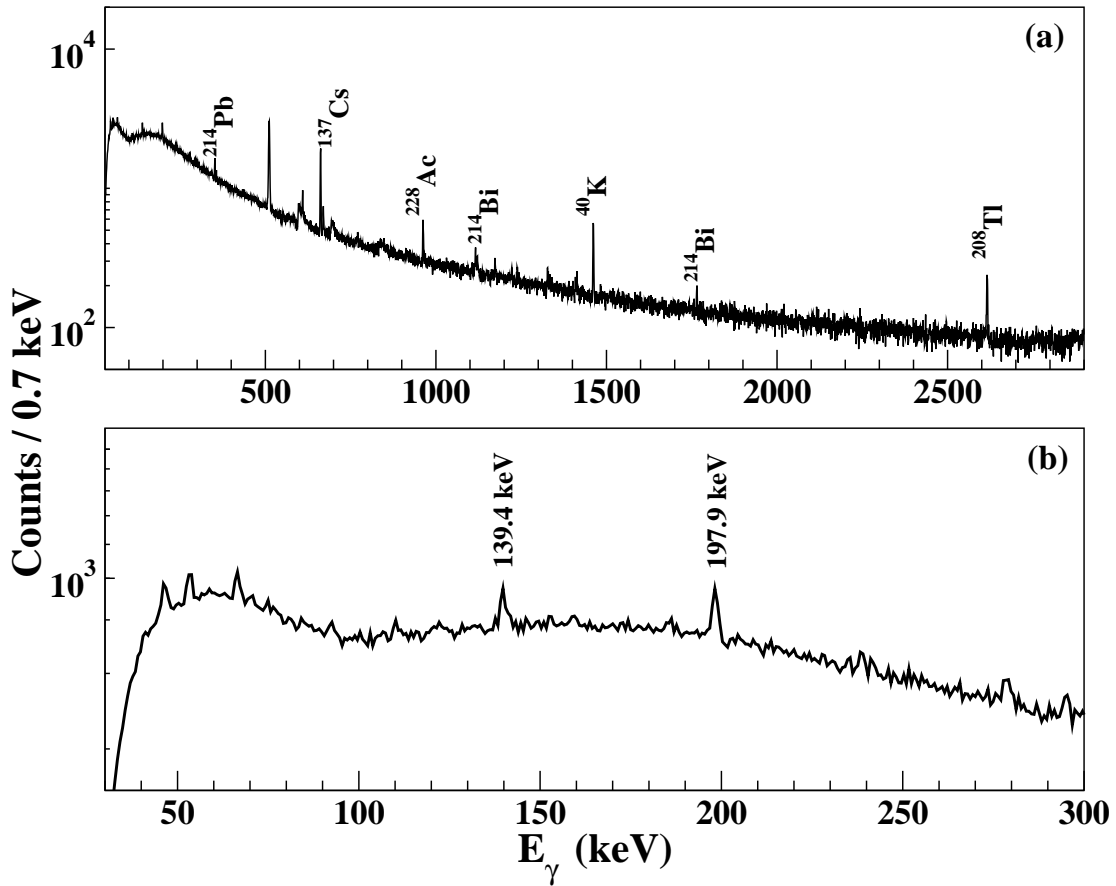


Figure 3.12: (a) The ambient background gamma ray spectra measured in the TiLES with full shield - Cu + Pb + active veto system ($T_{data} = 42.6$ d). The expanded view showing the 139.4 keV and 197.9 keV gamma rays from $^{74}\text{Ge}(n, \gamma^n)$ and $^{70}\text{Ge}(n, \gamma^n)$ reactions, respectively is shown in panel (b).

Figure 3.12(a) shows the background gamma ray spectra recorded in the TiLES for a continuous period of ~ 42 d. Figure 3.12(b) shows the expanded view where 139.4 keV and 197.9 keV gamma rays are clearly visible. The intensity of the prominent gamma rays with Cu + Pb + muon veto system is given in Table 3.6.

Table 3.6: Intensity of prominent gamma rays in TiLES with full shield - Cu + Pb + active veto system.

Energy (keV)	Reaction Channels/ Radio-isotopes	Observed Activity (counts/day)
139.4	$^{74}\text{Ge}(n, \gamma^m)^{75}\text{Ge}$	34(6)
197.9	$^{70}\text{Ge}(n, \gamma^m)^{71}\text{Ge}$	43(5)
351.9	^{214}Pb	26(4)
511.0	$^{208}\text{Tl}, ^{40}\text{K}, \text{ann.}$	291(7)
594.4-604.9*	$^{74}\text{Ge}(n, n'\gamma)^{74}\text{Ge}$	34(1)
609.3	^{214}Bi	21(2)
661.7	^{137}Cs	113(3)
669.6	$^{63}\text{Cu}(n, n'\gamma)^{63}\text{Cu}$	17(2)
690.1-704.2*	$^{72}\text{Ge}(n, n'\gamma)^{72}\text{Ge}$	33(1)
962.1	$^{63}\text{Cu}(n, n'\gamma)^{63}\text{Cu}$	26(3)
1115.5	$^{65}\text{Cu}(n, n'\gamma)^{65}\text{Cu}$	12(2)
1120.5	^{214}Bi	9(1)
1173.2	^{60}Co	6(2)
1332.5	^{60}Co	4(1)
1460.8	^{40}K	36(2)
1764.5	^{214}Bi	6(1)
2614.5	^{208}Tl	18(2)

* Asymmetric and broadened peak.

It is clearly seen that the ambient spectra is dominated by U, Th and ^{40}K but ^{137}Cs is also observed. In addition, gamma rays produced by de-excitation from the metastable state formed on thermal neutron capture via reactions $^{74}\text{Ge}(n, \gamma^m)$, $^{70}\text{Ge}(n, \gamma^m)$ were observed in the background spectra [94]. The sensitivity of the TiLES with the full existing shield and $T_{data} = 6 d$ is ~ 1 mBq/g for ^{232}Th , ~ 2 mBq/g for ^{40}K .

3.5 Radio-purity Measurements

Several materials like Cu, BWH rock, Sn, NTD Ge sensors, Torlon, Teflon have been counted in a close counting geometry in the TiLES for the investigation of trace radio-impurities. For the gamma rays observed in excess of the background, the activity N_x is estimated using Eq. 3.3 after correcting for the ambient background:

$$N_x = \frac{N_{\text{obs}}}{\epsilon_\gamma \times I_\gamma \times m} \quad (3.3)$$

where N_{obs} is the observed yield of the γ -ray, ε_γ is the photopeak detection efficiency computed using GEMS [95], I_γ is the branching fraction of the respective γ -ray and m is the mass of the measured sample. It should be mentioned that in some cases where I_γ could not be directly obtained, it is assumed to be 1. In cases where no activity could be observed above the sensitivity of the setup, only a limit could be set on the observed radio-impurities. For close geometry counting, the TiLES has a provision to mount sample at $d \sim 1$ cm from the top face of the HPGe detector and total space available for sample is $9 \text{ cm} \times 9 \text{ cm} \times 5 \text{ cm}$. For mounting the sample, Teflon and Perspex both having low density, low Z and good mechanical strength were considered. It was found that Teflon has a lower yield of 2614.5 keV γ -ray as compared to the Perspex. Hence, Teflon plate is used as the sample mount in all measurements and the mounting arrangement is shown in Figure 3.13.

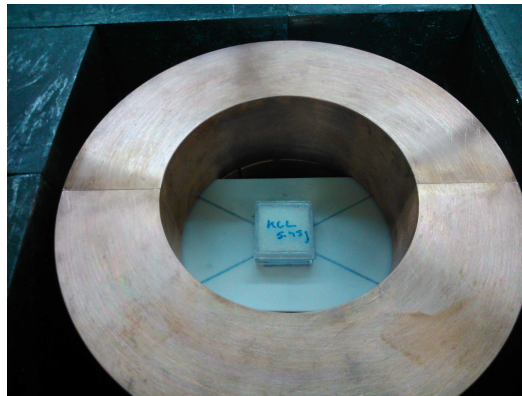


Figure 3.13: A typical mounting arrangement of a sample in the TiLES for counting in a close geometry (with top Cu + Pb shield removed).

Since the shielding arrangement was constructed in stages, measurements on various samples reported here were carried out in different shield stages and is specified in each case. It should be mentioned that although the materials to be used in TIN.TIN will be in large quantity ($\sim 1 - 100$ kg) at this initial R&D stage various samples studied were of small size (\sim mg – few g), mostly because of limited availability.

3.5.1 Cu Samples

In order to choose the radio-pure Copper for inner shield, Cu samples (see Table 3.7) were measured in the TiLES only with 10 cm Pb shield. The Electrolytic Tough Pitch (ETP) Cu (2N purity) was also chosen since

Table 3.7: Details of different Copper samples investigated for inner shield.

Sample	Mass (g)	Source
ETP Cu	13.2	Aurubis, Europe
OFHC Cu (A)	7.3	Leico Industries, USA
OFHC Cu (B)	2.6	Sequoia Brass and Copper, USA
OFHC Cu (C)	7.1	Non Ferrous materials Technology Development Centre (NFTDC), Hyderabad

the cryostat of TIN.TIN detector is made of the same material. The observed radio-impurities in the Cu samples are listed in Table 3.8. It can be seen that both OFHC Cu (A) and OFHC Cu (C) have similar levels of radioactivity, but the OFHC Cu (A) sample has lower ^{40}K concentration.

Table 3.8: Observed radio-impurities in different Cu samples (with 10 cm Pb shield).

Energy (keV)	ETP Cu (counts/ day g)	OFHC Cu (A) (counts/day g)	OFHC Cu (B) (counts/day g)	OFHC Cu (C) (counts/day g)
139.4	32 (12)	11(5)	13(6)	8(1)
197.9	29(9)	6(3)	28(5)	9(1)
511.0	835(30)	119(5)	365(9)	133(2)
609.3	51(16)	7(2)	18(5)	–
1460.8	138(9)	19(2)	58(4)	24(1)
1764.5	29(4)	4(1)	9(2)	–
2614.5	88(7)	13(1)	39(4)	15(1)

Hence the OFHC Cu (A) sample was chosen for the inner shield of the TiLES. Figure 3.14 shows a spectrum of the ETP Cu sample together with the background spectrum, clearly indicating many gamma rays above the background level.

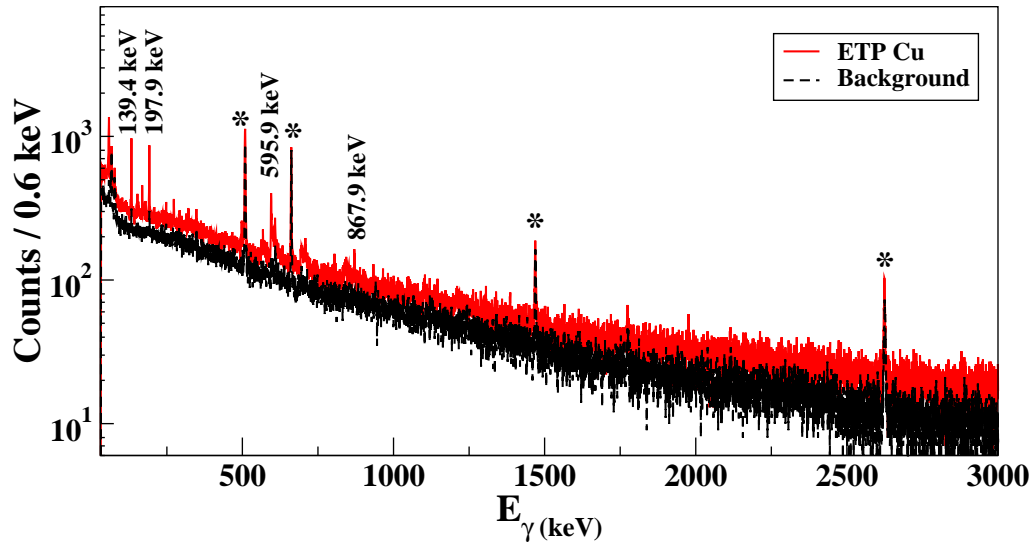


Figure 3.14: A gamma ray spectrum (red bold line) of the ETP Cu sample in the TiLES (only with 10 cm Pb shield, $T_{data} = 6$ d). The ambient background without the sample (black dotted line) is also shown for comparison and prominent lines are indicated with stars.

The observed gamma rays together with their origins and the corresponding measured activity are given in Table 3.9. Although the observed gamma

Table 3.9: Prominent gamma rays observed in the ETP Cu sample with 10 cm Pb shield.

Energy [0.5ex] (keV)	Reaction Channels/ Radio-isotopes	Observed Activity	
		(counts/day)	(mBq/g)
139.4*	$^{74}\text{Ge}(n, \gamma^m)$	310(75)	4.6(1.1)
159.3	$^{63}\text{Cu}(n, \gamma)$	56(14)	1.7(4)
186.0	$^{65}\text{Cu}(n, \gamma)$	51(13)	0.7(2)
175.1	$^{70}\text{Ge}(n, \gamma)$	56(14)	0.8(2)
197.9*	$^{70}\text{Ge}(n, \gamma^m)$	301(69)	4.0(9)
278.2	$^{63}\text{Cu}(n, \gamma)$	69(12)	1.4(3)
326.0	$^{72}\text{Ge}(n, \gamma)$	76(18)	3.9(9)
385.8	$^{65}\text{Cu}(n, \gamma)$	16(6)	0.6(2)
499.9	$^{70}\text{Ge}(n, \gamma)$	65(15)	1.5(3)
511.0*	$^{208}\text{Tl}, ^{40}\text{K}, \text{ann.}$	281(11)	6.3(3)
595.9	$^{73}\text{Ge}(n, \gamma)$	178(18)	3.9(4)
608.4	$^{73}\text{Ge}(n, \gamma)$	58(11)	7(1)
708.5	$^{70}\text{Ge}(n, \gamma)$	30(11)	1.6(6)
802.2*,#	–	39(10)	1.2(3)
867.9	$^{73}\text{Ge}(n, \gamma)$	52(11)	2.7(6)
961.1	$^{73}\text{Ge}(n, \gamma)$	9(4)	2.1(9)
1326.9*	$^{63}\text{Cu}(n, n'\gamma)$	9(6)	0.4(2)

* The branching fractions have been taken as 1.

Unidentified gamma ray

rays are at much lower energies than the ROI, i.e. near the $Q_{\beta\beta}$ (^{124}Sn), the coincidence summing and pile up of low energy gamma rays can contribute to the background in the ROI. It can be seen that the overall background level in the spectra with the ETP Cu sample is higher as compared to the

ambient background. Hence, it will be essential to have a Pb shield around the Tin detector array inside the cryostat in TIN.TIN.

3.5.2 Bodi West Hills (BWH) Rock

A rock sample (mass ~ 23 g) bored from the depths of Bodi West Hills, the site for INO cavern, was counted in the TiLES only with 10 cm Pb shield. Figure 3.15 shows a spectrum of the rock sample together with the background spectrum, clearly indicating the higher ^{40}K content in the sample [95]. The estimated impurities in the BWH rock sample from the γ -rays

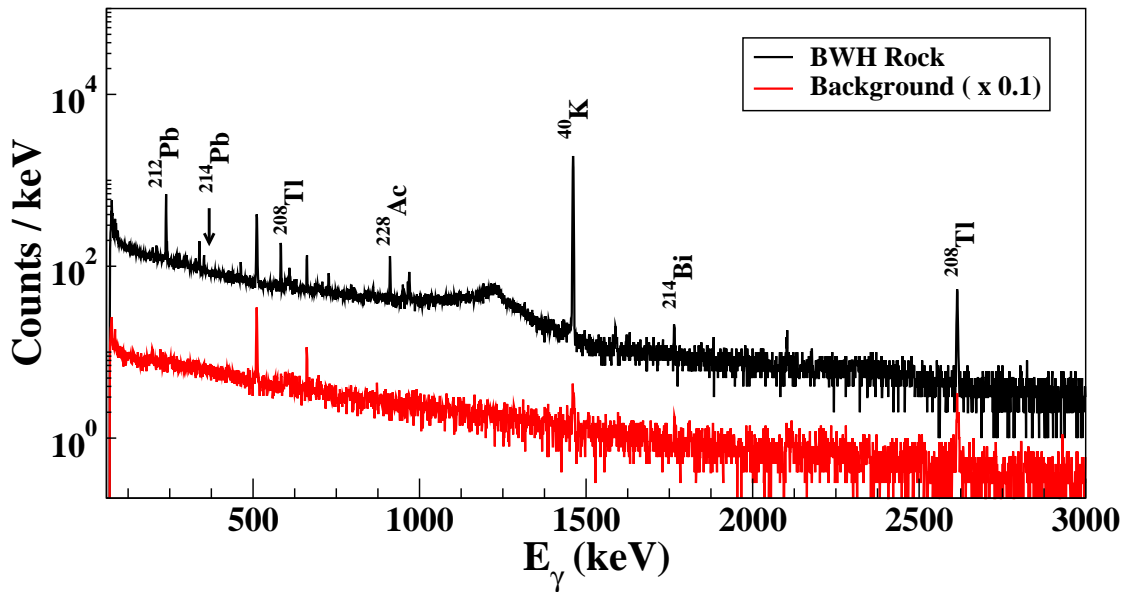


Figure 3.15: A gamma ray spectrum (black line) of the rock sample from the INO site (from Bodi West Hills) in the TiLES in a close geometry (only with Pb shield, $T_{data} = 1$ d). The scaled ambient background (red line) without the sample is also shown for comparison.

visible above the background level are listed in Table 3.10.

Table 3.10: Estimated radio-impurity concentrations (N_x) in the BWH rock sample from the INO site with 10 cm Pb shield.

Element	N_x (mBq/g)	Element	N_x (mBq/g)
^{212}Pb	11.1(4)	^{40}K	1050(16)
^{214}Pb	1.7(4)	^{208}Tl	1.8(8)
^{228}Ac	10.3(7)	^{214}Bi	7(1)

3.5.3 Sn Samples

Generally, large detector masses (~ 100 kg) are required for DBD studies. In case of Sn, the natural abundance of ^{124}Sn (isotope of interest) is 5.8% and its enrichment (to levels of 50-90%) on a large scale is a challenging task. Hence, in the initial stages of development of TIN.TIN detector, a $^{\text{nat}}\text{Sn}$ bolometer will be employed. Therefore, background from other stable natural Tin isotopes also needs to be investigated. With this motivation, the $^{\text{nat}}\text{Sn}$ (7N purity, mass ~ 630 mg), ^{124}Sn (97.2%, mass ~ 60 mg), ^{122}Sn (93.6%, mass ~ 100 mg) samples were counted in the TiLES with 10 cm Pb shield. The gamma ray spectrum of the ^{124}Sn sample in the TiLES is shown in Figure 3.16. Both the ^{122}Sn and ^{124}Sn samples (procured from Isoflex) showed high level of 661.7 keV gamma activity from ^{137}Cs . While ^{122}Sn has 3365(99) mBq/g of ^{137}Cs activity, ^{124}Sn showed 1739(47) mBq/g activity. The ^{124}Sn sample showed an additional unidentified gamma ray at 1064.6(2) keV at the rate of 12(4) counts/day. The gamma ray spectra of

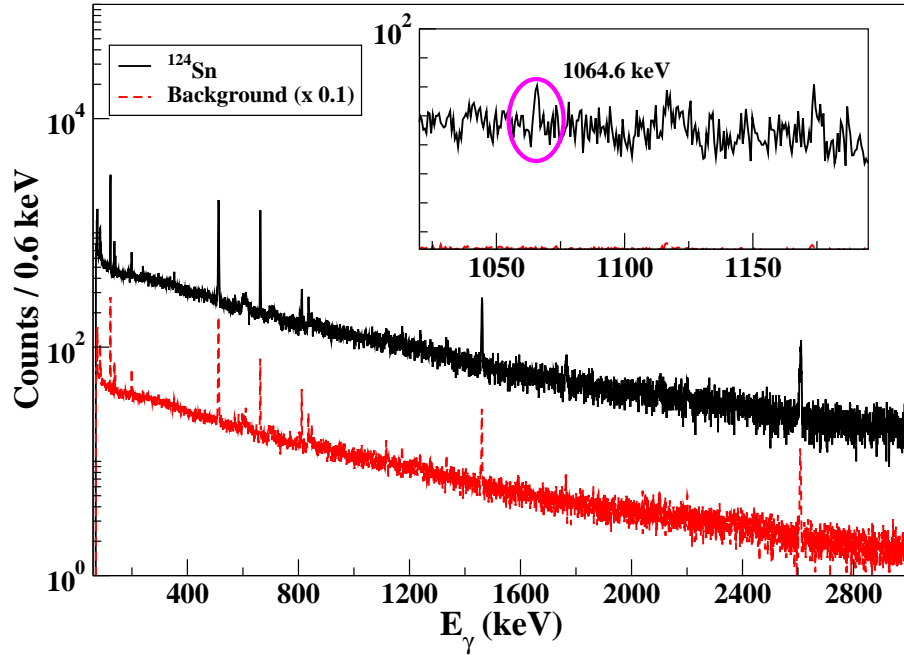


Figure 3.16: A gamma ray spectrum (black bold line) of the ^{124}Sn sample in the TiLES counted in a close geometry (only with 10 cm Pb shield, $T_{data} = 8.5$ d). The observed additional 1064.6(2) keV γ -ray is shown in the inset. The scaled ambient background (red dashed line) is also shown for comparison.

the $^{\text{nat}}\text{Sn}$ (Alfa Aesar) is shown in Figure 3.17 and the gamma rays detected above the ambient background level are listed in Table 3.11. The $^{\text{nat}}\text{Sn}$ sample also showed a gamma ray at 1271.9 keV originating from $^{112}\text{Sn}(n, \gamma)$ reaction. As mentioned earlier, the observed low energy gamma rays in the Sn samples can affect background in the ROI due to coincidence summing and pile up effects.

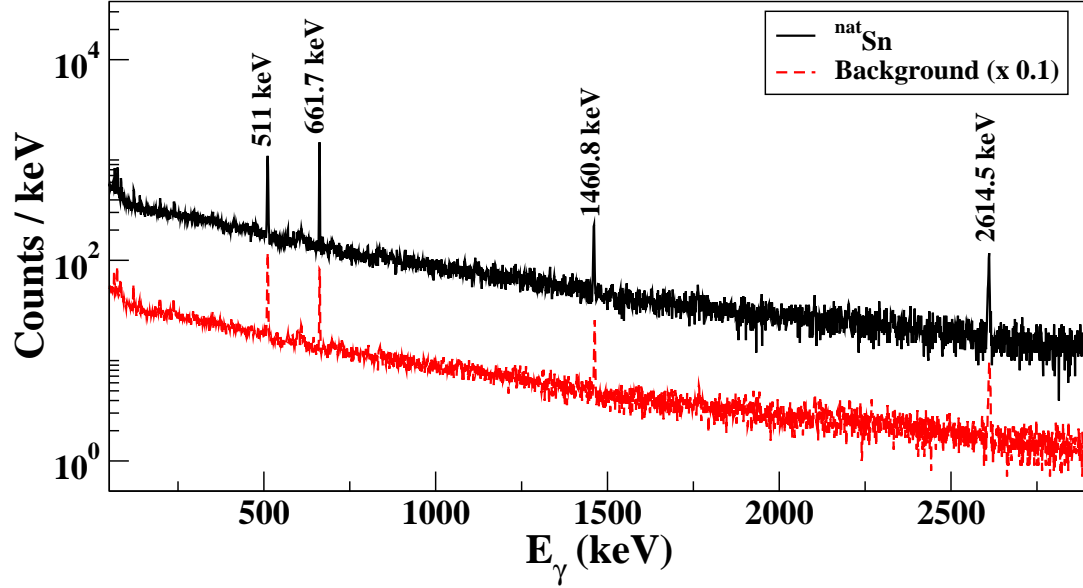


Figure 3.17: A gamma ray spectrum of the ^{nat}Sn sample (black bold line) in the TiLES counted in a close geometry (only with 10 cm Pb shield, $T_{data} = 4$ d). The scaled ambient background (red dashed line) is also shown for comparison.

Table 3.11: Gamma rays observed in the ^{nat}Sn sample with 10 cm Pb shield.

Energy (keV)	Radio-isotopes/ Reaction Channels	Observed Activity	
		(counts/day)	(mBq/g)
661.6	^{137}Cs	251(20)	100(8)
511*	Annihilation	23(1)	6.4(3)
1271.9*	$^{112}\text{Sn}(n, \gamma)$	53(9)	29(5)
1460.8	^{40}K	29(2)	168(12)
2614.5	^{208}Tl	30(3)	30(3)

* The branching fractions have been taken as 1.

3.5.4 Qualification of TIN.TIN Components

Many other components of TIN.TIN were investigated in the TiLES with 5 cm Cu + 10 cm Pb shield. For low temperature (mK) thermometry in

TIN.TIN, development of NTD Ge sensors is underway [71]. This involves the thermal neutron irradiation of Ge wafers. Spectroscopic studies of the NTD Ge samples, irradiated at Dhruva Reactor (BARC, Mumbai), were done in the TiLES to estimate a cooldown period for the radio-impurity levels to reduce to ≤ 1 mBq/g [96]. Commercial NTD Ge sensor (AdSem, Inc., mass ~ 2.4 mg) was also counted for comparison and was found to have high levels of ^{65}Zn ($T_{1/2} = 243.6$ d) 7566(523) mBq/g (see Figure 3.18). Silver paste is generally used in low temperature applications as an adhe-

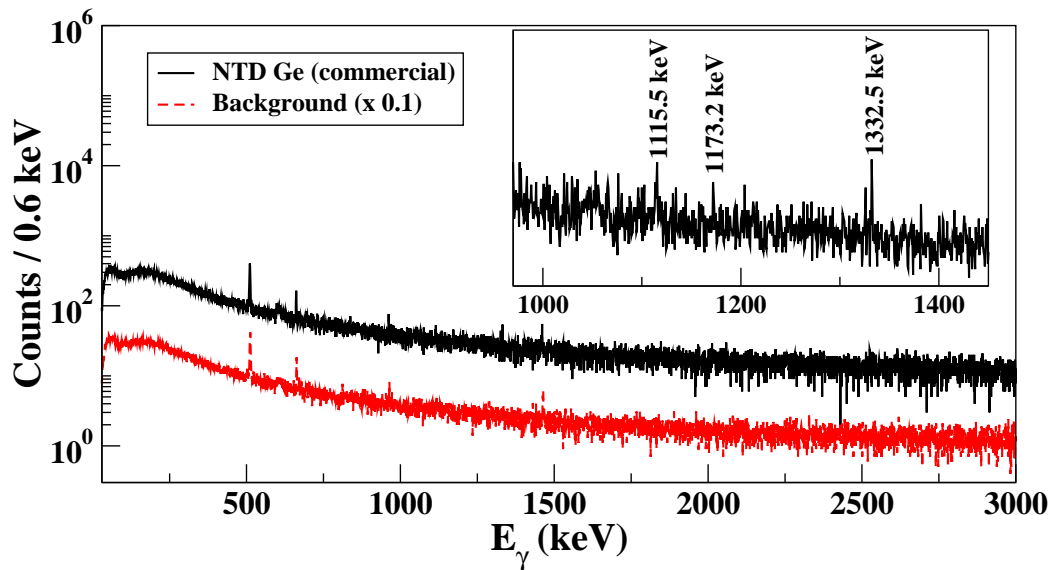


Figure 3.18: A gamma ray spectrum (black bold line) of the commercial NTD Ge sensor in the TiLES counted in a close geometry (with Cu + Pb shield, $T_{data} = 3$ d). An expanded view of the γ -rays in the range of 950–1500 keV is shown in the inset.

sive for making electrical contacts, e.g. to attach NbTi wires to the two ends of Carbon sensor [97]. Hence, radio-purity of the Silver paste was

checked by counting a small sample (mass ~ 30 g) in the TiLES and no radio-impurities were observed at the measurement sensitivity. Torlon and Teflon samples, which can be used in TIN.TIN as support structures, were also counted in the TiLES and did not show any measurable activity. All the virgin samples, used for neutron activation technique (discussed in next chapter) and Ge wafers prior to thermal neutron irradiation, were qualified in the TiLES. In addition, ^{nat}Zr foils were counted in the TiLES for estimating the sensitivity to measurement of DBD to excited state in ^{94}Zr , which will be discussed in chapter 6.

3.6 Summary

A low background setup TiLES comprising HPGe detector, surrounded by Cu inner shield, Pb outer shield and active veto system using plastic scintillators has been installed at TIFR. The OFHC Cu (Leico Industries, USA) is selected for an inner shield based on the radio-purity measurements in the TiLES. The digital DAQ based on a commercial CAEN digitiser has been set up for the TiLES. The CADFLAP program is developed to generate the anti-coincidence spectra between the HPGe detector and the plastic scintillators. The setup has been extensively used for qualification and selection of radio-pure materials to be used in the prototype bolometer R&D as well as for background studies. The BWH rock sample from INO cavern

was found to have considerably high level of ^{40}K (1050(16) mBq/g). The enriched Sn samples showed high levels of 661.7 keV γ -ray activity while the $^{\text{nat}}\text{Sn}$ (7N purity) samples has higher radioactivity of ^{40}K . In addition, gamma rays from Tin isotopes other than ^{124}Sn were observed in the $^{\text{nat}}\text{Sn}$ sample. Many gamma rays originating from neutron interactions were observed in the ETP Cu sample, emphasizing that an additional Pb shield will be essential around the Tin detector array inside the cryostat.

Chapter 4

Study of Neutron-induced Background and its Effect on $0\nu\beta\beta$ Decay in ^{124}Sn

4.1 Introduction

Of the different sources of background, namely, α, β, γ and neutrons, background arising from neutrons is most difficult to suppress and hence crucial to understand. In fact, neutrons are reported to be the limiting source of background for dark matter search experiments since they can produce nuclear recoils via elastic scattering off target nuclei resulting in a signal similar to that of WIMPs (Weakly Interacting Massive Particles) [98–100]. As discussed in Chapter 1, neutrons are produced in the spontaneous fission of $^{\text{nat}}\text{U}$ (mainly ^{238}U), Th present in the rocks and the surrounding materials. In addition, alpha particles produced from decay of intermediate nuclei

in the natural decay chains can react with light nuclei in the rocks to produce neutrons via (α, n) reactions [56]. Very high energy neutrons ($E_n \sim \text{GeV}$) are produced by muon-induced interactions in the rocks and materials surrounding the detector. It has been reported that in an underground laboratory, the low energy neutron flux ($E_n < 10 \text{ MeV}$) from natural radioactivity is about two to three orders of magnitude higher than that from the muon-induced reactions [56, 98, 101, 102]. Although the high energy neutrons are more penetrating, the average neutron energy reduces from 100 – 200 MeV to $\sim 45 \text{ MeV}$ [103] as they propagate through layers of shield materials. Thus, it is important to understand the background arising from low energy neutrons. With low energy neutrons, the inelastic scattering of neutrons ($n, n'\gamma$) and neutron-capture (n, γ) with the source/detector and the surrounding materials are main sources of gamma background. Moreover, these neutrons after thermalisation in the shield can produce significant background by radiative capture reactions in the detector/source assembly. In addition, any impurities in these materials could be potential sources of neutron-induced background. The reaction products formed upon neutron activation can have half-lives ranging from $\sim \text{min}$ to $\sim \text{years}$. The short-lived activities can be avoided by storing the material for prolonged periods in underground locations but the long-lived activities are highly undesirable.

This chapter presents measurements of the neutron-induced gamma background ($E_n < 20$ MeV) in TIN.TIN detector components. The aim of the neutron activation study ($E_n < 20$ MeV) is two fold – the selection of materials suitable for use in and around the cryogenic bolometer and the evaluation of its effect on the gamma background level in the ROI near $Q_{\beta\beta}(^{124}\text{Sn})$. The thermal neutron-induced background in $^{\text{nat}}\text{Sn}$ is also discussed.

4.2 Experimental Details

The Sn bolometer will be mounted in a specially designed low background cryostat. The neutron-induced gamma background from the cryostat housing can be significantly reduced by mounting low activity Pb shield inside the cryostat (similar to CUORE [104]). Hence, only the neutron activation of materials in the close vicinity of the detectors elements is of prime importance. For neutron-induced background study the materials chosen were: ETP $^{\text{nat}}\text{Cu}$ used inside the cryostat, Torlon 4203, Torlon 4301 and Teflon – cryogenic materials for detector holders, $^{\text{nat}}\text{Pb}$ – the common shielding material, $^{\text{nat}}\text{Sn}$ (7N purity) and 97.2% enriched ^{124}Sn . Torlon 4203, 4301 and Teflon samples used were of standard commercial grade. Elemental concentrations of Torlon and Teflon were obtained using Time of Flight Secondary Ion Mass Spectrometry (TOF-SIMS). Since all the materials contain high percentage of ^{19}F , Secondary Ion Mass Spectra

were obtained in both positive and negative ion modes to ascertain the total fluorine concentration. Final elemental concentrations were obtained after suitable correction with weighted relative sensitivity factors (RSF) for individual element [105] and are given in Table 4.1. Besides C, F and O, the major element found in Torlon 4203 is Ti (contains TiO₂ [106]) while Fe was found in Torlon 4301, which could be undesirable for low temperature applications. The samples also showed additional trace elements like Si, S, Cl and Mn but only dominant components with concentration > 0.1% are listed in Table 4.1.

Table 4.1: Elemental distribution of Torlon 4203, Torlon 4301 and Teflon obtained with SIMS.

Element	Torlon 4203 (%)	Torlon 4301 (%)	Teflon (%)
¹² C	28	27	24.4
¹⁶ O	1.2	1.3	0.9
¹⁹ F	66.2	67	72.3
²³ Na	0.1	0.2	0.2
^{24,25,26} Mg	0.2	0.3	0.3
²⁷ Al	0.2	0.2	0.2
³¹ P	0.2	0.2	0.2
^{39,40,41} K	0.2	0.2	0.2
⁴⁰ Ca	0.1	0.5	0.1
^{46,47,48,49,50} Ti	2.1	0.7	0.2
^{50,52,53,54} Cr	0.3	0.1	0.1
^{54,56,57,58} Fe	0.5	1.1	0.1
^{58,60,61,62} Ni	0.1	0.5	0.1
^{63,65} Cu	0.2	0.3	0.3

The neutron activation was performed using proton beam on Be and Li production targets in the neutron irradiation setup at the Pelletron Linac Facility, Mumbai [107]. Figure 4.1 shows a schematic diagram of the neutron irradiation set up showing the production target and sample mount.

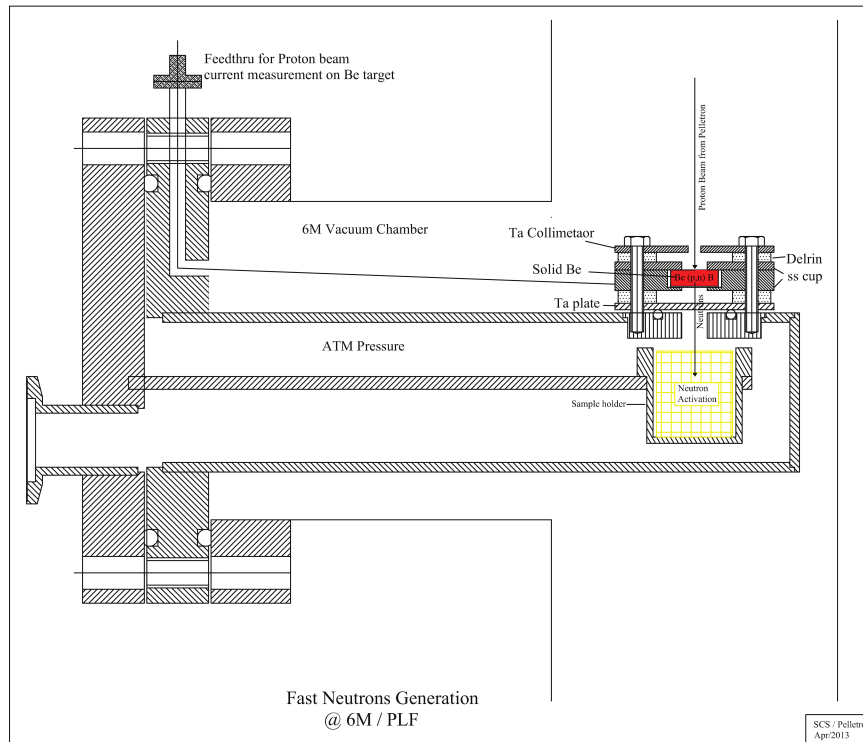


Figure 4.1: A schematic diagram of the neutron irradiation set up showing the production target (red box) and sample mount (yellow grid) [107].

Irradiation targets were mounted in a forward direction with respect to the proton beam, close to the production target but outside the vacuum chamber. This facilitated the change of irradiation targets without breaking the accelerator vacuum. The setup is located in a well shielded area above the analyzing magnet of the Pelletron, which permits the use of high proton beam current ~ 120 nA on the production target. In the present study, proton beams of energy $E_p = 10\text{-}20$ MeV on a Be target (5 mm thick) were used to obtain neutrons of a broad energy range with reaction ${}^9\text{Be}(p,n){}^9\text{B}$ ($Q = -1850$ keV) [108]. Beam energies were chosen to cover the energy range of neutron spectra originating from fission and (α, n) reactions in the rocks [56]. The energy dependence of the cross-sections of the possible reaction channels in different targets was also taken into consideration. In addition, nearly mono-energetic neutrons were produced with the ${}^7\text{Li}(p,n){}^7\text{Be}$ ($Q = -1644$ keV) reaction by bombarding a 0.15 mm thick natural Lithium target (wrapped in a ~ 2 μ thick Ta foil) with proton beam of energy 12 MeV. Contribution from the ${}^6\text{Li}$ (natural abundance 7.59%) in the natural lithium target is expected to be negligible. At $E_p = 12$ MeV, due to the contributions from the excited states of ${}^7\text{Be}$, quasi-monoenergetic neutrons are produced [109, 110]. The flux obtained in case of the Li target was smaller than that in the case of Be by a factor of ~ 10 . However, the better definition of neutron energy was useful for identification of some of

the reaction channels. It should be mentioned that neutron flux could not be measured accurately in the setup and hence ^{nat}Fe target ($\sim 5 - 6 \text{ mg/cm}^2$) was used to estimate neutron flux with the $^{56}\text{Fe}(n,p)^{56}\text{Mn}$ reaction. Multiple irradiation targets (upto five) were stacked in a 3 cm long target holder (Aluminum or Teflon) using Teflon spacers for an efficient utilization of beam time. In this geometry, the solid angles subtended by the neutron beam at the first and last target were $\sim 0.25 \text{ sr}$ and $\sim 0.04 \text{ sr}$, respectively. Thickness of irradiated targets varied from 1.8 mg/cm^2 to 0.29 g/cm^2 . Both short (2 – 3 h) as well as long (10 – 35 h) duration irradiation were carried out to look for short-lived and long-lived products. In case of long irradiation experiments, the access to target area was restricted due to the radiation safety limits and targets could be taken out for measurements only after sufficient cooling time ($\sim 20 \text{ min}$ to $\sim 1 \text{ h}$). Hence, some of the short-lived activities could not be observed.

The irradiated targets were counted offline for the detection of characteristic γ -rays of reaction products resulting from neutron activation. The TiLES (with Cu + Pb shield) was used for these spectroscopic studies. In addition, two HPGe detectors of R.E. $\sim 30\%$ (D1 and D2) shielded with 5 cm thick normal Pb rings were used (see Figure 4.2). The detectors D1 and D2 were mostly used for identification of gamma-rays and half-life measurements. Targets were mounted in a close geometry in these counting



Figure 4.2: A picture of the HPGe detectors D1 and D2 with 5 cm normal Pb shield.

setups to search for low levels of activity and coincidence summing effects had to be taken into account. Data were recorded with the CAEN N6724 digitizer and analyzed using LAMPS [84]. It should be mentioned that all targets were studied in the TiLES prior to irradiation and did not show any radioactivity above the background level.

4.2.1 Estimation of Neutron Flux

As mentioned earlier, the neutron flux is estimated from the yield of 846.7 keV γ -ray, produced via $^{56}\text{Fe}(n,p)^{56}\text{Mn}$ reaction. Since the neutron spectra produced from the $^9\text{Be}(p,n)^9\text{B}$ reaction is continuous, energy integrated neutron flux has been estimated in the energy range of $E_n \sim 100$ keV to E_{max} , where $E_{max} = E_p - Q_{th}$ with $Q_{th} = 2057$ keV. The number of Mn

atoms (N_{Mn}) produced by irradiation of a Fe target with a constant neutron flux ϕ_n ($n\text{ cm}^{-2}\text{ s}^{-1}$) for time t_{irr} is given by,

$$N_{Mn} = \frac{N_{Fe} (1 - e^{-\lambda t_{irr}}) \sum_{E_n} \sigma_c(E_n) \phi_n(E_n) dE_n}{\lambda} \quad (4.1)$$

where N_{Fe} is number of Fe target atoms, λ is the decay constant of ^{56}Mn and $\sigma_c(E_n)$ is the (n, p) cross-section of $^{56}\text{Fe}(n, p)^{56}\text{Mn}$ reaction at the neutron energy E_n . The factor $((1 - e^{-\lambda t_{irr}})/\lambda)$ arises from decay during irradiation. The N_{Mn} can be obtained from the measured photo peak area (N_γ) of 846.7 keV γ -ray as,

$$N_{Mn} = \frac{N_\gamma}{e^{-\lambda t_c} (1 - e^{-\lambda t}) I_\gamma \varepsilon_\gamma} \quad (4.2)$$

where t_c is the time elapsed between the end of neutron irradiation and start of the counting (cool-down time), t is the counting period, I_γ is the branching ratio and ε_γ is the photo peak detection efficiency of E_γ (846.7 keV) for a finite size source in close geometry, computed using GEMS program [95]. Since the distribution of neutrons produced from the $^9\text{Be}(p, n)^9\text{B}$ reaction is continuous, energy integrated neutron flux can be estimated as,

$$\langle \phi_n \rangle = \frac{\sum_{E_n} \sigma_c(E_n) \phi_n(E_n) dE_n}{\sum_{E_n} \sigma_c(E_n) dE_n} \quad (4.3)$$

The numerator in Eq. 4.3 is extracted from Eq. 4.1 while the denominator is obtained using ENDF/B-VII library [111]. In case of Li target, since the emitted neutrons are nearly monoenergetic, the measured value of neutron capture cross section in the same setup, $\sigma_c = 65.88$ (4.54) barn, at an average neutron energy $E_n = 9.85$ MeV corresponding to $E_p = 12$ MeV is used [112]. Table 4.2 gives the extracted neutron flux at a distance $d \sim 5$ cm from the production target (Be/Li) for different proton energies together with maximum energy of the neutrons E_{max} , average energy of the neutrons $\langle E_n \rangle$ and the average proton beam current $\langle I \rangle$. The $\langle E_n \rangle$ for $p+{}^9\text{Be}$ reaction is calculated as,

$$\langle E_n \rangle = \frac{\sum_{i=0}^3 \sum_{E_n} \sigma_{(p,n_i)}(E_n) E_n dE_n}{\sum_{i=0}^3 \sum_{E_n} \sigma_{(p,n_i)}(E_n) dE_n} \quad (4.4)$$

where the summation runs over E_n from ~ 100 keV to E_{max} and $\sigma_{(p,n_i)}(E_n)$ corresponds to ${}^9\text{Be}(p, n_i){}^9\text{B}$ cross-section at E_n for the i th channel of neutron production [111]. Only (p, n_0) , (p, n_1) , (p, n_2) and (p, n_3) channels are considered and others with total cross-sections $< 6\%$ of (p, n_0) are neglected.

Table 4.2: Estimated energy integrated neutron flux from $^{56}\text{Fe}(n,p)^{56}\text{Mn}$ reaction for 12 and 20 MeV proton energies (at $d \sim 5$ cm).

Production Target	E_p (MeV)	E_{max} (MeV)	$\langle E_n \rangle$ (MeV)	ϕ_n ($n\text{ cm}^{-2}\text{ s}^{-1}$)	$\langle I \rangle$ (nA)
^9Be	12	9.9	3.9	$2.3(0.2) \times 10^5$	133
	20	17.9	5.6	$9.9(0.7) \times 10^5$	148
$^{\text{nat}}\text{Li}$ [113]	12	10.1	9.85	$1.3(0.2) \times 10^5$	112

The uncertainty in the neutron flux includes the error in ε_γ , statistical and fitting errors in the photo peak area of 846.7 keV γ -ray (N_γ) and error in the coincidence summing correction factor for ^{56}Mn . It should be noted that the neutron flux at $E_p = 10$ MeV could not be measured since the activity of 846.7 keV γ -ray was not observed due to relatively lower yield.

4.3 Data Analysis and Results

Table 4.3 lists the details of the products formed in different samples together with their half-lives and the expected most intense γ -rays. The last two columns of the Table 4.3 give the minimum neutron energy E_n at which the cross-section for the respective neutron-induced reaction channel is $\geq \mu\text{b}$. In most of the cases, the half-lives ($T_{1/2}$) of the reaction products were measured and were found to agree within 20% of the reference values [111]. As the expected energy resolution of the Tin bolometer is 0.2–0.5% (full width at half maximum) at $Q_{\beta\beta}$, the ROI for background estimation is taken

as 2292.6 ± 25 keV (i.e., $Q_{\beta\beta} \pm 5\sigma$). The gamma-rays with energies within this ROI as well as with $E \geq Q_{\beta\beta}$ are potential sources of background and are highlighted in bold text in Table 4.3.

Table 4.3: Neutron-induced reaction products, $T_{1/2}$ and expected γ -rays in the irradiated samples. The minimum neutron energy E_n at which corresponding σ is $\geq \mu\text{b}$ is also listed [111].

Sample	Reaction channel	$T_{1/2}$	E_γ (keV)	E_n (MeV)	σ (barn)
Torlon 4203	${}^{\text{nat}}\text{Ti}(n, X){}^{47}\text{Sc}$	3.3492 d	159.4		
	${}^{\text{nat}}\text{Ti}(n, X){}^{48}\text{Sc}$	43.67 h	175.4, 983.5, 1037.5, 1312.1		
	${}^{\text{nat}}\text{Ti}(n, X){}^{46}\text{Sc}$	83.79 d	889.3, 1120.5		
	${}^{27}\text{Al}(n, \alpha){}^{24}\text{Na}$	14.997 h	1368.6, 2754.0	4.6	1.4×10^{-6}
	${}^{27}\text{Al}(n, p){}^{27}\text{Mg}$	9.458 min	843.8, 1014.5	2.5	1.9×10^{-5}
Torlon 4301	${}^{56}\text{Fe}(n, p){}^{56}\text{Mn}$	2.5789 h	846.8, 1810.7, 2113.1	4	6.0×10^{-6}
	${}^{27}\text{Al}(n, \alpha){}^{24}\text{Na}$	14.997 h	1368.6, 2754.0	4.6	1.4×10^{-6}
Teflon	${}^{19}\text{F}(n, 2n){}^{18}\text{F}$	109.77 min	511	11.5	1.5×10^{-3}
${}^{\text{nat}}\text{Pb}$	${}^{204}\text{Pb}(n, 2n){}^{203}\text{Pb}$	51.92 h	279.2, 401.3 680.5	8.5	2.1×10^{-3}
	${}^{204}\text{Pb}(n, n'){}^{204\text{m}}\text{Pb}$	66.93 min	374.8, 899.2, 911.7, 1274	1.0	2.4×10^{-1}
	${}^{121}\text{Sb}(n, \gamma){}^{122}\text{Sb}$	2.7238 d	564.2, 692.7,	0.1	2.1×10^{-1}
	${}^{123}\text{Sb}(n, \gamma){}^{124}\text{Sb}$	60.20 d	602.7, 1690.9 2090.9, 2182.6 2294.0	0.1	1.9×10^{-1}
${}^{\text{nat}}\text{Cu}$	${}^{63}\text{Cu}(n, \gamma){}^{64}\text{Cu}$	12.701 h	511, 1345.8	0.055	2.5×10^{-2}
	${}^{63}\text{Cu}(n, \alpha){}^{60}\text{Co}$	1925.28 d	1173.2, 1332.5	2.5	1.1×10^{-2}
	${}^{65}\text{Cu}(n, \gamma){}^{66}\text{Cu}$	5.120 min	1039.2	0.06	1.1×10^{-2}
	${}^{65}\text{Cu}(n, \alpha){}^{62\text{m}}\text{Co}$	13.91 min	1163.5, 1172.9, 2003.7, 2104.9, 2301.9, 2882.3	5	3.9×10^{-6}
	${}^{65}\text{Cu}(n, p){}^{65}\text{Ni}$ ${}^{64}\text{Ni}(n, \gamma){}^{65}\text{Ni}$	2.5175 h	1115.5, 1481.8, 1623.4, 1724.9	2.5 0.553	1.0×10^{-6} 6.5×10^{-3}

Table 4.3 continued...

Sample	Reaction channel	$T_{1/2}$	E_γ (keV)	E_n (MeV)	σ (barn)
nat, ¹²⁴ Sn	¹¹² Sn(n, np) ¹¹¹ In	2.8047 d	171.3, 245.4	12	4.9×10^{-6}
	¹¹⁶ Sn(n, np) ^{115m} In	4.486 h	336.2	14.5	7.6×10^{-5}
	¹¹⁵ Sn(n, p) ^{115m} In			5	1.9×10^{-4}
	¹¹⁵ In(n, n') ^{115m} In			0.5	6.4×10^{-3}
	¹¹⁶ Sn(n, p) ^{116m} In	54.29 min	416.9, 818.7, 1097.3, 1293.6 1293.6, 2112.3	8	1.5×10^{-4}
	¹¹⁷ Sn(n, n') ^{117m} Sn	13.76 d	156.0, 158.6	0.2	2.9×10^{-1}
	¹¹⁶ Sn(n, γ) ^{117m} Sn			0.1	5.5×10^{-2}
	¹¹⁸ Sn(n, 2n) ^{117m} Sn			9.9	7.2×10^{-2}
¹²⁴ Sn(n, 2n) ^{123m} Sn	40.06 min	160.3	9	1.6×10^{-1}	
¹²² Sn(n, γ) ^{123m} Sn			0.3	1.2×10^{-2}	
¹²⁴ Sn(n, 2n) ¹²³ Sn	129.2 d	1088.6	9	1.6×10^{-1}	
¹²² Sn(n, γ) ¹²³ Sn			0.3	1.2×10^{-2}	
¹²⁴ Sn(n, γ) ^{125m} Sn	9.52 min	331.9	0.315	6.8×10^{-3}	
¹²⁴ Sn(n, γ) ¹²⁵ Sn	9.64 d	822.5, 1067.1 1089.2			

It should be mentioned that many of these reaction products decay by β^- emission and if the $Q_\beta \geq Q_{\beta\beta}({}^{124}\text{Sn})$, electrons or bremsstrahlung resulting from these electrons can contribute to the background in ROI. In particular, the (n, γ) reaction on ¹²⁴Sn leads to ¹²⁵Sn which β^- decays with a Q_β (2357 keV) value close to the $Q_{\beta\beta}$ of ¹²⁴Sn. Due to short range of electrons, contribution to the background in the detector arising due to β -decays in the shield and support materials will be mainly from the surface events.

This together with β -decays within the detector will affect the background, which is not considered in the present work.

4.3.1 Neutron-induced Activity from Torlon and Teflon

Figure 4.3 shows the gamma ray spectra of the irradiated Torlon 4203, Torlon 4301 and Teflon samples at different times (t_c) after the neutron irradiation.

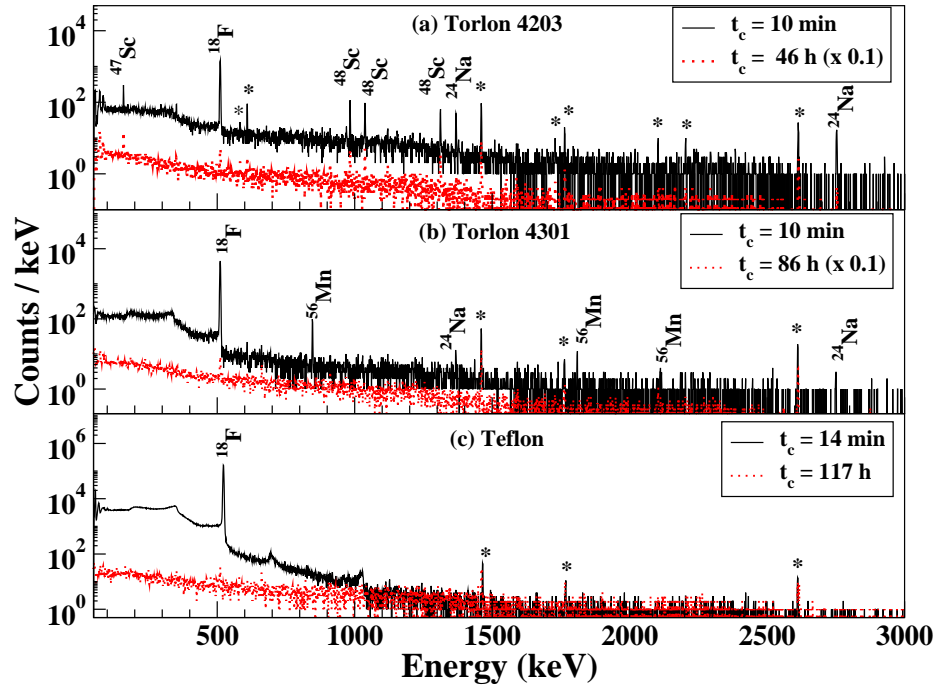


Figure 4.3: Gamma ray spectra of the neutron irradiated (a) Torlon 4203 with $E_p = 20$ MeV, $t_{irr} = 3$ h, $N_n \sim 1.31(9) \times 10^{10}$, (b) Torlon 4301 with $E_p = 20$ MeV, $t_{irr} = 3$ h, $N_n \sim 1.38(9) \times 10^{10}$ and (c) Teflon with $E_p = 20$ MeV, $t_{irr} = 2$ h, $N_n \sim 0.82(6) \times 10^{10}$ for different t_c – time elapsed since the end of irradiation. The spectrum shown in (a) is measured in the D2 setup while spectra in (b) and (c) are recorded in the D1 setup. In panels (a) and (b), spectra for larger t_c are scaled by 0.1 for better visualization. The γ -rays originating from room background are indicated with stars ($T_{data} = 1$ h for each spectrum).

Both Torlon 4203 and 4301 samples were exposed to similar neutron dose, while the neutron dose received by the Teflon sample was $\sim 40\%$ lower. It can be seen that the most dominant gamma-ray is 511 keV in all the three samples, but the Torlon and Teflon samples show different levels of activity and different impurities. The Teflon and Torlon samples contain fluorocarbon in different proportions, which is reflected in the intensity of the 511 keV γ -ray with Teflon having the maximum intensity. As mentioned earlier, the Torlon 4203 contains TiO_2 (Table 4.1) and many gamma-rays originating from $\text{Ti}(n,X)\text{Sc}$ reactions are clearly visible (see Table 4.3). Most of the Sc isotopes formed are short-lived and produce γ -rays with $E_\gamma < 1312$ keV. However, ^{46}Sc has a relatively long half-life, namely, $T_{1/2} = 83.79$ d. It may be mentioned that the Large Underground Xenon (LUX) dark matter experiment has observed background from ^{46}Sc , which was formed due to the cosmogenic activation of the LUX Titanium cryostat [114]. In case of the Torlon 4301, γ -rays resulting from $^{56}\text{Fe}(n,p)^{56}\text{Mn}$ reaction were observed (see Figure 4.3(b)). Both the Torlon samples have traces of Al, which gives rise to γ -ray of energy 2754.0 keV which is higher than $Q_{\beta\beta}(^{124}\text{Sn})$ with a $T_{1/2} = 14.99$ h and is highly undesirable. Figure 4.4 shows the decay curves for 511 keV γ -ray in the irradiated Torlon and Teflon samples. The background rate at 511 keV in the different detector systems has been taken into account. The origin of 511 keV from the $^{19}\text{F}(n,2n)^{18}\text{F}$

reaction is confirmed since the measured half-life agrees with that of ^{18}F within errors, namely, $T_{1/2}^{ref} = 109.77(5)$ min [111].

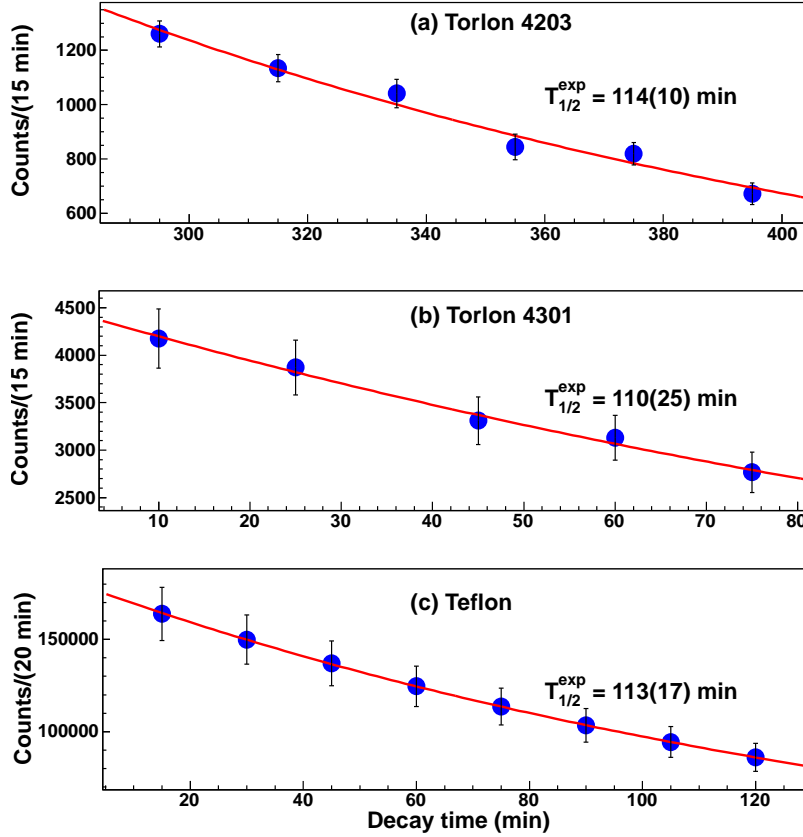


Figure 4.4: Decay curves for 511 keV γ -ray of ^{18}F formed in the irradiated (a) Torlon 4203 with $E_p = 20$ MeV and $t_{irr} = 10$ h, (b) Torlon 4301 with $E_p = 20$ MeV and $t_{irr} = 3$ h and (c) Teflon with $E_p = 20$ MeV and $t_{irr} = 2$ h.

Considering the threshold energy $E_n \sim 11.5$ MeV for $^{19}\text{F}(n, 2n)^{18}\text{F}$ reaction [111], this channel is not expected to be activated at lower neutron energies. The gamma ray spectra of irradiated samples at $E_p = 12$ MeV are

shown in Figure 4.5 for Teflon (in dotted red lines) and in Figure 4.6 for the Torlon samples. It can be clearly seen that the ^{18}F is not populated at $E_n \leq 9.9$ MeV ($E_p = 12$ MeV) and yield of 511 keV γ -ray is significantly reduced, whereas most of the reaction channels in Torlon are populated even at lower neutron energy (see Table 4.3). It may be mentioned that the observed peaks at 1022 keV and ~ 685.6 keV in the Teflon spectrum, originate from summing of two 511 keV γ -rays and from summing of 511 keV with backscattered gamma-rays, respectively. This is also seen in the $^{\text{nat}}\text{Cu}$ sample.

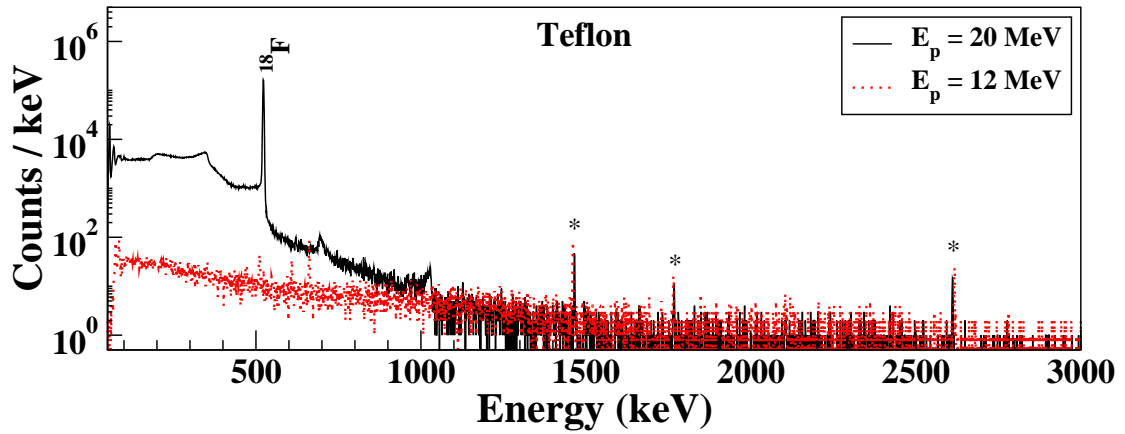


Figure 4.5: Gamma ray spectra of the neutron irradiated Teflon with $E_p = 20$ MeV, $t_{irr} = 2$ h and $N_n \sim 0.82(6) \times 10^{10}$ (shown by solid black lines) together with $E_p = 12$ MeV, $t_{irr} = 13$ h and $N_n \sim 1.27(9) \times 10^{10}$ (shown by dotted red lines). Both the spectra have been measured after similar cooling time (t_c) 14 min and 10 min, respectively, in the D1 setup ($T_{data} = 1$ h for each spectrum). Stars have same meaning as in Figure 4.3.

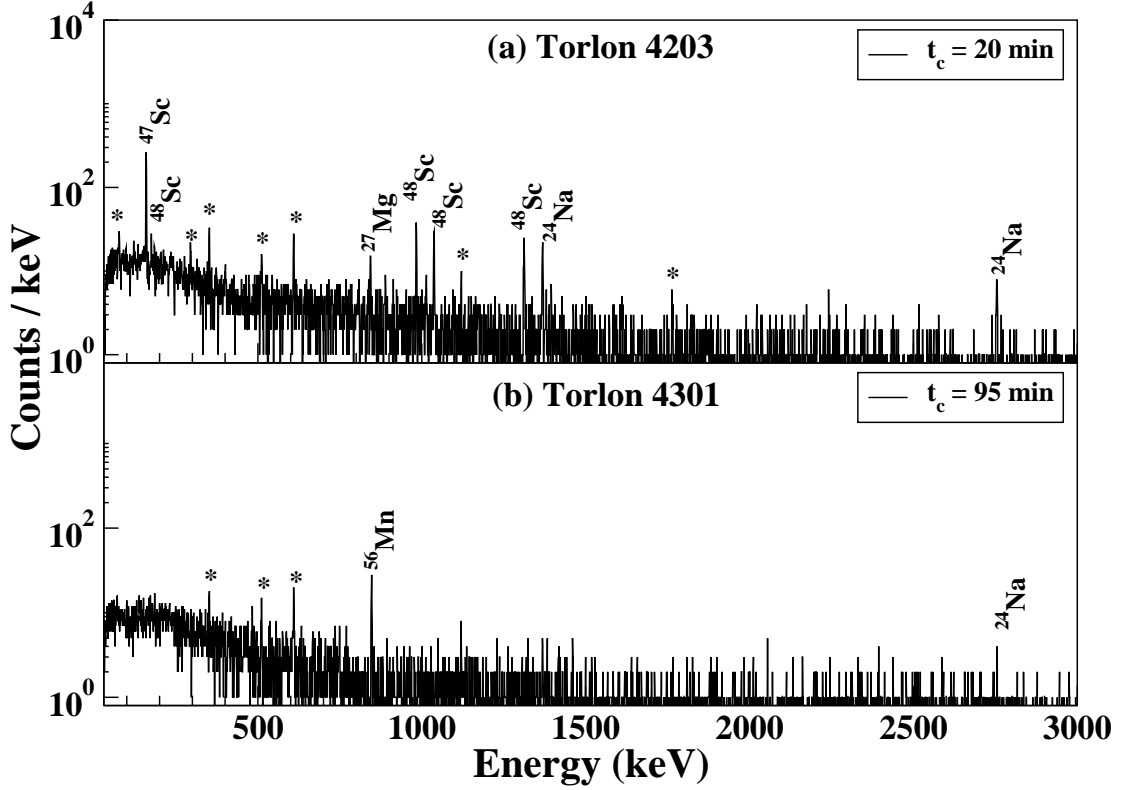


Figure 4.6: Gamma ray spectra of the neutron irradiated (a) Torlon 4203 ($N_n \sim 1.4(1) \times 10^{10}$) and (b) Torlon 4301 ($N_n \sim 1.3(1) \times 10^{10}$) with $E_p = 12$ MeV and $t_{irr} = 13$ h. Both the spectra are recorded in the TiLES ($T_{data} = 1$ h for each spectrum). Stars have same meaning as in Figure 4.3.

Even though the 511 keV γ -ray activity in Teflon is significantly larger (~ 15.5 (1.2) times) than that in Torlon 4301, there is no gamma background at energies higher than 511 keV in Teflon. Therefore from the neutron-induced gamma background consideration, Teflon seems to be a better candidate as compared to the Torlon for use in TIN.TIN detector.

4.3.2 Neutron-induced Activity from ^{nat}Pb and ^{nat}Cu

The Lead shield is generally closer to the detector assembly and the gamma rays produced by neutron-induced reactions in Lead can deteriorate the background levels. It has been previously reported in Ref. [103] that inelastic scattering of neutrons in Lead can be a significant source of background for DBD experiments. The gamma ray spectra of the irradiated ^{nat}Pb and ^{nat}Cu samples are shown in Figures 4.7 (a) and (b), respectively. Gamma-rays originating from decay of ^{203}Pb and ^{204m}Pb (see Table 4.3) are seen in the spectrum. In addition, Sb impurities are also found in the Lead sample. It should be noted that the decay of ^{124}Sb produces many gamma-rays $> Q_{\beta\beta}$ (^{124}Sn) but with small branching fractions: 2294.0 keV (0.0320%), 2323.5 keV (0.00243%), 2455.2 keV (0.0015 %), 2681.9 keV (0.00165%), 2693.6 keV (0.0030 %) and 2807.5 keV (0.00147%) [111]. In the present work, only 602.7 keV is observed in the gamma-ray spectrum above the detection limit of the TiLES. But $E_{\gamma} = 2294.0$ keV may be a crucial source of background in an underground laboratory with improved sensitivity.

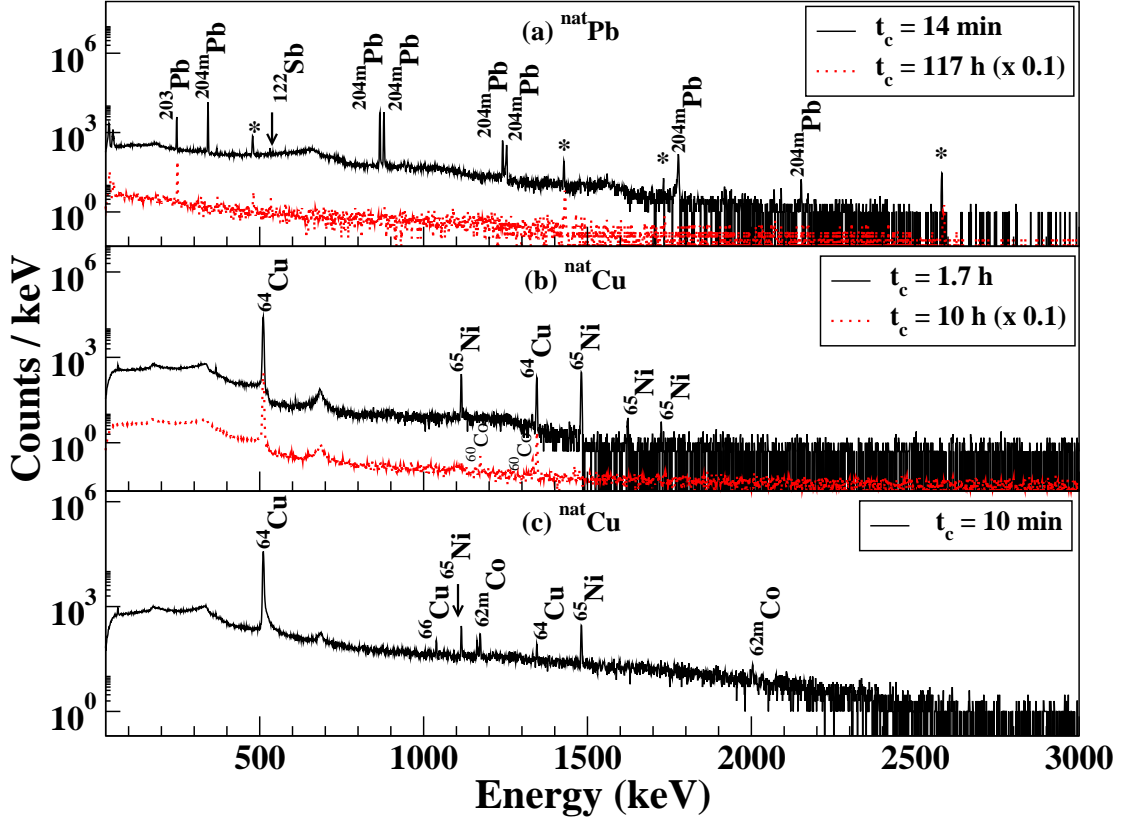


Figure 4.7: Gamma ray spectra of the neutron irradiated (a) $^{\text{nat}}\text{Pb}$ with $E_p = 20$ MeV, $t_{\text{irr}} = 2$ h and $N_n \sim 0.69(5) \times 10^{10}$ for different cooling time t_c , (b) $^{\text{nat}}\text{Cu}$ with $E_p = 20$ MeV, $t_{\text{irr}} = 10$ h, $N_n \sim 5.9(4) \times 10^{10}$ for different cooling time t_c and (c) $^{\text{nat}}\text{Cu}$ with $E_p = 20$ MeV, $t_{\text{irr}} = 2$ h and $N_n \sim 1.09(8) \times 10^{10}$. The spectrum shown in (a) is measured in the D2 setup while those in (b) and (c) in the TiLES ($T_{\text{data}} = 1$ h for each spectrum). In panels (a) and (b), spectra for larger t_c are scaled by 0.1 for better visualization. Stars have same meaning as in Figure 4.3.

In the gamma ray spectrum of $^{\text{nat}}\text{Cu}$ (see Figure 4.7(b)) short-lived activities ($T_{1/2} \sim \text{h}$) such as ^{64}Cu and ^{65}Ni are seen. The long-lived products like ^{60}Co ($T_{1/2} = 5.27$ y) are visible in the spectra after sufficient cooling time ~ 10 h, when the overall gamma background level due to the decay of the short-lived nuclei is reduced. Short-lived products ($T_{1/2} \sim \text{min}$) such

as ^{62m}Co and ^{66}Cu formed in the Copper sample are visible where spectra could be measured after shorter cooling time. Figure 4.8 shows the half life tracking of some of the products formed in $^{\text{nat}}\text{Pb}$ sample.

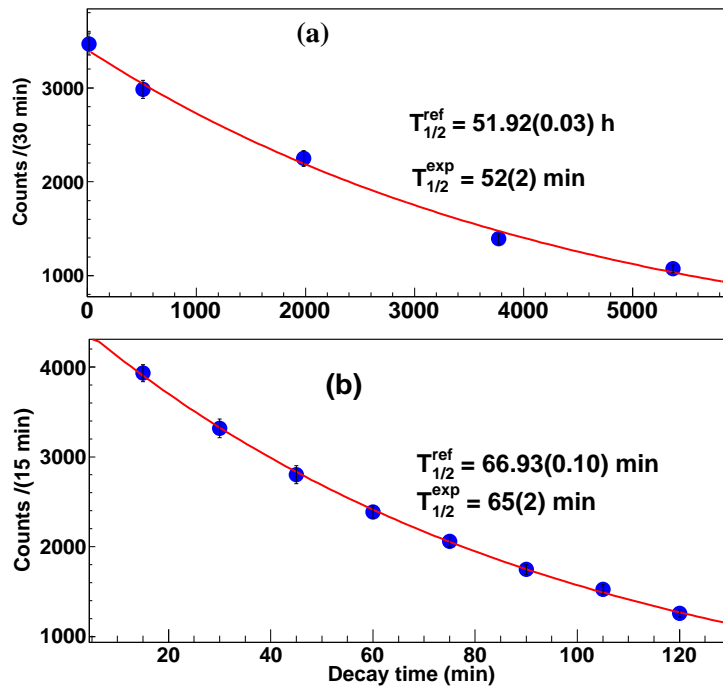


Figure 4.8: Decay curves for (a) 279 keV γ -ray of ^{203}Pb and (b) 899 keV γ -ray of ^{204m}Pb formed in the neutron irradiated $^{\text{nat}}\text{Pb}$ with $E_p = 20 \text{ MeV}$.

Figure 4.9(a) shows the decay curve of 511 keV γ -ray in $^{\text{nat}}\text{Pb}$ sample. A single exponential fit indicated $T_{1/2} \sim 41(4) \text{ min}$, while a two component fit resulted in $T_{1/2}^{t_1}$ and $T_{1/2}^{t_2}$ as 11(4) and 70(32) min, respectively but the origin of 511 keV in $^{\text{nat}}\text{Pb}$ was not identified. Whereas the decay curve in Figure 4.9(b) for $^{\text{nat}}\text{Cu}$ gives $T_{1/2} \sim 12.4(5) \text{ h}$, implying that the 511 keV γ -ray

results from the $^{63}\text{Cu}(n, \gamma)^{64}\text{Cu}$ reaction. It should be noted that no ^{18}F was observed in the $^{\text{nat}}\text{Pb}$ or $^{\text{nat}}\text{Cu}$ samples, confirming that the Teflon sample holder/spacers did not contribute to observed impurities in these samples.

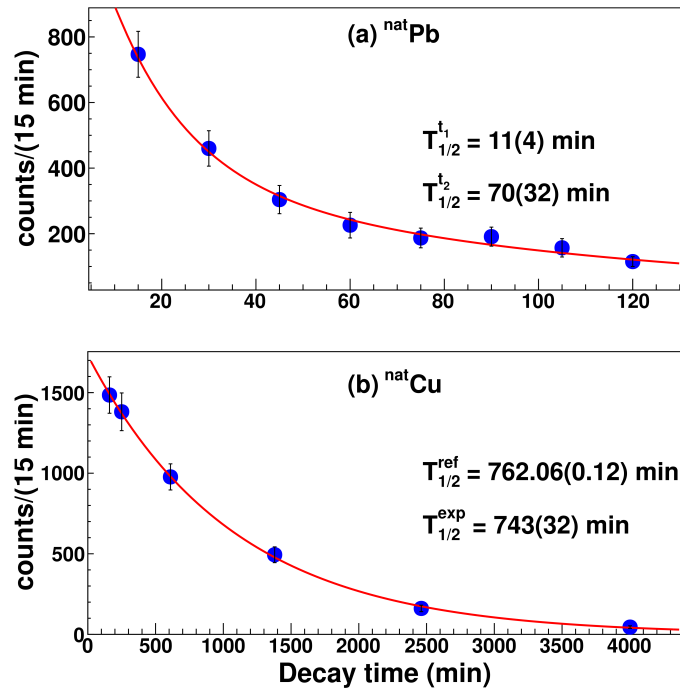


Figure 4.9: Decay curves for 511 keV γ -ray formed in the irradiated (a) $^{\text{nat}}\text{Pb}$ with $E_p = 20$ MeV and $t_{irr} = 2$ h, (b) $^{\text{nat}}\text{Cu}$ with $E_p = 20$ MeV and $t_{irr} = 2$ h.

Refs. [104, 115] have reported the formation of ^{60}Co in Copper due to cosmogenic activation. In addition, the $^{62\text{m}}\text{Co}$ decay produces several high energy γ -rays (see Figure 4.7(c)). Therefore for minimizing the Co activity, it is essential to store Copper in an underground location.

4.3.3 Neutron-induced Activity in ^{nat}Sn and ^{124}Sn

Figure 4.10(a) shows the gamma ray spectra of the neutron irradiated ($E_{max} = 17.9$ MeV) enriched ^{124}Sn (97.2%) sample. In addition to the gamma rays originating from neutron activation of ^{124}Sn , reaction products of other Sn isotopes, namely, ^{112}Sn , ^{115}Sn , ^{116}Sn , ^{117}Sn and ^{122}Sn , are also found in the enriched sample (see Table 4.3). Most of the isotopes formed are short-lived, the longest-lived being ^{123}Sn with a $T_{1/2} = 129.2$ d. The highest energy gamma ray $E_{\gamma} = 2112.3$ keV originates in the decay of ^{116m}In . Some of the observed reaction products can be produced by different Tin isotopes depending on the incident neutron energy and the relative cross-sections. For example, ^{123m}Sn can be formed either by $^{122}\text{Sn}(n, \gamma)^{123m}\text{Sn}$ or by $^{124}\text{Sn}(n, 2n)^{123m}\text{Sn}$ reaction. The contribution from ^{122}Sn was probed by low energy neutron irradiation ($E_{max} = 7.9$ MeV corresponding to $E_p = 10$ MeV) where the $^{124}\text{Sn}(n, 2n)^{123m}\text{Sn}$ reaction is unfavoured. The observation of significantly reduced (0.16%) but measurable activity of ^{123m}Sn ($E_{\gamma} = 160.3$ keV) at lower neutron energy clearly indicated the traces of ^{122}Sn in the enriched sample. Similarly, ^{115m}In ($E_{\gamma} = 336.2$ keV) can be produced from $^{115,116}\text{Sn}$ with high energy neutrons but at lower neutron energy only $^{115}\text{In}(n, n')^{115m}\text{In}$ (^{115}In natural abundance 95.7%) is the possible reaction channel. Thus, observation of 336.2 keV γ -ray with low energy

neutrons implies presence of trace impurity of ^{115}In in the enriched Tin target. In the observed spectra, γ -rays 1088.6 and 1089.2 keV originating from decay of ^{123}Sn ($T_{1/2} = 129.2$ d) and ^{125}Sn ($T_{1/2} = 9.64$ d), respectively, could not be separated. Measurements after $t_c \sim 10$ d showed that the relative yield

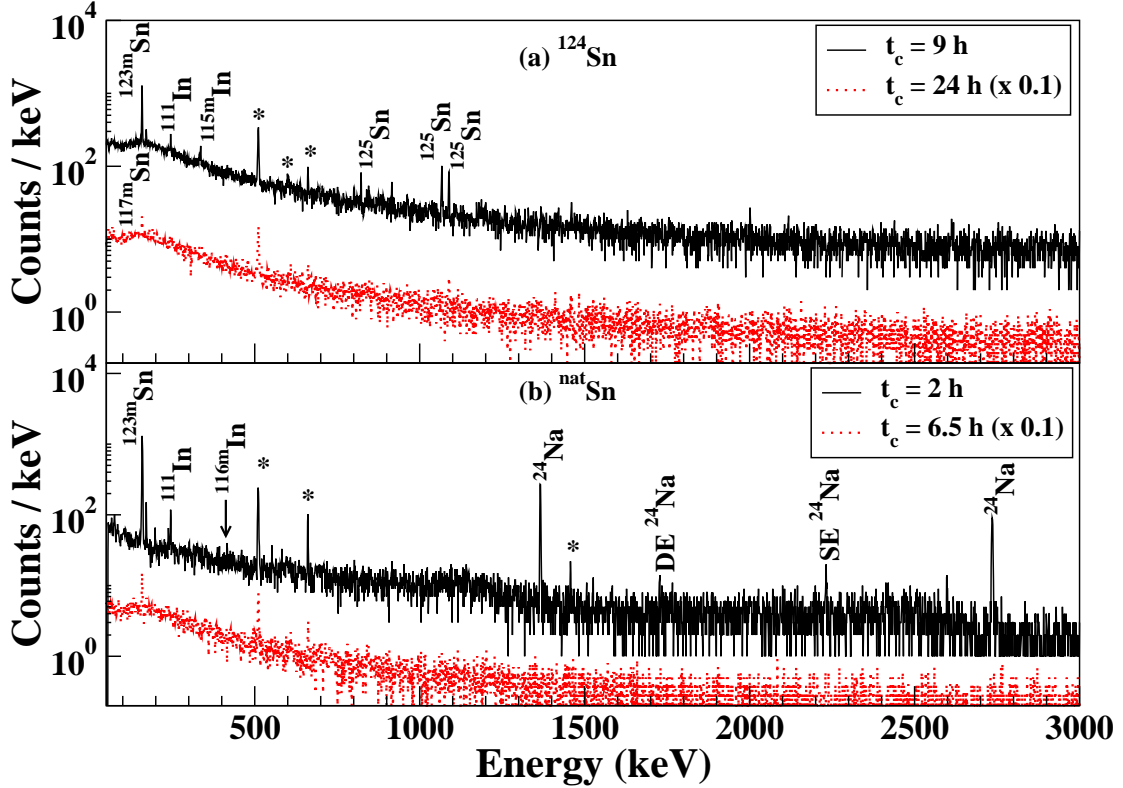


Figure 4.10: Gamma ray spectra of the neutron irradiated (a) ^{124}Sn with $E_p = 20$ MeV, $t_{irr} = 10$ h, $N_n \sim 4.1(3) \times 10^{10}$ (solid black lines) and with $E_p = 10$ MeV, $t_{irr} = 5$ h and $N_n \sim 0.44(4) \times 10^{10}$ (dotted red lines) ($T_{data} = 14$ h), (b) ^{nat}Sn with $E_p = 20$ MeV, $t_{irr} = 2$ h, $N_n \sim 1.9(1) \times 10^{10}$ (solid black lines) and with $E_p = 10$ MeV, $t_{irr} = 5$ h, $N_n \sim 0.51(4) \times 10^{10}$ (dotted red lines). All spectra are recorded in the TiLES and those corresponding to larger t_c have been scaled by 0.1 for better visualization ($T_{data} = 6$ h for each spectrum). Stars have same meaning as in Figure 4.3.

of $E_\gamma = 1089.2$ keV was higher than that for $E_\gamma = 1067$ keV confirming the

formation of ^{123}Sn . It should be noted that 331.9 keV and 822.5 keV γ -rays from $^{125\text{m}}\text{Sn}$ and ^{125}Sn , respectively, were also visible.

Figure 4.10(b) shows the gamma ray spectra of irradiated $^{\text{nat}}\text{Sn}$ sample with low energy neutrons, where the gamma rays from reaction products of ^{112}Sn , ^{116}Sn and ^{122}Sn are visible. The other stable isotopes of Sn upon neutron activation form either long-lived and/or stable reaction products and hence could not be observed. It should be noted that 336.2 keV γ -ray from $^{115\text{m}}\text{In}$ was not visible in the $^{\text{nat}}\text{Sn}$ (7N) sample at the same detection sensitivity as in case of ^{124}Sn . Gamma rays originating from decay of ^{24}Na were observed in the samples irradiated in an Al target holder, produced via $^{27}\text{Al}(n, \alpha)^{24}\text{Na}$ reaction (see Figure 4.10(b)). No additional impurities are seen in the $^{\text{nat}}\text{Sn}$ (7N) sample.

4.3.4 Effect of Neutron-induced Gamma Background for $0\nu\beta\beta$ Decay in ^{124}Sn

Neutron-induced gamma background at energies $E_\gamma \geq 2.1$ MeV is estimated for the measured neutron flux corresponding to $E_p = 20$ MeV. Activities of different reaction products in the $^{\text{nat}}\text{Cu}$, $^{\text{nat}}\text{Pb}$ and $^{124,\text{nat}}\text{Sn}$ samples are calculated from the yields of observed γ -rays of 2003.7 keV, 602.7 keV and 416.9 keV, respectively (see Table 4.3). These γ -rays could be observed only in the close counting geometry in the TiLES (high efficiency), in case

of higher intensities in the respective decay chains. The activity thus obtained for a particular reaction product was then used to estimate the expected background from gamma rays in the ROI using known branching ratios (see Table 4.3). Table 4.4 gives the expected yield of such high energy gamma rays in the ^{nat}Cu , ^{nat}Pb and $^{124,nat}\text{Sn}$ samples. The neutron flux is corrected for solid angle subtended by targets in the cascade geometry, placed at different distances (d) from the production target. It should be noted that the coincidence summing of low energy gamma rays in these decay cascades can also produce gamma background in the ROI, which will depend on the detector configuration.

Table 4.4: Estimated neutron-induced background from the high energy γ -rays in Pb, Cu and Sn samples.

Sample	Neutron fluence $n\text{ cm}^{-2}(\times 10^{10})$	Reaction Product	$T_{1/2}$	E_γ of interest (keV)	Expected Intensity of E_γ ($Bq\text{ g}^{-1}$)
^{nat}Pb	0.30(2)	^{124}Sb	60.2 d	2182.6 2294.0	0.0007(3) 0.0005(2)
^{nat}Cu	0.33(2)	^{62m}Co	13.91 min	2301.9 2882.3	6(2) 4(1)
^{124}Sn	1.6(1)	^{116m}In	54.29 min	2112.3	5(1)
^{nat}Sn	0.84(6)	^{116m}In	54.29 min	2112.3	24(6)

Most of the activities producing high energy gamma-rays are short-lived and can be minimized by storage in an underground location prior to use in the detector setup. Typical neutron flux in underground locations at $E_n <$

10 MeV is $10^{-6} \text{ n cm}^{-2}\text{s}^{-1}$ [116] and the required overall background level will be $<10^{-2} \text{ counts}/(\text{keV kg y})$. Hence, contribution from Cu and Pb samples in the region of high energy gamma rays would be negligible. From Table 4.4, it can be seen that $^{\text{nat}}\text{Sn}$ will produce $\sim 5(2)$ times higher gamma background of 2112.3 keV on neutron activation and can be of concern.

4.4 Thermal Neutron-induced Background in $^{\text{nat}}\text{Sn}$

Fast neutrons after thermalisation in the shield can produce significant background by radiative capture reactions (n, γ) in the detector/source assembly. To investigate the long-lived activities generated by thermal neutrons, the $^{\text{nat}}\text{Sn}$ sample (7N purity, mass $\sim 1.9 \text{ mg}$) was irradiated with thermal neutrons of flux $5 \times 10^{13} \text{ n cm}^{-2} \text{ s}^{-1}$ for 1 minute at Dhruva Reactor, BARC. The irradiated samples were counted in the TiLES after a cool down time of 90 d after the neutron irradiation time and the gamma ray spectrum is shown in Figure 4.11. Table 4.5 lists the products together with their respective half lives [111] for the observed gamma rays in the sample.

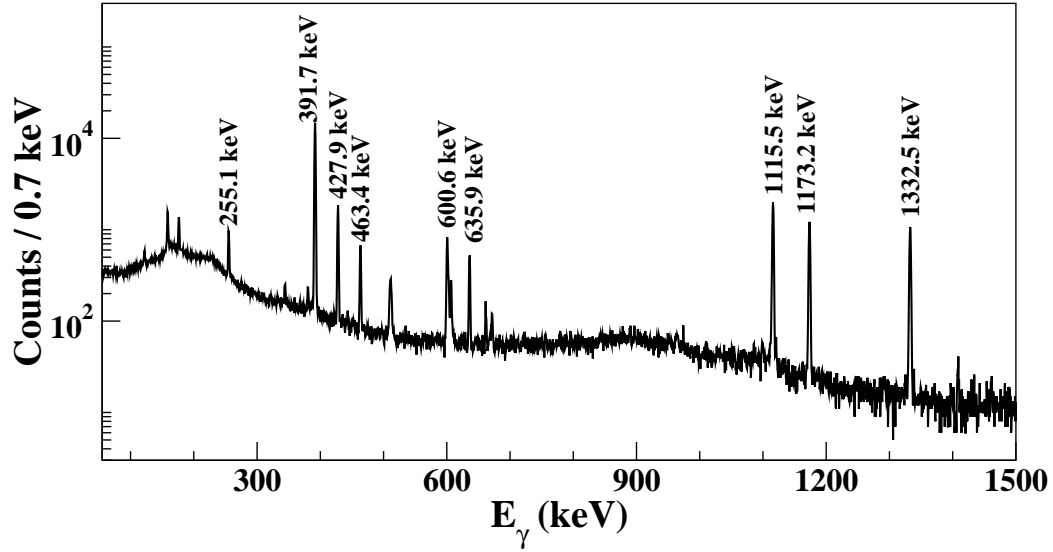


Figure 4.11: Gamma ray spectra of the ^{nat}Sn sample irradiated with thermal neutrons. The time elapsed since irradiation is $t_c = 90$ days ($T_{data} = 1$ d).

Table 4.5: Thermal neutron-induced reaction products, $T_{1/2}$ and observed γ -rays in the ^{nat}Sn sample.

Sample	Reaction channel	$T_{1/2}$	E_γ (keV)
^{nat}Sn	$^{112}\text{Sn}(n, \gamma)^{113}\text{Sn}$	115.09 d	255.1, 391.7
	$^{124}\text{Sn}(n, \gamma)^{125}\text{Sn}$, $^{125}\text{Sn}(n, \gamma)^{125}\text{Sb}$	2.75856 y	176.3, 427.9, 463.4, 600.6, 606.7, 635.9, 671.4
	$^{64}\text{Zn}(n, \gamma)^{65}\text{Zn}$	243.93 d	1115.5
	$^{59}\text{Co}(n, \gamma)^{60}\text{Co}$	5.27 y	1173.2, 1332.5

It is not clear if the Zn and Co impurities were present in the sample or were deposited from the reactor environment. It is evident from Table 4.5

that most of the products formed are long-lived ($T_{1/2} \sim \text{y}$) and decay by β -emission. The electrons produced with $Q_{\beta} \geq Q_{\beta\beta}$ (^{124}Sn) will contribute to the background. This emphasizes the need to study thermal neutron-induced background in other surrounding materials.

4.5 Summary

Neutron-induced background, both at thermal and fast neutron energies, has been studied in various materials to be used in TIN.TIN detector such as Torlon 4203 and 4301, Teflon, $^{\text{nat}}\text{Cu}$, $^{\text{nat}}\text{Pb}$ and $^{124,\text{nat}}\text{Sn}$. The contribution to the gamma background has been evaluated for an average neutron flux $\sim 10^6 \text{ n cm}^{-2}\text{s}^{-1}$ integrated over neutron energy $E_n = \sim 0.1$ to ~ 18 MeV. Both Torlon samples show the presence of Al which will contribute to high energy gamma background. In addition, Torlon 4301 has Fe impurity while Ti in Torlon 4203 can produce long-lived impurities like ^{46}Sc . Teflon shows only 511 keV γ -ray activity resulting from $^{19}\text{F}(n, 2n)^{18}\text{F}$ reaction at $E_n \geq 11.5$ MeV. Hence, Teflon appears to be a better material for support structures in the Sn cryogenic bolometer from neutron-induced background consideration. Although, the $^{\text{nat}}\text{Cu}$ sample and Sb impurity in $^{\text{nat}}\text{Pb}$ produces high energy gamma background ($E_{\gamma} > 2.1$ MeV) upon neutron activation, the contribution in the ROI of $0\nu\beta\beta$ decay in ^{124}Sn is estimated to be negligible. The neutron-induced reactions form short-lived

activities in both ^{124}Sn and $^{\text{nat}}\text{Sn}$ samples, which are of concern for the Tin detector. Among the various Sn isotopes formed ^{123}Sn has the longest half-life $T_{1/2} = 129.2$ d, while $^{116\text{m}}\text{In}$ produces high energy γ -ray of 2112.3 keV. Thus, for background reduction enriched Tin is preferable as compared to natural Tin. The $^{\text{nat}}\text{Sn}$ produces $\sim 5(2)$ times higher gamma background of 2112.3 keV γ -ray than ^{124}Sn on neutron activation. Thermal neutrons can produce long-lived isotopes in $^{\text{nat}}\text{Sn}$ like ^{113}Sn ($T_{1/2} = 115.09$ d). These results suggest that it would be necessary to store Sn material in underground location for extended periods prior to use in the cryogenic bolometer setup.

Chapter 5

Estimation of Neutron Flux at INO

Cavern

5.1 Introduction

As discussed in Chapter 1, neutrons are known to be an important source of background for experiments like direct dark matter searches, double beta decay experiments, solar neutrino measurements, etc. In underground laboratories, neutrons originate from the presence of U and Th trace elements in the surrounding rock. Neutrons induced by cosmic-ray muon interactions with rock and shielding material are generally more penetrating because of higher energy ($E_n > 20$ MeV) but expected flux is ~ 100 – 1000 times lower [101, 102]. To reach the desired sensitivity in the experiment, the neutron background from rock, detector components and cosmic-ray muons should be significantly suppressed. The neutron background from

rock ($E_n < 20$ MeV) can be reduced by installing passive shield of hydrocarbon material or water surrounding the detector. MC simulations are required to optimize the shield configuration and composition.

This chapter describes the estimation of the neutron flux in the cavern from the BWH rock activity (spontaneous fission and (α, n) interactions). A volume source distributed uniformly in a finite size rock element is considered in the simulations, where the strength of the source is derived from the BWH rock composition. The total neutron flux is estimated at the center of a 12 m long cylindrical tunnel of 4 m diameter and a concept design of shield for reduction of this neutron flux is also presented. Based on the shield requirement, the experimental hall dimensions for TIN.TIN detector are projected.

5.2 Neutron Production in the INO Cavern

In an underground cavern, neutrons from the surrounding rock are produced in two ways : (1) spontaneous fission of U, Th present in the rocks, (2) α particles emitted in the decay chains of U, Th induces (α, n) interactions with the low Z elements present in the rock. Therefore, it is essential to know the composition of the rock, mainly the content of U, Th and low Z isotopes.

5.2.1 Elemental Analysis of BWH Rock

The INO cavern will be located in Bodi West Hills (BWH), Madurai, India [74]. The BWH rock is mainly Charnockite, which is the hardest known rock, having a density of $\sim 2.89 \text{ g/cm}^3$. The BWH rock composition is obtained from TOF-SIMS method [105]. Table 5.1 shows various constituent elements of the BWH rock together with respective concentrations. Since

Table 5.1: Elemental distributions of BWH rock obtained with TOF-SIMS method.

Element	Concentration (% Weight)	Element	Concentration (% Weight)
$^1\text{H}, ^2\text{H}_2$	1.1	^{32}S	0.1
$^6\text{Li}, ^7\text{Li}$	0.001	$^{39,40,41}\text{K}$	4
^{12}C	2	^{40}Ca	9.99
$^{16}\text{O}, ^{32}\text{O}_2$	2.04	^{52}Cr	0.49
^{23}Na	5	^{56}Fe	1
$^{24,25,26}\text{Mg}$	7	$^{58,60}\text{Ni}$	0.55
^{27}Al	25	$^{63,65}\text{Cu}$	1.2
$^{28,29,30}\text{Si}$	40	$^{107,109}\text{Ag}$	0.05
^{31}P	3	^{120}Sn	0.6
^{197}Au	0.01		

the SIMS method has limited sensitivity $\geq 100 \text{ ppb}$, the Inductively Coupled Plasma Mass Spectrometry (ICPMS) method was used to obtain the U, Th concentration in the rock [117]. It was found that the BWH rock contains 60 ppb of ^{238}U and 224 ppb of ^{232}Th . In the present work, the BWH

rock is assumed to be a homogeneous mixture of its constituent elements and the U, Th impurities are distributed uniformly in the rock.

5.2.2 Neutron Yield from the BWH Rock

Table 5.2 gives the half-lives of spontaneous fission ($T_{1/2}^{SF}$) together with the natural abundances of U, Th isotopes and the spontaneous fission neutron yield. Due to very small isotopic abundance, contribution from ^{235}U to

Table 5.2: The spontaneous fission neutron yield of the U, Th isotopes [118].

Element	Nat. Abundance (%) [111]	$T_{1/2}^{SF}$ (y)	Yield n/(s g)	Neutron Multiplicity
^{232}Th	100	1.22×10^{21} [119]	9.99×10^{-8}	2.14
^{235}U	0.7204	3.5×10^{17}	2.99×10^{-4}	1.86
^{238}U	99.2742	8.20×10^{15}	1.36×10^{-2}	2.01

the neutron flux is expected to be negligible. Hence, only ^{238}U and ^{232}Th decays are considered here. The spectrum of the neutrons emitted in SF is described by an analytic function, known as Watt spectrum [120], which is given by:

$$W(a, b, E) = Ce^{-E/a} \sinh(\sqrt{bE}) \quad (5.1)$$

where $C = \sqrt{\left(\frac{\pi b}{4a}\right)} \left(\frac{e^{b/4a}}{a}\right)$

The parameters a and b are empirically derived for each isotope (see Table 5.3).

Table 5.3: The Watt spectrum parameters for ^{238}U and ^{232}Th .

Isotope	a (MeV)	b (MeV $^{-1}$)
^{238}U [120]	0.7124	5.6405
^{232}Th [121]	0.80	4.0

Table 5.4 lists the average energy $\langle E_\alpha \rangle$ of the α particles emitted in U, Th decay chains, the alpha decay $T_{1/2}^\alpha$ and alpha yield. It should be noted that the α particles have a very short range ($\sim 50 \mu$ at $E_\alpha = 10$ MeV) in the rock. The (α, n) reaction rate will depend on the initial energy of the emitted alpha particle, the reaction Q value and the Coulomb barrier. For

Table 5.4: Details of the alpha yield of the U and Th isotopes [118].

Isotope	$\langle E_\alpha \rangle$ (MeV)	$T_{1/2}^\alpha$ (y)	Alpha Yield (α / (s-g))
^{238}U	4.19	4.47×10^9	1.2×10^4
^{232}Th	4.00	1.41×10^{10}	4.1×10^3

the present work, the thick target (α, n) reaction yields ($N(E)$ - neutrons per MeV) for low Z elements ($Z \leq 29$) have been taken from Refs. [122]

and [123]. The total thick target neutron yield is determined by the sum of the individual element yield weighted by its mass ratio in the BWH rock (as per Table 5.1). Since the neutron yield data for ^{40}Ca , ^{31}P could not be obtained from literature, it is assumed to be the same as that of Si. The neutron yields thus obtained, normalized to U and Th content of the BWH rock, are shown in Figure 5.1. The (α, n) component dominates at lower

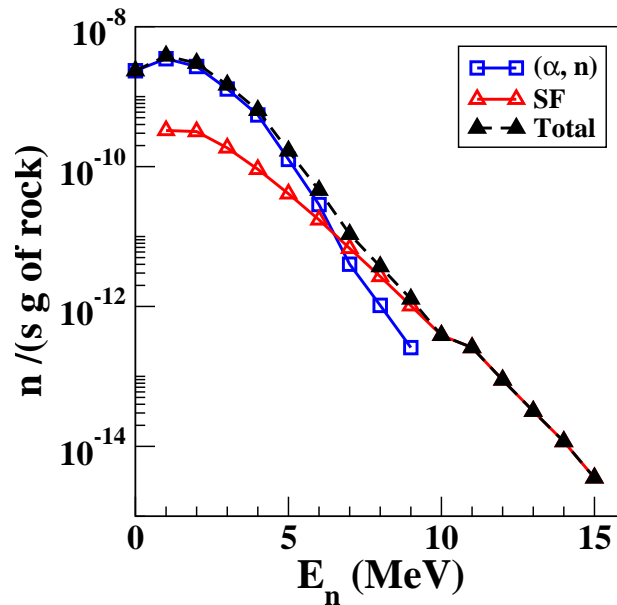


Figure 5.1: Neutron spectra for BWH rock with 60 ppb of ^{238}U and 224 ppb of ^{232}Th .

neutron energies while the SF dominates at higher energies. The data for (α, n) was not available for $E_n > 8$ MeV, but from the trend it is clear that the (α, n) contribution is ~ 100 times lower than that of the SF for $E_n > 8$ MeV.

5.3 MC Simulation of Neutron Flux at INO Cavern

The underground observatory at the INO site will have a rock cover of ~ 1000 m on all sides. However, the neutron flux will get attenuated in \sim few meters of rock [124] and hence only a finite size rock element will contribute to the neutron flux in the cavern. As can be seen from Figure 5.1, neutron source in the rock material is very weak and the flux rapidly decreases with energy. This will necessitate the large scale simulations and will be prone to errors due to statistical fluctuations. To overcome this problem, an alternative approach using MC simulations has been employed. For mono-energetic, uniformly distributed, isotropically emitted neutrons within the volume of the rock element, energy spectra ($N(E_j)$) after transmission through a rock element were computed. The size of the rock element was optimized such that $N(E_j)$ reaches a saturation value for the highest incident neutron energy $E_n = 15$ MeV (in steps of 1 MeV). The transmission factor $T(E_j, E_i)$ – the fraction of neutrons with initial energy E_i and emerging with final energy E_j is computed for $E_i = 1$ to 15 MeV for this optimal sized rock element. The neutron flux $N(E_j)$ (in units of $\text{cm}^{-2} \text{s}^{-1}$) per unit area at the surface of the rock is then computed using:

$$N(E_j) = \sum_i T(E_j, E_i) N(E_i) \quad (5.2)$$

where $N(E_i)$ is taken from the total neutron spectrum of the BWH rock given in Figure 5.1. Finally the neutron flux seen by the detector is estimated at the center of the tunnel by integrating over the entire cylindrical surface of the tunnel.

The GEANT4-based MC simulation studies have been done using the G4NDL4.0 neutron cross-section library. Since the neutron flux rapidly decreases with energy (by about \sim six orders of magnitude at $E_n = 15$ MeV), only $E_n \leq 15$ MeV is considered in the simulations. Typically, 10^6 events were generated at each incident energy and final energy spectra is made with bin widths of 1 MeV.

5.4 Neutron Transmission through the BWH Rock

As mentioned earlier, neutrons are attenuated as well as scattered in the rock. To understand these effects as a function of neutron energy, simulations were done for different configurations. For investigating the attenuation effect, a mono-energetic point source of neutrons placed behind a 40×40 cm² BWH rock of different thicknesses was considered. Figure 5.2 shows the neutron transmission probability ($P(E_i)$) as a function of rock thickness for $E_n = 1 - 20$ MeV. It can be seen that the flux of neutrons of $E_n = 15 - 20$ MeV reduces by two orders of magnitude after propagation through 30 cm thick BWH rock. It should be pointed out that $P(E_i)$

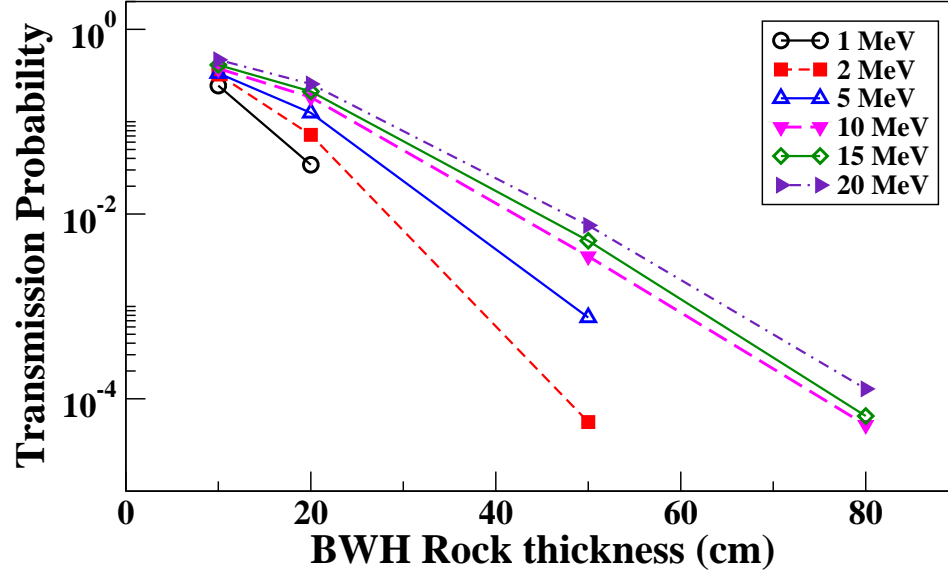


Figure 5.2: Neutron transmission probability as a function of rock thickness for a mono-energetic point source.

decreases because neutrons lose energy, and as a result the yield of low energy neutrons ($N(E_j), E_j < E_i$) is enhanced. However, the low energy neutron yield is also affected by scattering in surrounding material. To understand the effect of the surrounding material, the rock volume was subdivided into inner cylinder and outer cylindrical shell. The inner cylinder was further divided into two cylinders RI and RII with diameter $\phi = 30$ cm and length $L = 30$ cm. The outer shell (RIII) dimensions were chosen to be $\phi = 90$ cm and $L = 60$ cm. These dimensions were chosen on the basis of Figure 5.2. The schematic geometry of these sub-divided volumes (I, II and III) is shown in Figure 5.3. The figure also shows a thin detector of size

$\phi = 30$ cm, $L = 0.2$ cm placed on the face of the RI for recording transmitted neutrons.

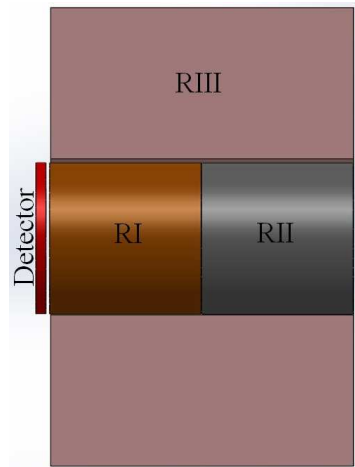


Figure 5.3: Schematic geometry of rock elements RI, RII and RIII considered in the simulations.

Simulations were done for following three configurations with uniform volume source :

- Case 1: RI-rock, RII and RIII-Air : Neutrons in RI.
- Case 2: RI, RII-rock, RIII-Air : Neutrons in RII.
- Case 3: RI, RII, RIII-rock : Neutrons in RI.

A typical spectrum for the first configuration is shown in Figure 5.4.

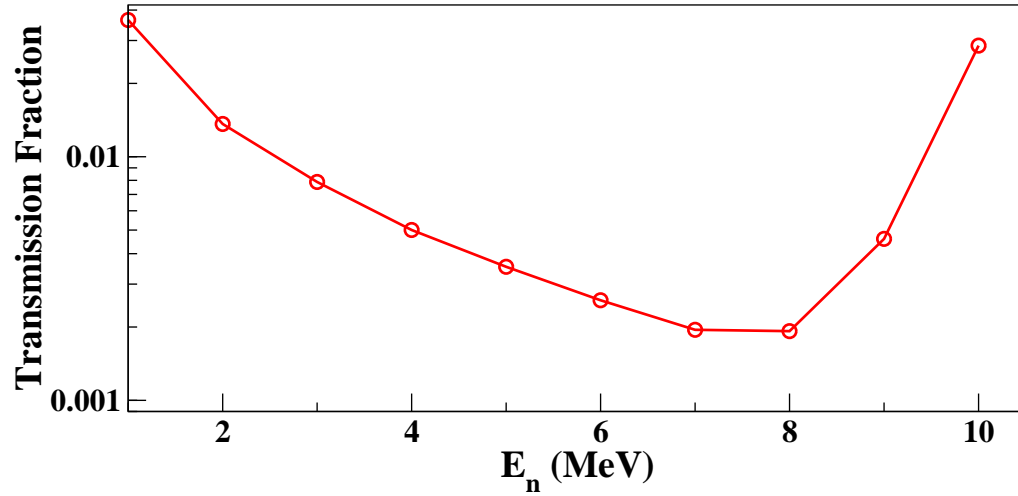


Figure 5.4: Neutron spectra after propagation through RI for incident neutron energy $E_n = 10$ MeV.

The total transmitted neutron spectrum was generated using :

$$N(E_f) = \sum_i T(E_f, E_i) N(E_i)$$

$$\text{where } N(E_i) = N_0 \delta(E_i)$$

The spectra for all three configurations after source strength normalization are shown in the Figure 5.5.

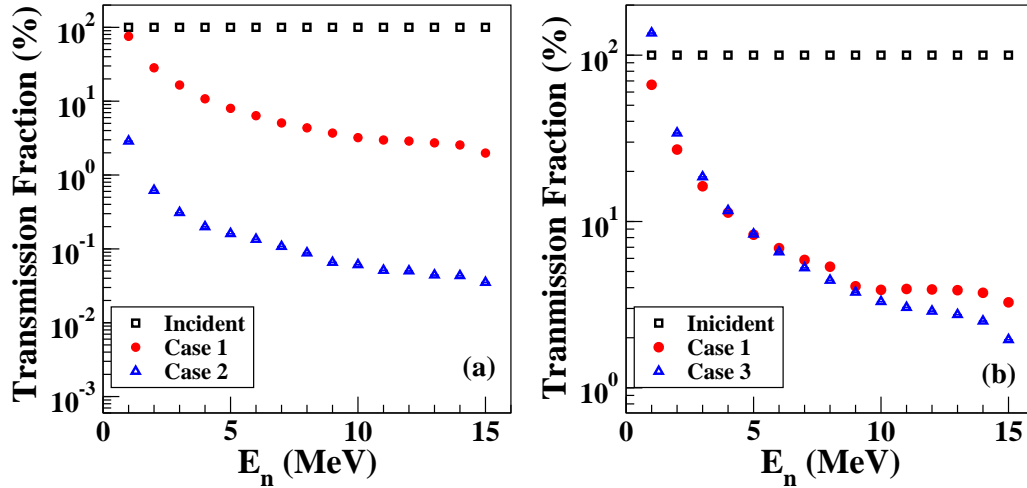


Figure 5.5: (a) Neutron transmission shown for Case 1 (red circle) and Case 2 (blue triangle) and (b) Neutron transmission shown for Case 1 (red circle), Case 3 (blue triangle) (see text for details)

It can be seen that the overall contribution from the RII is only about 10% of that of the RI. Further, reduction in the flux at higher energies ($E_n > 10$ MeV) is greater than that at lower energies. The enhancement in the low energy yield arising due to scattering in surrounding rock material is clearly visible in Figure 5.5(b) in the spectrum corresponding to configuration 3. It is expected that after finite thickness the contribution due to scattering effects will saturate.

5.5 Rock Element Size Optimization

In order to find the rock thickness where the scattering effects are saturated, simulations were done for cylindrical rock elements of diameters (d)

(90, 100, 110, 130, 150 cm). In each case, length of the cylinder was kept same as the diameter to ensure equal transmission length in all directions. The transmitted neutron spectrum was generated for the highest incident neutron energy $E_n = 15$ MeV and is shown in Figure 5.6 for one of the configurations. Since the scattering is expected to enhance the low energy yield, the transmission fractions for different energy ranges (0-5, 6-10, 11-15 MeV) were studied for each geometry and are shown in Figure 5.7.

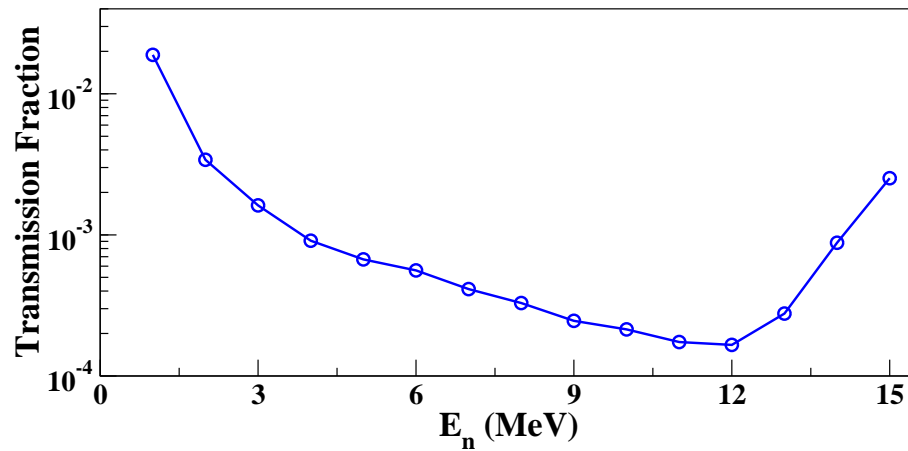


Figure 5.6: Neutron energy spectra for incident neutron energy $E_n = 15$ MeV for the rock element $d = L = 90$ cm.

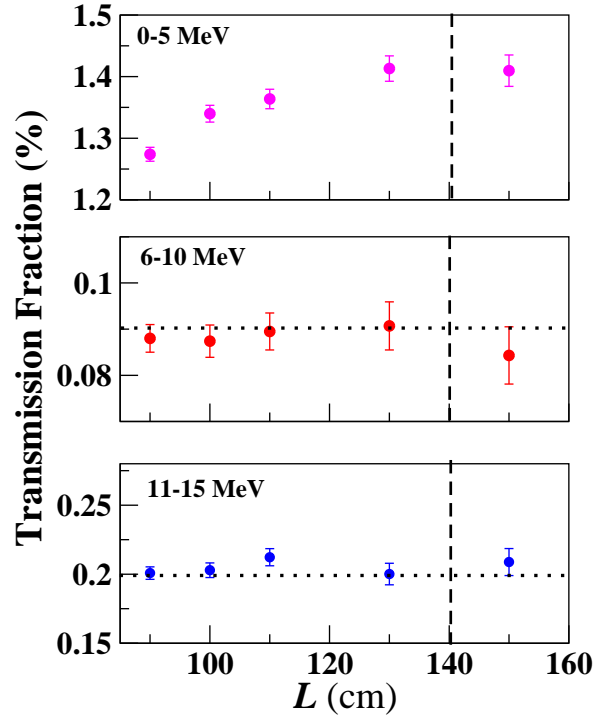


Figure 5.7: Transmission fraction of neutron for $E_n = 15$ MeV as a function of $d = L$ of the rock element for the different energy ranges. Each rock element have been scaled to the volume of element with $d = L = 90$ cm.

While for high neutron energies ($E_n > 5$ MeV) the transmission fraction is nearly constant, the saturation value in the low energies window ($E_n = 1 - 5$ MeV) is reached only for rock elements size $d = L > 130$ cm. Hence the optimal size of rock element is chosen to be $d = L = 140$ cm. Figure 5.8 shows the neutron spectra from this unit rock element which are used to generate transmission matrix $T(E_j, E_i)$ mentioned earlier.

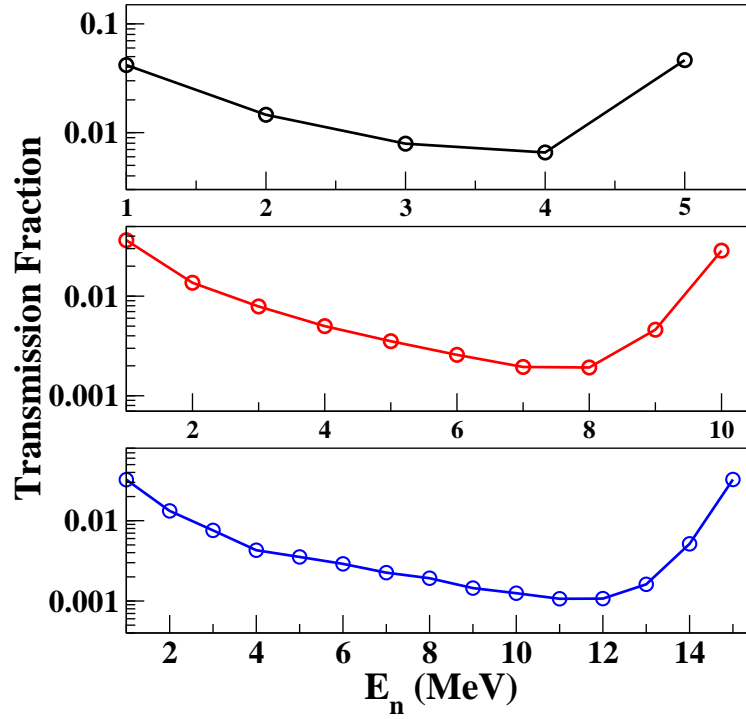


Figure 5.8: Neutron spectra of incident neutron energy (a) $E_n = 5$ MeV, (b) $E_n = 10$ MeV and (c) $E_n = 15$ MeV for rock element $d = L = 140$ cm.

The total neutron flux $N_s(E_j)$ is obtained at the surface of this BWH unit rock element using Eq. 5.2. It should be noted that the $N_s(E)$ thus obtained represents the flux at any point on the surface of the cylindrical tunnel.

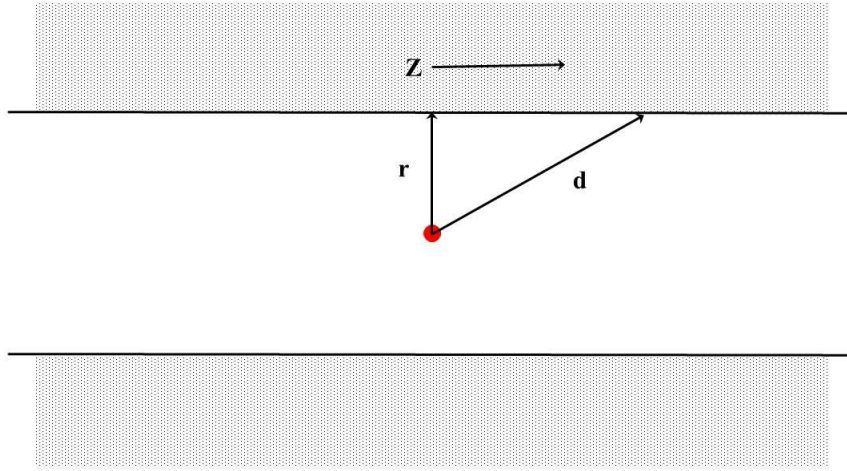


Figure 5.9: A schematic diagram of the underground tunnel assumed as a cylinder. The surrounding rock is shown by the shaded portion.

Assuming the experimental hall to be a cylindrical tunnel of radius $r = 2$ m and $L = 12$ m (see Figure 5.9), the neutron flux $N_f(E)$ at its center can be estimated as :

$$\begin{aligned}
 N_f(E) &= \int_{\phi=0}^{2\pi} \int_{z=-6}^6 \frac{N_s(E)}{A} \frac{A}{d^2} r d\phi dz \\
 &= N_s(E) 2\pi \int_{z=-6}^6 \frac{r}{r^2 + z^2} dz \quad (5.3) \\
 &= N_s(E) 2\pi \left[\arctan\left(\frac{z}{r}\right) \right]_{z=-6}^6 \\
 &= 7.84 \times N_s(E)
 \end{aligned}$$

The half length of the cylinder was restricted to 6 m since the contribution to the flux from larger lengths will be smaller than 10%. Moreover, additional shield could be provided at this distance in the tunnel. It should be mentioned that no additional scatterings from tunnel walls was considered in this estimation. Figure 5.10 shows the estimated neutron flux $N_f(E)$ at the center of the tunnel in the range $E_n = 1 - 15$ MeV. The energy inte-

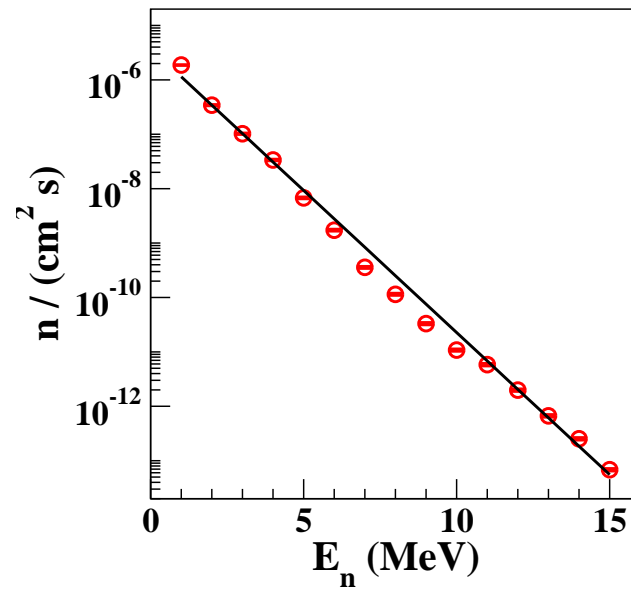


Figure 5.10: The estimated neutron flux ($N_f(E)$) at the center of an underground tunnel at INO site. The unfilled circle represents the MC data and the line corresponds to the exponential fit in the range of $E_n = 2 - 15$ MeV.

grated neutron flux obtained is $3.2 \times 10^{-6} \text{ n cm}^{-2} \text{ s}^{-1}$ from the rock activity.

This calculated spectrum can be approximately described by an exponential

function:

$$N(E) = 3.8 \times 10^{-6} \exp(-1.203 E) \quad (5.4)$$

It should be mentioned that neutrons will also originate from the radioactivity of the concrete of the experimental hall, the exact composition of which is presently not known.

5.6 Concept Design for Neutron Shield

The shield used for neutrons is made of hydrogen-rich materials such as water, paraffin, etc. Boron is generally added to the paraffin to absorb thermal neutrons. To estimate the required shield size, simulations have been done with mono-energetic point neutron source ($E_n = 1 - 20$ MeV) at the rock surface. Borated (5% ^{nat}B) [125] paraffin of different thicknesses was employed in MC simulations to study the neutron attenuation in the paraffin shield. The Borated Paraffin (BPE) of thickness 20 cm reduces the neutron flux of $E_n = 20$ MeV to 0.4%. In hydrogenous materials neutron capture by proton releases a γ -ray of energy 2224.573(0.002) keV (the binding energy of Deuterium), which is close to the $Q_{\beta\beta}$ (^{124}Sn). Hence additional Pb shield needs to be inserted between the paraffin. The Pb thickness was varied between 2-6 cm and optimum value was found to be 5 cm. Figure 5.11

shows the simulation geometry (panel a) together with the gamma-ray spectra before and after the 5 cm thick Pb (panel b). It is evident that composite

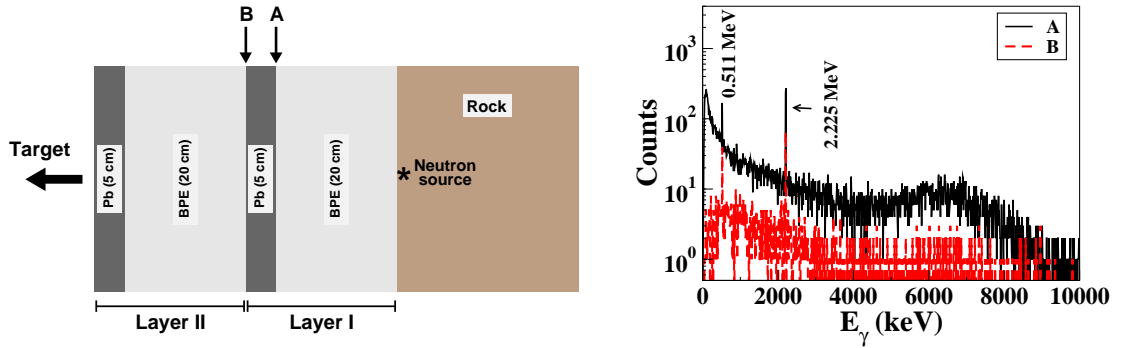


Figure 5.11: (a) Neutron shield using (BPE + Pb) between the rock and experimental hall, (b) Gamma-ray spectra after positions A and B for $E_n = 20$ MeV.

BPE + Pb shield is required to reduce the net background from the rock.

Table 5.5 lists the gamma background (N_γ) produced per incident neutron after Layer I for a given neutron energy.

Table 5.5: Gamma background (N_γ) produced per incident neutron after Layer I for different incident neutron energies.

E_n (MeV)	N_γ (0-10 MeV)	N_γ (2.2 MeV)
1	6.4×10^{-4}	2.5×10^{-5}
5	1.0×10^{-3}	4.6×10^{-5}
10	2.0×10^{-2}	7.9×10^{-5}
20	3.9×10^{-2}	1.9×10^{-3}

The transmission probability of low energy neutrons decreases rapidly with absorber thickness and hence MC output will have large statistical errors. To overcome this problem, the absorber thickness t was sub-divided into smaller blocks of equal thickness $t/2$ or $t/4$. If $T(E_j, E_i)$ is the transmission probability for neutron of energy E_i to emerge with energy E_j after traversing the thickness t , then $T_2(E_j, E_i)$ corresponding to thickness $2t$ (i.e. $t + t$) can be obtained as:

$$T_2(E_j, E_i) = \sum_{k=j}^i T(E_j, E_k) T(E_k, E_i) \quad (5.5)$$

In the present work MC simulation were done for 5 cm BPE ($E_n = 1 - 5$ MeV), 10 cm BPE ($E_n = 6 - 10$ MeV) and 20 cm BPE ($E_n = 11 - 20$ MeV). The choice of thickness for different energy windows ensured that simulation errors were around $\sim 3\%$. Figure 5.12 shows a comparison of neutron transmission for $E_i = 10$ MeV obtained by this method and from MC simulations ($N_n = 10^6$). It is seen that the overall shape is well reproduced and the errors in the folding approach are considerably smaller. Using this approach the neutron spectrum in the cavern $N_f(E)$ (shown in Figure 5.10) after 20 cm and 40 cm BPE is computed and is shown in Figure 5.13. It is clear that two layers of BPE (total 40 cm) will be sufficient to reduce the neutron flux even at $E_n = 15$ MeV ($\sim 10^{-6}$). It would be of interest to

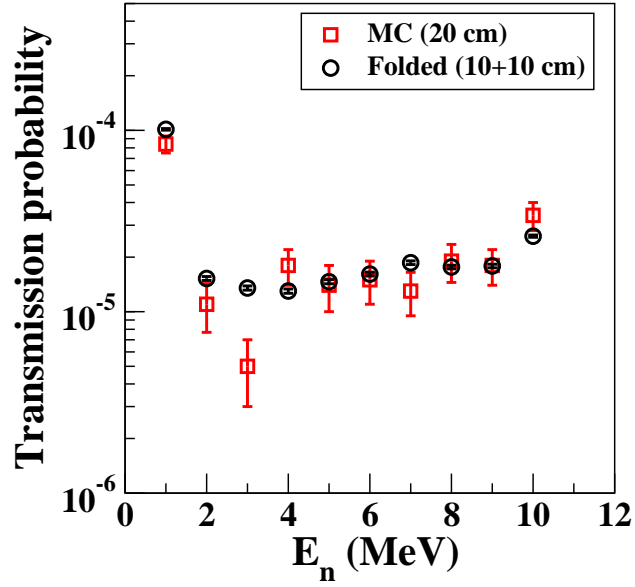


Figure 5.12: Transmission probability obtained from MC and the folding technique through 20 cm BPE for $E_n = 10$ MeV.

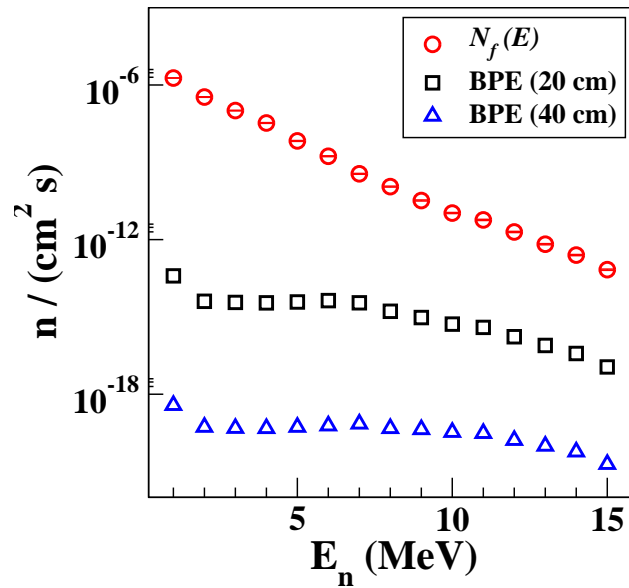


Figure 5.13: Neutron spectra ($N_f(E)$) at the center of an underground tunnel at INO site after propagation through 20 cm and 40 cm BPE.

study other neutron shield materials (wood, water) and the Boron fraction to assess the impact on gamma background.

5.6.1 Laboratory Size Requirements for TIN.TIN

It is envisaged that the large scale TIN.TIN detector (of mass ~ 1 ton) will consist of an array of Sn bolometers in a cryostat. The sensitivity of a large detector ~ 1 ton (90% enrichment) is estimated as $\langle m_{ee} \rangle \sim 50 - 100$ meV in one year observation time assuming ~ 0.01 counts/(keV kg y) background [71]. As discussed in earlier chapters, a Pb shield is required inside the cryostat for reducing the gamma background for the Sn array. Therefore, the expected size of the cryostat is ~ 1.5 m diameter and ~ 3 m height. According to the estimates obtained in the previous section, two layers of BPE (20 cm) + Pb (5 cm) are expected to be adequate for desired background levels (~ 0.01 counts/(keV kg y)). However, if the neutron background increases because of concrete or any other factor, then additional BPE + Pb layer may be necessary. Assuming three composite layers of neutron shield (BPE (20 cm) + Pb (5 cm)) around the cryostat, the required space for the detector + shield will be of $3 \text{ m} \times 3 \text{ m}$. A minimum clearance of ~ 1 m is required from the walls of the experimental hall to reduce the background. Considering this, the laboratory size of $10 \text{ m} \times 10 \text{ m}$ and height of 5 m is essential inside the cavern. Since the overall tunnel height in INO cavern is

around 5 m, it is proposed to make a 10 m \times 5 m wide pit with a depth of \sim 6 m, which will provide a total height of \sim 10 m. This will be required for mounting/dismounting detector shields and accessories. In addition, underground laboratories for material storage and processing will be necessary.

5.7 Summary

The neutron flux ($E_n \leq 15$ MeV) resulting from spontaneous fission and (α, n) interactions for BWH rock containing 60 ppb of ^{235}U and 224 ppb of ^{232}Th is estimated. Since the neutron source in the rock material is very weak and the flux rapidly decreases with energy, an alternative approach using MC simulations has been employed. It is shown that only finite rock size contributes to the neutron flux at surface and a rock element of size $d = L = 140$ cm is optimal to evaluate the neutron background. The total neutron flux at the center of a 4 m diameter, 12 m long tunnel in the underground cavern is determined. The estimated flux at low energy ($E_n \leq 15$ MeV) is 3×10^{-6} n cm $^{-2}$ s $^{-1}$. The composite shield design of three layers of BPE (20 cm) + Pb (5 cm) is proposed for significant reduction of neutron flux at the target site. Since hydrogen-rich shield material produces a γ -ray close to $Q_{\beta\beta}(^{124}\text{Sn})$, shield design require special consideration for gamma

attenuation. Based on this, the size requirements for the underground laboratory for TIN.TIN are projected as 10 m × 10 m and approximately 5 m tall.

Chapter 6

Summary and Future Outlook

Double Beta Decay is a rare second order transition which can take place when single beta decay is energetically forbidden or highly suppressed because of large spin differences. The $2\nu\beta\beta$ decay where two electrons and two $\bar{\nu}_e$ are emitted, does not violate lepton number and is allowed in the Standard Model. The $2\nu\beta\beta$ decay is predicted in about 35 even-even isotopes and has been observed in about 11 isotopes so far with $T_{1/2} \sim 10^{18} - 10^{24}$ y. Other modes of double beta decay like $\beta^+\beta^+$, β^+EC and $ECEC$ are also possible. Neutrinoless Double Beta Decay is a lepton number violating nuclear transition, possible only if neutrinos are their own antiparticles. If the process is mediated by the exchange of a light left-handed Majorana neutrino, its decay rate will depend on the square of the effective Majorana neutrino mass. Therefore, NDBD can provide information on the absolute scale of neutrino mass. The effective neutrino mass also

involves the two CP violating Majorana phases which cannot be probed by the neutrino oscillation experiments. Hence, NDBD is regarded as a golden channel to probe the fundamental nature of neutrinos. Worldwide, there are many ongoing experiments like GERDA, CUORE, EXO, KamLAND-Zen, etc. to study the NDBD in different isotopes. Until now, NDBD has not been observed and only a lower limit on $T_{1/2} \sim 10^{25}$ y has been set in ^{76}Ge and ^{136}Xe .

In India, a feasibility study has been initiated to search for $0\nu\beta\beta$ decay in ^{124}Sn using a Tin cryogenic bolometer. The bolometer detector offers good energy resolution (0.2% at $Q_{\beta\beta}$). The $Q_{\beta\beta}$ value of ^{124}Sn is 2292.64 ± 0.39 keV and it has a moderate isotopic abundance $\sim 5.8\%$. TIN.TIN (The India-based TIN detector) will be located at the upcoming underground facility INO. Given the rarity of the DBD processes, background understanding and minimization is crucial to improve the sensitivity of the measurement.

This thesis work involved radiation background studies for $0\nu\beta\beta$ search in ^{124}Sn . For this purpose TiLES (Tifr Low background Experimental Setup), a low background counting setup with a special HPGe detector, has been setup at sea level at TIFR. Detailed measurements are performed with point and extended geometry sources to generate an effective model of the detector with GEANT4 based Monte Carlo simulations. The effective detector

model agrees within 5.46(3)% with experimental data over a wide energy range of 100–1500 keV. The GEMS program is developed for MC simulation based efficiency computation for any source configuration in a close geometry. The setup is shielded with 5 cm low activity Cu shield, 10 cm low activity Pb ($^{210}\text{Pb} < 0.3 \text{ Bq/kg}$) shield and active veto system using plastic scintillators. The CADFLAP program is developed to generate the anti-coincidence spectra between the HPGe detector and the plastic scintillators. The setup has been extensively used for qualification and selection of radio-pure materials to be used in the prototype bolometer R&D as well as for background studies. The BWH rock sample from INO cavern was found to have considerably high level of ^{40}K (1050(16) mBq/g). The enriched Sn samples showed high levels of 661.7 keV γ -ray activity while the $^{\text{nat}}\text{Sn}$ (7N purity) samples has higher radioactivity of ^{40}K . In addition, gamma rays from Tin isotopes other than ^{124}Sn were observed in the $^{\text{nat}}\text{Sn}$ sample. Many gamma rays originating from neutron interactions were observed in the ETP Cu sample, emphasizing that an additional Pb shield will be essential around the Tin detector array inside the cryostat.

Neutron-induced background, both at thermal and fast neutron energies, has been studied in various materials to be used in TIN.TIN detector such

as Torlon 4203 and 4301, Teflon, ^{nat}Cu , ^{nat}Pb and $^{124,nat}\text{Sn}$. The contribution to the gamma background has been evaluated for an average neutron flux $\sim 10^6 \text{ n cm}^{-2}\text{s}^{-1}$ integrated over neutron energy $E_n = \sim 0.1$ to ~ 18 MeV. Both Torlon samples show the presence of Al which will contribute to high energy gamma background. In addition, Torlon 4301 has Fe impurity while Ti in Torlon 4203 can produce long-lived impurities like ^{46}Sc . Teflon shows only 511 keV γ -ray activity resulting from $^{19}\text{F}(n, 2n)^{18}\text{F}$ reaction at $E_n \geq 11.5$ MeV. Hence, Teflon appears to be a better material for support structures in the Sn cryogenic bolometer from neutron-induced background consideration. Although, the ^{nat}Cu sample and Sb impurity in ^{nat}Pb produces high energy gamma background ($E_\gamma > 2.1$ MeV) upon neutron activation, the contribution in the ROI of $0\nu\beta\beta$ decay in ^{124}Sn is estimated to be negligible. The neutron-induced reactions form short-lived activities in both ^{124}Sn and ^{nat}Sn samples, which are of concern for the Tin detector. Among the various Sn isotopes formed ^{123}Sn has the longest half-life $T_{1/2} = 129.2$ d, while ^{116m}In produces high energy γ -ray of 2112.3 keV. Thus, for background reduction enriched Tin is preferable as compared to natural Tin. The ^{nat}Sn produces $\sim 5(2)$ times higher gamma background of 2112.3 keV γ -ray than ^{124}Sn on neutron activation. Thermal neutrons can

produce long-lived isotopes in ^{nat}Sn like ^{113}Sn ($T_{1/2} = 115.09$ d). These results suggest that it would be necessary to store Sn material in underground location for extended periods prior to use in the cryogenic bolometer setup.

The neutron flux ($E_n \leq 15$ MeV) resulting from spontaneous fission and (α, n) interactions for BWH rock containing 60 ppb of ^{235}U and 224 ppb of ^{232}Th is estimated. Since the neutron source in the rock material is very weak and the flux rapidly decreases with energy, an alternative approach using MC simulations has been employed. It is shown that only finite rock size contributes to the neutron flux at surface and a rock element of size $d = L = 140$ cm is optimal to evaluate the neutron background. The total neutron flux at the center of a 12 m long tunnel in the underground cavern is determined. The estimated flux at low energy ($E_n \leq 15$ MeV) is 3×10^{-6} n cm $^{-2}$ s $^{-1}$. The composite shield design of three layers of BPE (20 cm) + Pb (5 cm) is proposed for significant reduction of neutron flux at the target site. Since hydrogen-rich shield material produces a γ -ray close to $Q_{\beta\beta}(^{124}\text{Sn})$, shield design require special consideration for gamma attenuation. Based on this, the size requirements for the underground laboratory for TIN.TIN is projected as 10 m x 10 m and approximately 5 m tall .

6.1 Possible Improvements in TiLES

The sensitivity of the TiLES is ~ 2 mBq/g for ^{40}K and ~ 1 mBq/g for ^{232}Th with the present shielding configuration and $T_{data} = 6$ d. For further improvement in background, ^{222}Rn contamination can be reduced by purging the system with pure dry N_2 gas. This will help in reducing the background originating from ^{214}Pb and ^{214}Bi . In addition, pulse shape discrimination can be applied between γ and $(\alpha + \beta)$ events. More plastic scintillators can be added to the existing setup for a better muon coverage. A cryo-free low background HPGe detector (Ortec, relative efficiency 30%) has been successfully tested at TIFR [126]. This is desirable for underground usage.

6.2 Rare Event Studies with TiLES

The low background gamma spectroscopy technique has been used to study rare decay events like DBD to the excited states of the daughter nuclei and rare alpha decays [127–131]. The TiLES can be used for such rare decay studies. For a number of nuclei DBD to excited states in their daughter nuclei are energetically possible. Its experimental signature would be the emission of a gamma ray from the nucleus. Table 6.1 gives the isotopes in which DBD can be studied in the TiLES [132].

Table 6.1: List of potential DBD Isotopes for TiLES [132].

Isotope	$Q_{\beta\beta}$ (keV)	Natural Abun. %	Exc. state	Expt. limits $T_{1/2}$ (y)	Theo. estimations $T_{1/2}$ (y)
^{154}Sm	1251	22.75	2_1^+ (123)	$> 2.3 \times 10^{18}$	1.6×10^{18}
^{94}Zr	1144	17.4	2_1^+ (871)	$> 1.3 \times 10^{19}$	10^{22-24}
^{160}Gd	1729.7	21.86	2_1^+ (87)	$> 2.1 \times 10^{19}$	–
^{170}Er	653.6	14.9	2_1^+ (84)	$> 3.2 \times 10^{17}$	–

The low energy gamma rays around 100 keV offer good detection efficiency but the background levels are dominated by the Compton continuum of high energy gamma rays. The candidate selected to study DBD decay to excited state is ^{94}Zr (see Figure 6.1). It should be mentioned that single beta decay in ^{96}Zr (natural abundance 2.8%) is suppressed by spin differences and a limit can be placed on β -decay in ^{96}Zr [133]. The $^{\text{nat}}\text{Zr}$ is available

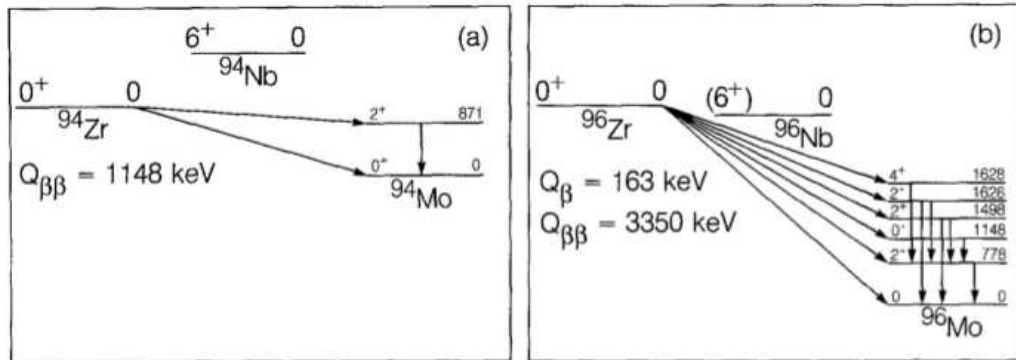


Figure 6.1: Decay schemes of (a) ^{94}Zr and (b) ^{96}Zr [133].

commercially in different forms. The FWHM at 871 keV gamma ray is ~ 2 keV in the TiLES.

Fast and thermal neutron induced background has been studied in the ^{nat}Zr foils (99.9% purity from Princeton Scientific Corp.). The irradiation time (t_{irr}) and neutron energies for the Zr irradiation are presented in Table 6.2 while the observed gamma rays with the corresponding channels of activation are given in Table 6.3. The Sr and Nb isotopes are found to be

Table 6.2: Details of Neutron Irradiation of ^{nat}Zr .

E_p (MeV)	t_{irr}	ϕ_n ($\text{n cm}^{-2} \text{s}^{-1}$)
12 MeV	12 h	$2.3(0.2) \times 10^5$
20 MeV	4 h, 13.7 h	$9.9(0.7) \times 10^5$
Thermal	1 min	1.3×10^{13}

Table 6.3: Neutron-induced reaction products, $T_{1/2}$ and observed γ -rays in the irradiated Zr samples. The minimum neutron energy E_n at which corresponding σ is $\geq \mu\text{b}$ is also listed [111].

Reaction channel	$T_{1/2}$ Refn.[111]	E_γ (keV)	E_n (MeV)
$^{90}\text{Zr}(n, p)^{90}\text{Y}$	3.19 h	202.5, 479.6, 681.8	3.2
$^{91}\text{Zr}(n, p)^{91\text{m}}\text{Y}$	49.7 m	555.6	2.9
$^{94}\text{Zr}(n, \gamma)^{95}\text{Zr}$	64.0 d	724.2, 756.77	–
$^{96}\text{Zr}(n, \gamma)^{97}\text{Zr}$	16.7 h	743.3	–
$^{90}\text{Zr}(n, 2n)^{89}\text{Zr}$	78.4 h	909.1, 1713.0	12.4
$^{93}\text{Nb}(n, 2n)^{92}\text{Nb}$	10.15 d	934.4	9
$^{86}\text{Sr}(n, \gamma)^{87}\text{Sr}$	2.8 h	388.5	–

present as impurities in the ^{nat}Zr sample. From Table 6.3, it can be seen that the most dominant reactions (n, γ) at thermal neutron energies give rise to gamma background less than 871 keV gamma ray. The ^{nat}Zr foils were counted in a close geometry in the TiLES to estimate the background sensitivity in the ROI, i.e. 871 ± 2 keV. A Monte Carlo study with GEMS was done to optimize the mounting geometry for 360 g of Zr foils. This was essential to minimize the self-absorption of 871 keV gamma ray in the Zr sample and maximize its detection efficiency. It was found that the 871 keV gamma ray attenuates by 26% in ~ 12 mm thick Zr plate. The counting of ^{nat}Zr was done in phases with a mass increase of ~ 50 g at each level to monitor the background in the ROI. Many gamma rays were observed in the spectrum of ^{nat}Zr (see Figure 6.2), mostly originating from the gamma transitions occurring in ^{97}Nb populated from the decay of ^{97}Zr [134]. The background index obtained in the ROI, i.e. around 871 keV, is ~ 59 counts/(keV kg d).

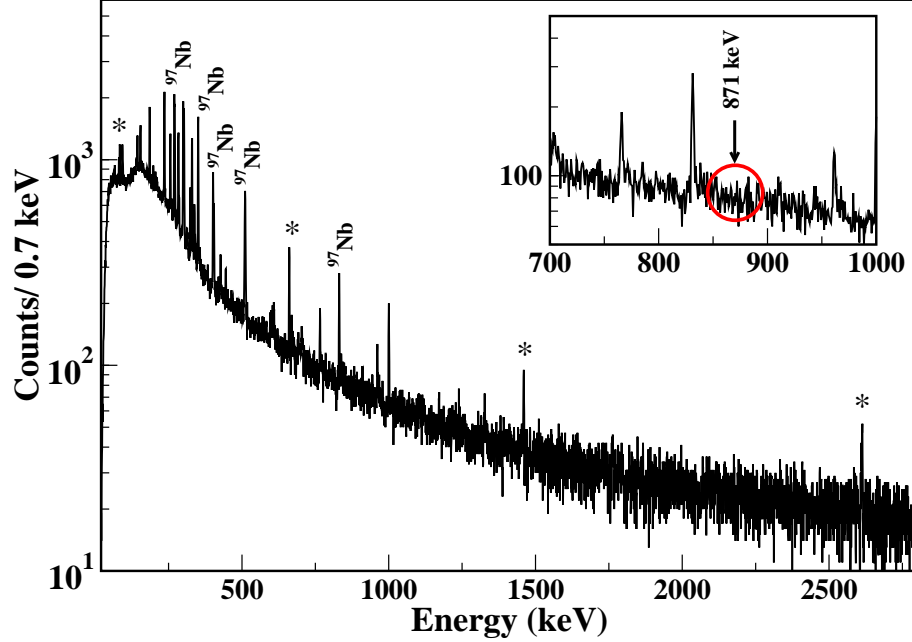


Figure 6.2: The gamma-ray spectra of ^{nat}Zr foils counted for 8 d in the TiLES. The inset shows the ROI around 871 keV gamma-ray.

The 871 keV gamma-ray was not visible above the background level and hence a lower limit on $T_{1/2}$ for DBD to the first excited state in ^{94}Zr is obtained using:

$$T_{1/2} > \frac{N_A \ln 2 \varepsilon a}{W k_{CL}} \sqrt{\frac{M t}{N_{bkg} \Delta E}} \quad (6.1)$$

where N_A is Avogadro's number, ε ($\sim 2.33\%$) is the detection efficiency of 871 keV, a (17.38%) is the isotopic abundance of ^{94}Zr (17.38%), W (91.22) is the molar mass of Zr, M is 360 g, t (y) is the time of measurement, N_{bkg} ($\text{g}^{-1}\text{keV}^{-1}\text{y}^{-1}$) is the background index, ΔE is the FWHM energy resolution of TiLES for 871 keV and k_{CL} is 1 corresponding to a 68% CL. The

$T_{1/2}$ obtained for DBD to the first excited state in ^{94}Zr is $1.59(0.08) \times 10^{18}$ y for ~ 35 g y exposure at 68% CL. The limit can be improved by \sim one order of magnitude (similar to the existing experimental limits $> 1.3 \times 10^{19}$ y) with long counting period (~ 150 g y) at the current background level. This also demonstrates the suitability/advantage of TiLES for rare event studies.

Glossary A

Glossary

Glossary of terms / acronyms (in order of appearance in the chapters).

$0\nu\beta\beta$: Neutrinoless double beta decay

$2\nu\beta\beta$: Two neutrino double beta decay

NDBD : Neutrinoless double beta decay

LH : Left-handed

RH : Right-handed

NH : Normal Hierarchy

IH : Inverted Hierarchy

IS : Inverted Spectrum

NS : Normal Spectrum

NO : Normal Ordering

IO : Inverted Ordering

PMNS : Pontecorvo-Maki-Nakagawa-Sakata

SUSY : SUper SYmmetric

NTME : Nuclear Transition Matrix Element

NSM : Nuclear Shell Model

QRPA : Quasi-Random Phase Approximation

ROI : Region Of Interest

FWHM : Full Width at Half Maximum

TIN.TIN : The INdia-based TIN detector

INO: India-based Neutrino Observatory

BWH : Bodi West Hills

TiLES : Tifr Low background Experimental Setup

MC : Monte Carlo

R.E. : Relative Efficiency

LAMPS : Linux Advanced Multi-Parameter System

DAQ : Data Acquisition system

NTD Ge : Neutron Transmutation Doped Germanium

DSP : Digital Signal Processing

DPP : Digital Pulse Processing

FPGA : Field Programmable Gate Array

OFHC : Oxygen-Free High thermal Conductivity

ETP : Electrolytic Tough Pitch

2N purity : purity at the level of 99%

7N purity : purity at the level of 99.99999%

TOF-SIMS : Time Of Flight Secondary Ion Mass Spectrometry

ENDF: Evaluated Nuclear Data File

ICPMS : Inductively Coupled Plasma Mass Spectrometry

T_{data} : Counting period of the gamma ray spectrum

t_c : Cooldown time after neutron irradiation

BPE : Borated Paraffin

CL : Confidence Level

BIBLIOGRAPHY

- [1] W. Pauli, Phys. Today **31N9** (1978) 27.
- [2] J. Chadwick, Nature **192** (1932) 312.
- [3] E. Fermi, Zeitschr. f. Phys. **88** (1934) 161.
- [4] M. Goepfert-Mayer, Phys. Rev. **48** (1935) 512.
- [5] E. Majorana, Nuovo Cimento **14** (1937) 171.
- [6] G. Racah, Nuovo Cimento **14** (1937) 322.
- [7] W.H. Furry, Phys. Rev. **56** (1939) 1184.
- [8] H. Primakoff, Phys. Rev. **85** (1952) 888.
- [9] T.D. Lee and C.N. Yang, Phys. Rev. **104** (1956) 254.
- [10] C.S. Wu *et al.*, Phys. Rev. **105** (1957) 1413.
- [11] H. Primakoff, S.P. Rosen, Report on Progress in Phys. **22** (1959) 121.
- [12] J. Schechter and J.W. F Valle, Phys. Rev. D **25** (1982) 2951.
- [13] T.D. Lee and C.N. Yang, Phys. Rev. **105** (1957) 1671.
- [14] F. Reines and C.L. Cowan, Nature **178** (1956) 446; F. Reines and C.L. Cowan, Phys. Rev. **113** (1959) 273.
- [15] M. Goldhaber, L. Grodzins and A.W. Sunyar, Phys. Rev. **109** (1958) 1015.
- [16] B. Pontecorvo, J. Exp. Theor. Phys. **33** (1957) 549.

- [17] B. Pontecorvo, J. Exp. Theor. Phys. **34** (1958) 247.
- [18] Z. Maki, M. Nakagawa, S. Sakata, Prog. Theor. Phys. **28** (1962) 870.
- [19] N. Cabibbo, Phys. Rev. Lett. **10** (1963) 531; M. Kobayashi and T. Maskawa, Prog. Theor. Phys. **49** (1973) 652.
- [20] R. Davis, Phys. Rev. Lett. **12** (1964) 302; R. Davis, Phys. Rev. Lett. **20** (1968) 1205.
- [21] J. N. Bahcall *et al.*, The Astrophys. J. **137** (1963) 344.
- [22] K.A. Olive *et al.* (Particle Data Group), Chin. Phys. C **38** (2014) 09001.
- [23] Y. Fukuda *et al.* (Super-Kamiokande Collaboration), Phys. Rev. Lett. **81** (1998) 1562; R. Wendell *et al.* (Super-Kamiokande Collaboration), Phys.Rev. D **81** (2010) 092004.
- [24] Q.R. Ahmad *et al.* (SNO Collaboration), Phys. Rev. Lett. **87** (2001) 071301; Q.R. Ahmad *et al.* (SNO Collaboration), Phys. Rev. Lett. **89** (2002) 011301.
- [25] K. Eguchi *et al.* (KamLAND Collaboration), Phys. Rev. Lett. **90** (2003) 021802; T. Araki *et al.* (KamLAND Collaboration), Phys. Rev. Lett. **94** (2005) 081801; S. Abe *et al.* (KamLAND Collaboration), Phys. Rev. Lett. **100** (2008) 221803;
- [26] M.H. Ahn *et al.* (K2K Collaboration), Phys. Rev. Lett. **90** (2003) 041801.
- [27] D.G. Michael *et al.* (MINOS Collaboration), Phys. Rev. Lett. **97** (2006) 191801; P. Adamson *et al.* (MINOS Collaboration), Phys. Rev. Lett. **106** (2011) 181801.
- [28] Talk presented by Thomas Schwetz in NuPhys2014: Prospects in Neutrino Physics, London, 15-17 Dec. 2014.
- [29] M.C. Gonzalez-Garcia, Michele Maltoni and Thomas Schwetz, J. of High Energy Physics **11** (2014) 052.

- [30] R. Saakyan, *Annu. Rev. Nucl. Part. Sci.* **63** (2013) 503.
- [31] W. Rodejohann, *Int. J. Mod. Phys. E* **20** (2011) 1833.
- [32] P. Vogel and M.R. Zirnbauer, *Phys. Rev. Lett.* **57** (1986) 3148.
- [33] V. Rodin, *J. of Phys: Conference series* **375** (2012) 042025.
- [34] S.M. Bilenky, C. Giunti, *Mod. Phys. Lett. A* **27** (2012) 1230015.
- [35] F.T. Avignone, S.R. Elliott, J. Engel, *Reviews of Modern Physics* **80** (2008) 481.
- [36] E. Fireman, *Phys. Rev.* **75** (1949) 323.
- [37] M.G. Inghram, J. H. Reynolds, *Phys. Rev.* **78** (1950) 822.
- [38] S.R. Elliott, A.A. Hahn, M.K. Moe, *Phys. Rev. Lett.* **59** (1987) 2020.
- [39] O. Cremonesi and Maura Pavan, *Advances in High Energy Physics*, **2014** (2014) 951432.
- [40] I. Ogawa *et al.*, *J. Phys. Conf. Ser.* **375** (2012) 042018.
- [41] B. Lehnert *et al.*, *Nucl. Inst. and Meth. A* **742** (2014) 254.
- [42] J. F. Wilkerson *et al.*, *J. Phys. Conf. Ser.* **375** (2012) 042010.
- [43] A. Barabash *et al.*, *J. Phys. Conf. Ser.* **375** (2012) 042012.
- [44] L. Cardani *et al.*, *J. Phys. Conf. Ser.* **375** (2012) 042016.
- [45] H. Bhang *et al.*, *J. Phys. Conf. Ser.* **375** (2012) 042023.
- [46] K. Fushimi *et al.*, *J. Phys. Conf. Ser.* **203** (2010) 012064.
- [47] C. Oldorf *et al.*, *J. Phys. Conf. Ser.* **375** (2012) 042022.
- [48] A. S. Barabash *et al.*, *JINST* **6** (2011) P08011.
- [49] P. Gorla *et al.*, *J. Phys. Conf. Ser.* **375** (2012) 042013.
- [50] A. Auger *et al.*, *Phys. Rev. Lett.* **109** (2012) 032505.

- [51] A. Gando *et al.*, Phys. Rev. C **85** (2012) 045504.
- [52] J. Hartnell *et al.*, J. Phys. Conf. Ser. **375** (2012) 042015.
- [53] A.S. Barabash, Phys. Rev. C **81** (2010) 035501.
- [54] Steven R. Elliott, Modern Physics Letters A **27** (2012) 1230009.
- [55] E. Garcia *et al.*, Appl. Radiat. Isot. **49** (1998) 1749.
- [56] H. Wulandari, J. Jochum, W. Rau, F. von Feilitzsch, Astroparticle Physics **22** (2004) 313.
- [57] J.B. Albert *et al.*, Nature **510** (2014) 229.
- [58] D.R. Artusa *et al.*, Eur. Phys. J. C **74** (2014) 2956; C.P. Aguirre *et al.* (CUORE), arXiv:1402.0922
- [59] A. Gando *et al.*, Phys. Rev. Lett. **110** (2013) 062502.
- [60] Alexander Barabash *et al.*, J. of Physics: Conference Series **173** (2009) 012008; M. Bongard (for the NEMO3 collaboration), arXiv:1105:2435.
- [61] M. Agostini *et al.*, Phys. Rev. Lett. **111** (2013) 122503.
- [62] H.V. Klapdor-Kleingrothaus *et al.*, Phys. Lett. B **586** (2004) 198.
- [63] M. Agostini *et al.* (GERDA), arXiv:1410.0853.
- [64] M. Agostini *et al.* (GERDA), arXiv:1307.2610.
- [65] D. Budjas *et al.*, JINST **4** (2009) P10007.
- [66] I. Abt *et al.*, Nucl. Inst. Meth. A **583** (2007) 332.
- [67] A. Barabash (for the SuperNEMO collaboration), arXiv:1112.1784.
- [68] J. J. Gomez-Cadenas *et al.* (NEXT), arXiv:1307.3914.
- [69] I. Dafinei *et al.*, Proc.of BEYOND Conf., Cape Town, South Africa, 2010, p. 256.

- [70] C. Arnaboldi *et al.* (CUORE), *Astropart. Phys.* **34** (2011) 797.
- [71] V. Nanal, *EPJ Web of Conferences* **66** (2014) 08005.
- [72] D.A. Nesterenko *et al.*, *Phys. Rev. C* **86** (2012) 044313.
- [73] M.K. Bacrania *et al.*, *IEEE Transactions on Nuclear Science* **56** (2009) 4.
- [74] N.K. Mondal, *Pramana* **79** (2012) 1003.
- [75] D. Budjas, M. Heisel, W. Maneschg, H. Simgen, *Appl. Radiat. and Isot.* **67** (2009) 706.
- [76] Fatima Padilla Cabal, Neivy Lopez-Pino, Jose Luis Bernal-Castillo, Yisel Martinez-Palenzuela, Jimmy Aguilar-Mena, Katia D'Alessandro, Yuniesky Arbelo, Yasser Corrales, Oscar Diaz, *Appl. Radiat. and Isot.* **68** (2010) 2403.
- [77] N. Cornejo Diaz, M. Jurado Vargas, *Nucl. Instr. and Meth. A* **586** (2008) 204.
- [78] J.C. Hardy, V.E. Iacob, M. Sanchez-Vega, R.T. Effinger, P. Lipnik, V.E. Mayes, D.K. Willis, R.G. Helmer, *Appl. Radiat. and Isot.* **56** (2002) 65.
- [79] R.G. Helmer, J.C. Hardy, V.E. Iacob, M. Sanchez-Vega, R.G. Neilson, J. Nelson, *Nucl. Instr. and Meth. A* **511** (2003) 360.
- [80] F. Hernandez, F. El-Daoushy, *Nucl. Instr. and Meth. A* **498** (2003) 340.
- [81] S. Hurtado, M. Garcia-Leon, R. Garcia-Tenorio, *Nucl. Instr. and Meth. A* **518** (2004) 764.
- [82] D. Karamanis, *Nucl. Instr. and Meth. A* **505** (2003) 282.
- [83] Jonas Boson, Goran Agren, Lennart Johansson, *Nucl. Instr. and Meth. A* **587** (2008) 304.
- [84] <http://www.tifr.res.in/~pell/lamps.html>

- [85] S. Agostinelli *et al.*, Nucl. Instr. and Meth. A **506** (2003) 250.
- [86] Rene Brun, Fons Rademakers, Nucl. Instr. and Meth. A **389** (1997) 81.
- [87] G.F. Knoll, Radiation Detection and Measurement, third ed., Wiley, New York (2000).
- [88] J. Rodenas, A. Pascual, I. Zarza, V. Serradell, J. Ortiz, L. Ballesteros, Nucl. Instr. and Meth. A **496** (2003) 390.
- [89] N.Q. Huy, D.Q. Binh, V.X. An, Nucl. Instr. and Meth. A **573** (2007) 384.
- [90] D. Karamanis, V. Lacoste, S. Andriamonje, G. Barreau, M. Petit, Nucl. Instr. and Meth. A **487** (2002) 477.
- [91] Viareggio, CAEN Application Note AN2508 (2011).
- [92] A. Nachab, Ph. Hubert, Nucl. Inst. Meth. B **274** (2012) 188.
- [93] G. Heusser, Nucl. Inst. Meth. B **58** (1991) 79.
- [94] I. Abt *et al.*, Eur. Phys. J. A **36** (2008) 139.
- [95] N. Dokania *et al.*, Nucl. Inst. Meth. A **745** (2014) 119.
- [96] S. Mathimalar *et al.*, Nucl. Inst. Meth. A **774** (2015) 68.
- [97] V. Singh *et al.*, Jour. of Low Temp. Phys. **175** (2014) 604.
- [98] H.J. Kim *et al.*, Astroparticle Physics **20** (2004) 549.
- [99] R. Agnese *et al.*, Phys. Rev. Lett. **111** (2013) 251301.
- [100] D.S. Akerib *et al.*, Phys. Rev. Lett. **112** (2014) 091303.
- [101] F. Bellini, C. Bucci, S. Capelli, O. Cremonesi, L. Gironi, M. Martinez, M. Pavan, C. Tomei, M. Vignati, Astroparticle Physics **33** (2010) 169.
- [102] D.M. Mei and A. Hime, Phys. Rev. D **73** (2006) 053004.

- [103] D.M. Mei, S.R. Elliott, A. Hime, V. Gehman and K. Kazkaz, *Phys. Rev. C* **77** (2008) 054614.
- [104] C. Arnaboldi *et al.*, *Nucl. Instr. Meth. A* **518** (2004) 775.
- [105] R.G. Wilson, *International J. of Mass Spectrometry and Ion Processes* **143** (1995) 43.
- [106] Torlon Resins Engineering Data, Solvay Advanced Polymers.
- [107] Sabyasachi Paul, G.S. Sahoo, S.P. Tripathy, S.C. Sharma, Ramjilal, N.G. Ninawe, C. Sunil, A.K. Gupta, and T. Bandyopadhyay, *Rev. of Sci. Inst.* **85** (2014) 063501.
- [108] So Kamada, Toshiro Itoga, Yasuhiro Unno, Wataru Takahashi, Takuji Oishi and Mamoru Baba, *J. of the Korean Physical Society* **59** (2011) 1676.
- [109] C.H. Poppe, J.D. Anderson, J.C. Davis, S.M. Grimes and C. Wong, *Phys. Rev. C* **14** (1976) 438.
- [110] S.P. Simakov and U. Fischier, *J. of the Korean Physical Society* **59** (2011) 1856.
- [111] www.nndc.bnl.gov
- [112] V.K. Mulik, H. Naik, S.V. Suryanarayana, S.D. Dhole, P.M. Prajapati, B.S. Shivashankar, K.C. Jagadeesan, S.V. Thakre, V.N. Bhoraskar and A. Goswami, *J. of Radioanal. Nucl. Chem.* **296** (2013) 1321.
- [113] H. Naik *et al.*, *Eur. Phys. J. A* **47** (2011) 51.
- [114] D.S. Akerib *et al.*, *Astroparticle Physics* **62** (2015) 33.
- [115] J. Argyriades *et al.*, *Nucl. Instr. Meth. A* **606** (2009) 449.
- [116] E. Andreotti *et al.*, *Astroparticle Physics* **34** (2010) 18.
- [117] Frank Vanhaecke, Patrick Degryse (eds.), *Isotopic Analysis: Fundamentals and Applications Using ICP-MS*, Wiley-VCH (2012).

- [118] Jeff Skiby (ed.), Application Guide to Neutron Multiplicity Counting, LA-13422-M, Los Alamos National Laboratory (1998).
- [119] R. Bonetti *et al.*, Physical Review C **51** (1995) 2530.
- [120] H. Wulandari *et al.*, Astroparticle Physics **22** (2004) 313.
- [121] Jerome M. Verbeke, Chris Hagmann, Doug Wright, UCRL-AR-22818, Lawrence Livermore National Laboratory (2009).
- [122] R. Heaton *et al.*, Nucl. Inst. Meth. A **276** (1989) 529.
- [123] D. M. Mei *et al.*, Nucl. Inst. Meth. A **606** (2009) 651.
- [124] R. Lemrani *et al.*, Nucl. Inst. Meth. A **560** (2006) 454.
- [125] N. Saneesh *et al.*, Proceedings of the DAE Symp. on Nucl. Phys. **58** (2013) 952.
- [126] N. Dokania *et al.*, Proceedings of the DAE Symp. on Nucl. Phys. **59** (2014) 828.
- [127] P. Belli *et al.*, Phys. Rev. C **83** (2011) 034603.
- [128] P. Belli *et al.*, Nuclear Physics A **846** (2010) 143.
- [129] P. Belli *et al.*, Nuclear Physics A **859** (2011) 126.
- [130] A. Barabash *et al.*, AIP Conf. Proc. **1417** (2011) 28.
- [131] P. Belli *et al.*, Phys. Rev. C **87** (2013) 034607.
- [132] V. I. Tretyak, Y. G. Zdesenko, Atomic Data and Nuclear Data Tables **80** (2002) 83.
- [133] Eric B. Norman and Dawn M. Meekhof, Phys. Lett. B **195** (1987) 126.
- [134] D.S. Murty, P. Jagam, V. Lakshminarayana, Canadian Jour. of Phys. **49** (1971) 1649.